



caesar
center of advanced
european studies
and research



UNIVERSITÄT
KOBLENZ · LANDAU

IMPLEMENTATION AND IMPROVEMENT
OF METAL-FILM PHASE PLATES
FOR SINGLE-PARTICLE CRYO-EM

vorgelegt von

Kristina Barragán Sanz

geb. Bachmeier

geboren am 03.11.1987 in Bendorf am Rhein

Angenommene Dissertation zur Erlangung des akademischen
Grades eines Doktors der Naturwissenschaften (Dr. rer. nat.)

Fachbereich 3: Mathematik/Naturwissenschaften
Universität Koblenz · Landau

Gutachterinnen und Gutachter:

Prof. Dr. Barbara Hahn

Dr. Stephan Irsen

Prüfungskommission:

Prof. Dr. Barbara Hahn

Prof. Dr. Christian Fischer

Prof. Dr. Eberhard Fischer

Tag der Disputation: 25.11.2021

Eidesstattliche Erklärung

Ich erkläre hiermit,

- dass ich die vorliegende Dissertation selbstständig verfasst habe und alle für die Arbeit benutzten Hilfsmittel und Quellen in der Arbeit angegeben sowie die Anteile etwaig beteiligter Mitarbeiterinnen und Mitarbeiter sowie anderer Autorinnen und Autoren klar gekennzeichnet sind;
- dass ich nicht die entgeltliche Hilfe von Vermittlungs- oder Beratungsdiensten (Promotionsberater oder andere Personen) in Anspruch genommen habe;
- dass ich die Dissertation nicht in gleicher oder ähnlicher Form als Prüfungsarbeit für eine staatliche oder andere wissenschaftliche Prüfung im In- oder Ausland eingereicht habe;
- dass ich keine gleiche oder eine andere Abhandlung in einem anderen Fachbereich oder einer anderen wissenschaftlichen Hochschule als Dissertation eingereicht habe;
- dass mir bewusst ist, dass ein Verstoß gegen einen der vorgenannten Punkte den Entzug des Dokortitels bedeuten und ggf. auch weitere rechtliche Konsequenzen haben kann.

Koblenz, den

Kristina Barragán Sanz

Abstract

Over the past few decades, Single-Particle Analysis (SPA), in combination with cryo-transmission electron microscopy, has evolved into one of the leading technologies for structural analysis of biological macromolecules. It allows the investigation of biological structures in a close to native state at the molecular level. Within the last five years the achievable resolution of SPA surpassed 2 Å and is now approaching atomic resolution, which so far has only been possible with X-ray crystallography in a far from native environment. One remaining problem of Cryo-Electron Microscopy (cryo-EM) is the weak image contrast. Since the introduction of cryo-EM in the 1980s phase plates have been investigated as a potential tool to overcome these contrast limitations. Until now, technical problems and instrumental deficiencies have made the use of phase plates difficult; an automated workflow, crucial for the acquisition of 1000s of micrographs needed for SPA, was not possible.

In this thesis, a new Zernike-type Phase Plate (PP) was developed and investigated. Freestanding metal films were used as a PP material to overcome the ageing and contamination problems of standard carbon-based PPs. Several experiments, evaluating and testing various metals, ended with iridium as the best-suited material. A thorough investigation of the properties of iridium PP followed in the second part of this thesis. One key outcome is a new operation mode, the *rocking* PP. By using this *rocking*-mode, fringing artifacts, another obstacle of Zernike PPs, could be solved. In the last part of this work, acquisition and reconstruction of SPA data of apoferritin was performed using the iridium PP in *rocking*-mode. A special semi-automated workflow for the acquisition of PP data was developed and tested. The recorded PP data was compared to an additional reference dataset without a PP, acquired following a conventional workflow.

Zusammenfassung

In den vergangenen Jahrzehnten haben sich Einzelpartikelanalyse (EPA) und Kryotransmissionselektronenmikroskopie (Kryo-EM) zu einer der führenden Technologien für die strukturelle Analyse von biologischen Makromolekülen entwickelt. Dies erlaubt die Untersuchung biologischer Strukturen in einem möglichst naturgetreuen Zustand auf molekularer Ebene. In den letzten fünf Jahren überwand die EPA erstmals die Auflösungsgrenze von 2 \AA und erreichte somit atomare Auflösung, was bislang nur mittels Röntgenkristallographie möglich war. Ein bestehendes Problem der Kryo-EM ist der schwache Bildkontrast. Seit der Einführung der Kryo-EM in den 1980er Jahren, wurde an Phasenplatten als mögliches Werkzeug, zur Verbesserung des Bildkontrasts geforscht. Hier limitierten immer technische Probleme bei der Herstellung oder geräteseitige Limitierungen, wie z.B. Hysterese der Linsen, den erfolgreichen Einsatz solcher Phasenplatten. Insbesondere ein automatisierter Arbeitsablauf für die Steuerung des Mikroskops und die Aufnahme der Bilder ließ sich nie realisieren.

In dieser Doktorarbeit wurde eine neue Zernike-Phasenplatte entwickelt und untersucht. Freistehende Metallfilme dienten als Phasenplattenmaterial, um Alterungs- und Kontaminationsprobleme der bislang üblichen kohlenstoffbasierten Phasenplatten zu überwinden. In ersten Experimenten zur Materialwahl wurde Iridium als geeignetes Metall identifiziert. Der zweite Teil der Arbeit behandelt die Untersuchung der Iridium-Phasenplatten hinsichtlich ihrer Eigenschaften und ihrem Verhalten im Elektronenmikroskop. Ein Resultat dieser Experimente ist der sogenannte *rocking*-Modus, bei dem die Phasenplatte während der Aufnahme bewegt wird und wodurch sich Streuungs- und andere Artefakte, die bei den Zernike-Phasenplatten üblicherweise auftreten, verhindern oder deutlich reduzieren ließen. Die Entwicklung eines angepassten Workflow ermöglichte die Aufnahme von EPA-Datensätzen mit Phasenplatte über mehrere Tage. Für die Evaluierung der Phasenplattendaten wurden Datensätze von Apoferritin mit und ohne Phasenplatte aufgenommen und miteinander verglichen.

Abbreviations

AFM Atomic Force Microscope

cryo-EM Cryo-Electron Microscopy

CTF Contrast Transfer Function

DED Direct Electron Detector

EM Electron Microscopy

FEG Field Emission Gun

FFT Fast Fourier Transform

FIB Focused Ion Beam

FSC Fourier Shell Correlation

PP Phase Plate

SEC Size-Exclusion Chromatography

SEM Scanning Electron Microscope

SNR Signal-to-Noise Ratio

SPA Single-Particle Analysis

TEM Transmission Electron Microscope

VPP Volta Phase Plate

2D Two Dimensional

3D Three Dimensional

Contents

Statement	i
Abstract	iii
Zusammenfassung	v
1 Introduction	1
1.1 Aim of this work	4
2 Fundamentals	5
2.1 The Transmission Electron Microscope	5
2.2 Image Formation Principles in Cryo-TEM	10
2.2.1 Electron Specimen Interaction	10
2.2.2 Contrast Problem in Cryo-Electron Microscopy	11
2.2.3 The Weak-Phase Object Approximation	11
2.2.4 The Contrast Transfer Function	14
2.3 Phase Plates	16
2.4 Cryo-Electron Microscopy	20

2.4.1	Cryo-Sample Preparation	20
2.4.2	Single-Particle Analysis	22
2.4.3	Phase Plate Cryo-Electron Microscopy	23
3	Materials and Methods	24
3.1	Materials and Devices	24
3.2	Methods	39
3.2.1	Sample Preparation	39
3.2.2	Cryo-Transmission Electron Microscopy Grids	44
3.2.3	Single-Particle Data Acquisition Workflow	46
3.2.4	Data Reconstruction	51
4	Development of a Metal-Film Zernike Phase Plate	60
4.1	Phase Plate Fabrication	61
4.1.1	Preliminary Experiments	61
4.1.2	Phase Plate Fabrication Workflow	63
4.1.3	Thickness Measurement of Phase Plate Films by Atomic Force Microscopy	69
4.2	Phase Plate Characterization	72
4.2.1	Phase Plate Installation	72
4.2.2	Material Selection	74
4.2.3	Phase Plate Lifetime and Ageing Experiments	77
4.2.4	Phase Plate Hole Size	81

4.3	The <i>Rocking</i> -Phase Plate	83
4.4	Discussion	90
5	Application of the PP for Single-Particle Analysis	97
5.1	Sample Preparation and Vitrification of Mouse Apoferritin	98
5.2	Prerequisites	98
5.3	Reference Dataset	100
5.3.1	Data Acquisition - Electron Microscopy	100
5.3.2	Single-Particle Reconstruction - Image Processing	101
5.3.3	Discussion	107
5.4	Modifications for PP Application	109
5.4.1	Leginon Workflow for Phase Plate Data Acquisition	109
5.4.2	Focus-Distance Test	112
5.4.3	Phase Plate Positioning and Adjustment	115
5.4.4	Discussion	117
5.5	Single Particle Analysis using the <i>Rocking</i> -Phase Plate	118
5.5.1	First Data Acquisition and Reconstruction using a <i>Rocking</i> - Phase Plate	118
5.5.2	CTF Estimation Tests	123
5.5.3	Second Data Acquisition and Reconstruction using a <i>Rock</i> - <i>ing</i> -Phase Plate	126
5.5.4	Third Data Acquisition and Reconstruction using a <i>Rocking</i> - Phase Plate	130

5.5.5	Particle Comparison - Reducing the Number of Particles of the Reference Dataset	134
5.5.6	Data Acquisition and Reconstruction using a Phase Plate in Static-Mode	139
5.6	Discussion	142
5.6.1	Sample Quality	143
5.6.2	Reconstruction	144
5.6.3	Leginon Workflow and Recording Conditions	151
5.6.4	Phase Plate	152
6	Conclusion and Outlook	155
	Bibliography	156
	List of Figures	173
	List of Tables	175
A	Apoferritin	176
A.1	Ferritin heavy chain equus caballus (horse)	176
A.2	Ferritin light chain equus caballus (horse)	177
A.3	Ferritin heavy chain mus musculus (mouse)	178
B	Phase Plates	179
B.1	Table of Phase Plates	179
B.2	Coat Thickness Measuring of Phase Plates by Atomic Force Microscopy	180

C Datasets	183
C.1 Dataset I 2020-03-31-mAPO	184
C.2 Dataset II 2020-04-05-mAPO	185
C.3 Dataset III 2020-05-03-mAPO-PP	186
C.4 Dataset IV 2020-05-18-mAPO	187
C.5 Dataset V 2020-05-21-mAPO-PP	188
C.6 Dataset VI 2020-06-30-mAPO-PP	189
C.7 Dataset VII 2020-07-29-mAPO-PP	190
C.8 Dataset VIII 2020-08-12-mAPO-PP	191
C.9 Dataset IX 2020-11-23-mAPO Reference Dataset	192
C.10 Dataset X 2020-11-30-mAPO-PP	193
Danksagungen	194

Chapter 1

Introduction

Studying life at a molecular resolution has been of great interest in laboratories all over the world for many years. Nobel prizes in chemistry in the years 2017, 2014, 2012, 1988 and 1985 were related to method development or high-resolution structural research in life science [1, 2, 3].

Electron Microscopy (EM) is a key technology for analyzing nature at nanometer resolution and below. EM allows investigating the structure of cells, single proteins or viruses at a molecular level, providing a better understanding of biological processes. Research on Zika virus [4] or SARS-CoV-2 spike proteins [5] are just two examples of recent discoveries using EM.

Conventional EM samples are usually chemically fixed and embedded in resin prior to the analysis using an electron microscope. This fixation procedure sacrifices fine structural details and limits resolution in the range of 1-2 nm. In order to reach molecular or even atomic resolution, the investigated samples need to be analyzed closer to their native state. In the 1970s and 1980s, Dubochet, Frank and Henderson successfully developed cryo-transmission electron microscopy, where samples are imaged in a vitrified state at liquid nitrogen temperature [1, 6].

Cryo-EM opened the possibility of studying biological structures, like proteins, at molecular resolution, without the need to grow single crystals like in X-ray crystallography. In contrast to crystallography, where samples are rigid crystals, cryo-EM allows the vitrification of molecules in different dynamic states. This enabled scientists, for the first time, to analyze molecules ‘in motion’ at atomic resolution [7]. The ability of cryo-EM to image samples in their near native state, comes at the cost of three major limitations:

difficult and time-consuming sample preparation, poor image contrast and sample sensitivity against the electron beam.

Only amorphous ice is transparent to the incoming electron beam. Therefore, it is absolutely crucial, to prevent the formation of ice crystals during sample preparation. Besides, the formation of crystalline ice would destroy the delicate structure of most biological samples.

In a conventional Transmission Electron Microscope (TEM), image contrast is generated by differences in the scattering behavior of the sample atoms.

Heavy elements scatter the incoming electrons stronger than light ones. Frozen biological samples consist mainly of light elements like carbon, oxygen, hydrogen etc. In these samples, the electron scattering is weak and the recorded micrographs show very low contrast. In such cryo-samples, phase contrast becomes the main image contrast. Phase contrast occurs when the phase of the incoming electron wave is slightly shifted when scattered by the sample. Image contrast is then generated by interference of the scattered, phase shifted beam and the unscattered beam. The key to improving the contrast in cryo-EM images, is to amplify the phase contrast. Methods of improving phase contrast have been investigated with great effort since the first introduction of cryo-EM in 1981 [8].

One approach to amplify phase contrast is using a PP. This additional electron-optical element, well known from light microscopy for many years [9, 10], increases contrast by adding an additional phase shift to either the elastically scattered electrons or the unscattered direct electron beam. Various types of PPs for transmission electron microscopy have been intensively investigated since the early 2000s. Nevertheless, their fabrication and use have been very difficult, mainly caused by

technical limitations of both, the PP fabrication and the performance of the electron microscopes at that time. These early works never led to a suitable setup for routine work.

Over the past 10 years, TEMs have made huge technical improvements. Nowadays, all modern instruments are fully digitally controlled, which makes their use much easier. Digitally controlled power supplies, and piezo-based motors greatly improved limitation like hysteresis effects of the lenses or position accuracy of the sample, apertures or a PP. Furthermore, electron sources with improved stability, multi-lens correction systems and computer assisted alignment workflows, founded the technical basis for a fully-automated use of modern cryo-electron microscopes.

Despite all these improvements, the contrast problem could not be solved. So, the interest in improving and developing new PPs is still high.

1.1 Aim of this work

In the project described in this thesis, I investigated a metal-film Zernike PP for cryo-EM of single proteins.

In the first part of the thesis, I describe the development of the PP. I started with testing various materials for the PP. A PP film typically needs to be very thin (~ 10 nm) and yet robust. In addition, it is essential that the metal used for the PP film, forms a fine-grain PP film, which is ideally resistant to charging and ageing.

To assure reproducible PPs, each step of the fabrication process is important. I establish a reliable fabrication workflow and look into the single workflow steps, e.g. sputtering of the metal-film and the PP hole cutting.

Fundamental for the performance of the PP is, besides the material of the PP film, the thickness of the film, determining the phase shift and the PP hole diameter, assigning the cut-on frequency of the PP.

This PP hole is also known for creating fringing artifacts that are visible in the micrographs. Therefore, I implemented a new acquisition mode when using the PP, with the intention of reducing artifacts produced by a static optical element in the TEM beam path. The so-called *rocking*-mode was extensively tested.

Furthermore, the installation and replacement of the PP in the TEM is a crucial and time-consuming step. In order to be able to perform the PP exchange by only one person and to reduce the downtime of the TEM, several changes in the installation process made herein, will be described.

The second part of this thesis deals with the application of the PP. First, I describe a new acquisition workflow for a semiautomatic data acquisition of single proteins using a PP. This was followed by the acquisition of datasets, using the PP in static and *rocking*-mode.

Finally, I intend to compare the structures of apoferritin acquired under standard acquisition conditions, using an objective aperture, with structures obtained using a metal-PP in static and *rocking*-mode.

Chapter 2

Fundamentals

2.1 The Transmission Electron Microscope

The first image using an electron beam was demonstrated in 1931 by Ruska and Knoll [11, 12]. Only a few years later, Ruska presented a working TEM and showed images of bacteriophage lysis [13, 14].

Already in this first attempt, the electron microscope outran the resolution of the best light microscopes at the time reaching a magnification of 12,000x [15]. Since then, electron microscopes have become crucial instruments in various fields of science and engineering. Nowadays, atomic resolution, below 100 pm, is state of the art and numerous analytical techniques like diffraction, spectroscopy or tomography enhanced the usability of these instruments a lot. Even for this thesis, which is a methodical study in transmission-electron microscopy, several additional electron microscopes were used for e.g. PP fabrication or analysis. Since electron microscopes play such a major role for the present work, a brief description of the principles of EM will be presented in the following chapter.

Elements of a Transmission Electron Microscope

Figure 2.1 shows a schematic view of a modern TEM.

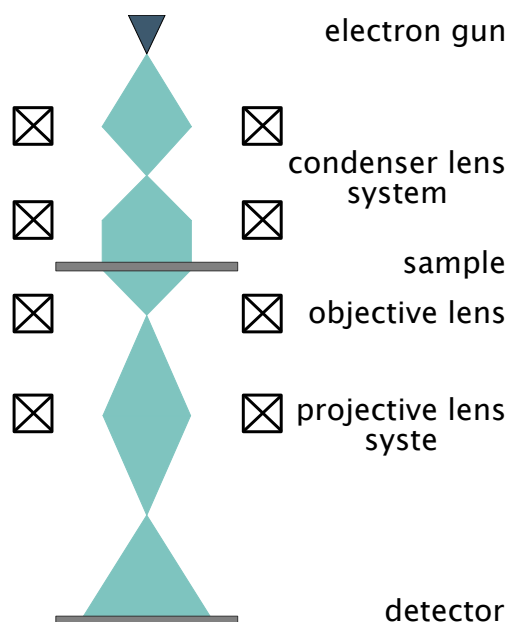


Figure 2.1: Setup of a TEM starting with the electron gun on the top, followed by the projective lens system, which provides parallel illumination of the sample. Below the sample, the electron beam is focused by the objective lens. The projective lens displays the final image onto the detector.

A TEM can be divided into five major parts:

The **electron gun** is the part of the TEM that emits the electrons and accelerates them to the desired kinetic energy. In principle, two types of electron guns can be used: thermionic guns and field emission guns.

Today, TEMs, used for high-resolution imaging, are equipped with a Field Emission Gun (FEG). FEGs show a superior brightness and a smaller crossover compared to thermionic electron guns. A smaller zero beam crossover facilitates the positioning of a PP in the back-focal plane and allows the use of a smaller PP hole diameter, which reduces the cut-on frequency and thereby improves the contrast [16].

A common electron source used in commercial TEMs is the Schottky-FEG, which

combines the advantages of both thermionic and field emission guns. Compared to cold-FEGs, Schottky-FEGs tolerate a poorer vacuum as the tip is additionally heated to it clean. Schottky compared to cold-FEGs provide a greater stability of beam current and still have low noise. Besides, they are more reliable and easier to operate. Once the electrons are emitted by either thermionic, or field emission, the electrons are accelerated to their final kinetic energy using a cascade of acceleration coils. [17, 18, 19]

The **condenser lens system** is the second major part in a TEM. It is responsible for forming a parallel beam to illuminate the sample. Modern TEMs are equipped with three condenser lenses. The first condenser lens creates an image of the gun crossover and defines the spot size. Condenser lens two and three assign the beam diameter on the specimen and provide parallel illumination of the sample. Within a certain range, the third condenser lens can be adjusted to control the convergence angle and the diameter of the beam to assure parallel illumination. A adjustable C3 condenser lens is essential for PP application. By changing the C3 lens to converging or diverging the beam, the PP can be shown on the screen. For PP data acquisition, the PP must be correctly centered and requires a parallel illumination of the sample. Besides the electron lenses, the condenser system is equipped with a condenser aperture, which defines the maximum angle of electrons deviating from the optical axis. [17, 18, 19]

Below the condenser system, the specimen is positioned on the **sample stage**. In current commercial microscopes, side-entry holders are used to insert the sample into the TEM. High-precision goniometers allow an accurate positioning of the sample within a subnanometer range. This is important for data acquisition where the change of exposure position is performed using stage movement instead of beam and image shift. [19, 20]

Once the electrons have passed the specimen, they reach the first image forming lens of the TEM: the **objective lens**. The electron beam is focused by the objective lens at the back-focal plane, where an objective aperture, or a PP, can be positioned. The objective lens is a strong electromagnetic lens. To minimize hysteresis effects, it is designed as a constant power lens, to keep thermal fluctuation

minimal. The focal length of a TEM objective lens is typically in the range of 0.5 to 5 mm. The Titan Krios used in this work has a focal length of 2.7 mm. For PP data acquisition, it is important that the objective lens is stable against hysteresis to keep a constant focal length. [17, 18, 19]

The **projector lens system** is located below the objective lens. It consists of several intermediate lenses and the projector lens. These lenses are used to magnify the image coming from the objective lens. The image is formed by at least three lenses in order to receive a rotation free image. The magnified image is finally projected onto a fluorescent screen, camera or a detector. [17, 19, 20]

Modern TEMs are often equipped with a combination of **detectors**: a CCD¹ camera and a CMOS based Direct Electron Detector (DED). In CCD cameras electrons have to be converted into photons before they can be detected by the imaging sensor. Therefore, a scintillator is used. In comparison, direct electron detectors do not use optically coupled devices. Here, the electrons are directly detected by the sensor without being transformed. Using direct translation from electrons towards the image improves the Signal-to-Noise Ratio (SNR), the DQE² and thereby the image quality. Especially beam-sensitive cryo-samples, which require low electron dose for data acquisition, profit from using DEDs. Another advantage of CMOS based DEDs is the improved readout speed. CCD cameras offer typical readout speeds in the range of 1-5 seconds/image. The CMOS technology of DEDs therefore, allows a parallel readout of all detector pixels resulting in a readout speed of up to 44 frames/second. This enables DEDs to record frame movies instead of integrated images. These frame movies can be drift corrected and therefore, offer a greatly improved image quality compared to CCD images. The Titan Krios used for this thesis is equipped with a 4k x 4k CMOS2 Falcon II DED (*Thermo Fischer Scientific*), recording 17 frames/second for high-resolution data acquisition. For low magnification micrographs, the Titan Krios also includes an Orius SC1000 (*Gatan*), a scintillator based CCD camera. The development of DEDs has been one factor for the evolution of cryo-EM over the last few years. [21, 22, 23, 24]

¹Charge-Coupled Device

²Detector Quantum Efficiency

Another huge improvement has been made by Maximilian Haider by introducing the **C_s corrector** [25]. This complex multipole element allows the correction of objective lens aberrations.

Optical lenses, as well as electromagnetic lenses, suffer from various types of aberrations. A prominent resolution limiting example is the spherical aberration, where light or electrons far from the optical axis are more strongly focused by the lens than electrons close to the optical axis.

In light microscopy, spherical aberrations can typically be corrected by aspherical lenses [18]. However, aspherical lenses for electron microscopy are not easy to realize.

Following Scherzer's theorem, usual round magnetic lenses have a positive spherical aberration coefficient C_s [26]. This positive C_s needs to be reduced, or ideally completely compensated, by a negative C_s . Haider et al. showed that by combining two transfer doublets and two hexapoles alternately, a negative C_s can be created and constructed the first functional hexapole corrector system for a 200 kV TEM [25, 27]. Since the early 2000s, aberration correctors are commercially available for TEMs and have been useful for many applications in high-resolution imaging [28]. All corrector elements are computer controlled [29] and the aberrations can be precisely measured using Zemlin diffractogram tableaux [30].

Using a C_s corrector allows the usage of electrons, which impact the objective lens far-off from the optical axis without losing resolution. Highly aberrated beams can be corrected and do not need to be excluded. The spatial resolution increased due to the smaller diffraction limit probe size [20]. This opens a broad variety of new possibilities, e.g. redesign of the sample area with more space, which allows in situ experiments, cryo applications or atomic resolution at low energies [20, 28]. In our case, the C_s corrector was crucial to correct aberrations induced by the PP. A PP is an additional element in the beam path of the TEM. PPs suffer from ageing, which provokes charging of the PP and causes the PP to act like a lens [31, 32]. To compensate for aberrations caused by the PP, a microscope equipped with a C_s corrector was a great benefit for this work.

2.2 Image Formation Principles in Cryo-Transmission Electron Microscopy

In this chapter, the image formation principles in transmission-electron microscopy are shortly described, beginning with a brief introduction of the electron-specimen interaction and followed by the contrast problem in cryo-EM. In consideration of the weak-phase object approximation, image contrast in a TEM will be mathematically described, to derive the Contrast Transfer Function (CTF).

2.2.1 Electron Specimen Interaction

Image formation in transmission-electron microscopy is based on the interaction between the electron beam and the sample.

Here, two types of interaction are observed: elastic and inelastic scattering. Elastic scattering of electrons, results from the electron-nucleus interaction and thereby, changes the momentum and phase of the incident electron. The change of its momentum and phase happens without a significant transfer of the kinetic energy of the electron. Elastic scattering of electrons is the major source that contributes to image contrast in a TEM.

In comparison, inelastic scattering arises from electron-electron interactions, where a significant energy transfer between the incident electron and the sample takes place. Here, part of the kinetic energy is converted into atom-electron excitation, while most of the excitation is converted into heat, causing irreversible radiation damage in biological specimens. The part of electrons, which are inelastically scattered, have a low angular distribution and are not favorable for high-resolution imaging. Inelastically scattered electrons produce an undesired background term in the image, which is normally tolerated. However, inelastically scattered electrons build the basis for various analytical methods in EM, e.g. EELS³, ELNES⁴,

³Energy-Loss Spectrum

⁴Energy-Loss Near-Edge Structure

EXELFS⁵. [33, 17, 19, 34]

A more detailed description of the theoretical background of electron interactions can be found in [17, 19].

2.2.2 Contrast Problem in Cryo-Electron Microscopy

Biological samples consist of low scattering elements of low atomic numbers, e.g. carbon and oxygen. Therefore, biological samples are nearly transparent to the high-energy electrons in a TEM. Samples embedded in amorphous ice decrease the contrast even further due to the inferior background noise, resulting in a worse SNR. Very thin specimens (< 100 nm) of light atoms are liable to the weak-phase object approximation where the amplitude contrast is negligible. Hence, the major contrast in cryo-samples is phase contrast. But, the transfer of low spatial frequencies in a conventional TEM is close to zero. In a conventional TEM, phase contrast is visualized by defocussing the objective lens. Another possibility to increase the transfer of low spatial frequencies, carrying the contrast information of biological samples, is the application of PPs. [34, 17]

2.2.3 The Weak-Phase Object Approximation

In cryo-EM, phase contrast is the major principle in image formation. Therefore, the description of image formation in this chapter considers exclusively phase contrast. All other contrast types, e.g. amplitude or diffraction contrast are neglected since their role in cryo-EM is less important.

Mathematically, the image formation in a TEM can be described by the following formulas, which follow the derivation of Frank et al. [34]:

Electrons scattered by the Coulomb potential of a nucleus (elastic scattering), change their momentum and phase. The emerging phase shift $\Phi(\mathbf{r})$ is proportional

⁵Extended Energy-Loss Fine Structure

to the integrated Coulomb potential along the beam path and can be described by formula 2.1, where \mathbf{r} is a two-dimensional vector and $C(\mathbf{r},z)$ is the 3D Coulomb potential distribution within the object. [34, 17]

$$\Phi(\mathbf{r}) = \int C(\mathbf{r}, z) dz \quad (2.1)$$

The incoming electron wave Ψ_0 is altered by the phase shift $\Phi(\mathbf{r})$, occurring during an elastic scattering process inside the sample and results in the object wave $\Psi(\mathbf{r})$ [34].

$$\Psi(\mathbf{r}) = \Psi_0 \exp [i\Phi(\mathbf{r})] \quad (2.2)$$

For very thin samples of light elements (< 10 nm), e.g. biological cryo-samples, the assumed phase shift is $\Phi(\mathbf{r}) \ll 1$. This is known as the weak-phase approximation. In this case, the object wave can be described by the first two terms of the Taylor expansion [34, 17].

$$\Psi(\mathbf{r}) = \Psi_0 \left[1 + i\Phi(\mathbf{r}) \right] \quad (2.3)$$

In a TEM, lens aberrations and defocussing occur, which affect the phase shift of the scattered wave and can be expressed by the following term [34]:

$$\gamma(\mathbf{k}) = 2\pi\chi(\mathbf{k}) \quad (2.4)$$

Here, $\gamma(\mathbf{k})$ is the induced phase shift and $\chi(\mathbf{k})$ is the wave aberration function, which can be indicated by the following formula [34]:

$$\chi(k) = \left[-\frac{1}{2}\lambda\Delta z k^2 + \frac{1}{4}\lambda^3 C_s k^4 \right] \quad (2.5)$$

where λ is the electron wavelength and k is the spatial frequency. With reference to the defocus Δz and the spherical aberration C_s , yet ignoring the effect of astigmatism.

The wave function $\Psi_{bf}(\mathbf{k})$ in the back focal plane of the objective lens can be described by the Fourier transform of the wave function $\Psi(\mathbf{k})$ and a term representing the effect of the phase shift due to lens aberrations [34].

$$\Psi_{bf}(\mathbf{k}) = \mathfrak{F} \{ \Psi(\mathbf{k}) \} \exp [i\gamma(\mathbf{k})] \quad (2.6)$$

The image plane wave function $\Psi_i(\mathbf{r})$ is obtained from the wave function of the back focal plane $\Psi(\mathbf{k})$, after modification by the aperture function $A(\mathbf{k})$, through an inverse Fourier transform [34]:

$$\Psi_i(\mathbf{r}) = \mathfrak{F}^{-1} \left\{ \mathfrak{F} \{ \Psi(\mathbf{k}) \} A(\mathbf{k}) \exp [i\gamma(\mathbf{k})] \right\} \quad (2.7)$$

$$A(\mathbf{k}) = \begin{cases} 1 & \text{for } |k| = \theta/\lambda \leq \theta_1/\lambda \\ 0 & \text{elsewhere} \end{cases}$$

where θ_1 is the radius of the objective aperture.

The intensity distribution in the image plane $I(\mathbf{r})$ can be described by the square of the absolute value [34]:

$$I(\mathbf{r}) = |\Psi_i(\mathbf{r})|^2 \quad (2.8)$$

Following the weak-phase approximation, where the amplitude contrast is negligible and replacing the exponential function of formula 2.7 by a trigonometric function, according to Euler's formula, the image intensity is approximately:

$$I(\mathbf{r}) \approx 1 - 2\mathfrak{F}^{-1}\{\Psi(\mathbf{k})\sin(\gamma(\mathbf{k}))\} \quad (2.9)$$

The sine part of formula 2.9 represents the CTF. This CTF is essential for understanding image formation especially, when using a PP and will therefore be further described in the following chapter.

2.2.4 The Contrast Transfer Function

The CTF describes the imaging properties of the objective lens of a TEM. The sine part of formula 2.9 represents the CTF and can be expressed by the following equation [34]:

$$CTF(k) = \sin(\gamma(k)) = \sin\left[2\pi\left(-\frac{1}{2}\Delta z\lambda k^2 + \frac{1}{4}C_s\lambda^3 k^4\right)\right] \quad (2.10)$$

where λ is the wavelength, Δz is the defocus and k is the spatial frequency. Here, the part of amplitude contrast is neglected, as the major source of image contrast in cryo-EM is phase contrast.

In traditional cryo-EM the phase contrast is amplified by changing the defocus Δz . The CTF is represented by a sine function, where the contrast transfer in the area of low spatial frequencies is close to zero. Especially for biological samples, the contrast transfer in the area of low spatial frequencies is very important. The area of low spatial frequencies represents the larger structures of the sample. If these frequencies are not represented in the micrograph, the sample is not visible. In order to image biological samples in cryo-EM, the defocus Δz is typically set to

a value of a few μm . This shifts the first zero crossing of the CTF in the direction of low spatial frequencies and due to the oscillation of the sine function increases contrast. The first zero crossing of the CTF gives information about the resolution limit. Beyond the first crossing phase flips occur in the CTF, which have to be corrected during data processing. Shifting the first zero crossing in the direction of low spatial frequencies by defocussing the sample, results in lower resolution. Additionally, the total number of zero crossings of the CTF increases, which leads to a loss of contrast information.

To increase the contrast transfer for low spatial frequencies and avoid the loss of resolution occurring during defocussing the sample, PPs can be used. For the usage of PPs, the CTF is extended by the phase shift Φ_{PP} .

From this follows the CTF_{PP} :

$$CTF_{PP}(k) = \sin \left[2\pi \left(-\frac{1}{2}\Delta z \lambda k^2 + \frac{1}{4}C_s \lambda^3 k^4 \right) + \Phi_{PP} \right] \quad (2.11)$$

where λ is the wavelength, Δz is the defocus, k is the spatial frequency and Φ_{PP} the additional phase shift induced by the PP.

Ideally, PPs shift the phase of the electron by an additional 90° . If a phase shift of 90° is applied to the formula 2.11, the sine function turns into a cosine function. A change to a cosine function results in a high contrast transfer for low spatial frequencies, without a loss of resolution.

The interest in PPs is high and several attempts for various types of PP systems have been made. A more detailed description about PPs follows in the next chapter.

2.3 Phase Plates

The idea of PPs, to improve image contrast, started back in 1942, when Zernike described a PP for light microscopy [35, 36]. Five years later, Boersch presented the idea for a PP system in a TEM [37]. The first practical implementations were tested in the late 50s and early 60s of the last century. These tests were mostly abandoned due to technical difficulties in producing the ultra thin PP films.

With the emerging cryo-transmission electron microscopy in the 1990s and early 2000s, PP systems for TEM experienced a revival in several EM laboratories.

The group of Nagayama focused on thin carbon based PPs with Zernike [38] and Hilbert [39] design. Further investigation on the electrostatic design of PPs was done by the group of Schröder [40, 41]. Also, rather exotic ideas like anamorphic PPs [42], photonic PPs [43] or systems using electrostatic mirrors [44] were tested. In 2012 a new PP principle was presented by Malac et al. [45] the so-called hole-free PP, where an electrostatic potential is generated by the electron beam on a thin material film. At the same time, KonTEM at caesar started their research on a Zernike-type metal-film PP [46].

In general, PPs are used to increase the image contrast at low spatial frequencies. They can tune the image contrast that arises during the interaction between the electron beam and the sample. The electron beam can be thought of as a beam consisting of two parts: the direct or central beam, containing the unscattered electrons and the scattered beam, containing the elastically scattered electrons. Due to the interference of the scattered and unscattered part of the electron beam, image contrast emerges. [33]

In the back focal plane of the objective lens, the scattered and unscattered part of the electron beam can be spatially separated. Therefore, PPs are normally positioned in the back focal plane of the objective lens.

Today, there are mainly two types of commonly used PPs in transmission-electron microscopy: the Volta Phase Plate (VPP), a derivative of Malac's design and the Zernike Phase Plate.

In 2014, Danev et al. presented the VPP, which follows the principle of the hole-

free PP. The PP consists of a thin continuous amorphous carbon film (fig. 2.2(A)). The PP film is constantly heated to 200 °C, to prevent contamination and to enable the Volta potential effect. Prior to the image acquisition, the phase shift has to be generated by continuous radiation of the carbon film for 1 min and is induced by the direct electron beam itself. Through the interaction of the central diffraction beam, with the amorphous carbon film, a potential immediately above the surface of the material occurs. This negative potential is called the Volta potential and is equal to the difference between the inner and the surface potential. Through the Volta potential, the central beam experiences a positive phase shift relative to the scattered beams, which is not constant and increases proportionally to the accumulated dose. [47, 48, 33]

Today, the VPP is the standard PP in most TEMs from Thermo Fisher Scientific.

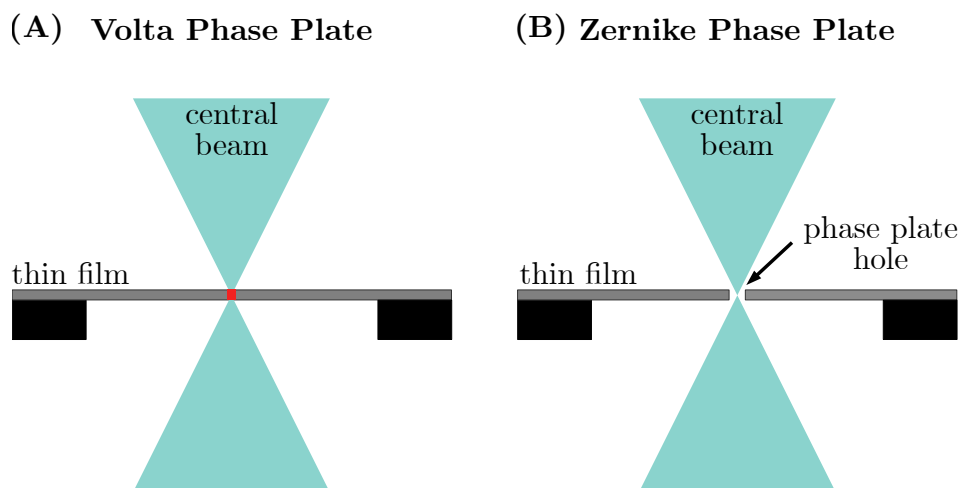


Figure 2.2: Schematic drawing of the VPP and Zernike PP principles (A) shows the principle of the VPP, where the central beam induces a Volta-potential to emerge a positive phase shift [47]. (B) represents the principle of the Zernike-type PP, consisting of a thin amorphous carbon film with a small hole for the central beam to pass through. Figure is adapted from Danev et al. [49].

Besides the VPP, Danev et al. presented a Zernike-type PP for transmission-electron microscopy, consisting of a thin amorphous carbon film, back in 2001 [38]. Unlike the VPP, the Zernike PP has a small hole in the middle of the PP film. Here, the PP has to be well centered in the back focal plane of the TEM.

Figure 2.2(B) shows, that the central electron beam has to pass through the hole of the PP, while the scattered part passes through the PP film. This leads to a phase retardation of the scattered electron beam [38] and positive phase contrast (fig. 2.3 (B)).

How is a PP influencing the image formation?

In cryo-EM, the assumption is that the electrons experience a phase shift of $\sim 90^\circ$ or $\frac{2}{\pi}$ during the interaction with a biological sample (weak-phase approximation). If an image is acquired in focus, the image amplitude Ψ_i and the scattered amplitude Ψ_{sc} can be added up to a vector addition shown in figure 2.3 (A).

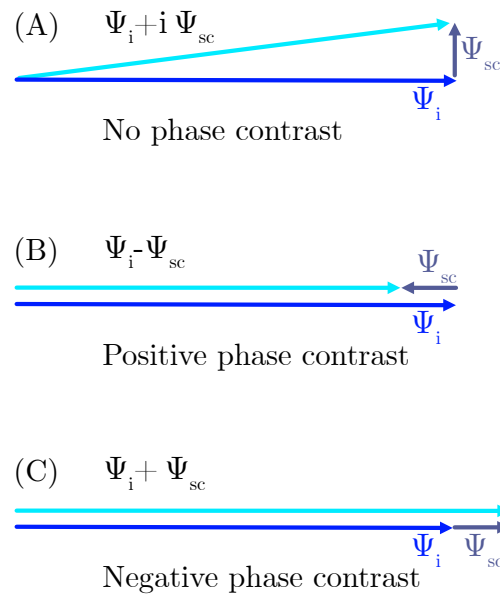


Figure 2.3: (A) Vector addition of the image amplitude Ψ_i and the phase shifted scattered amplitude Ψ_{sc} by 90° . (B) positive phase contrast due to an additional phase shift of 90° . (C) negative phase shift induced by an additional phase shift of -90° . Adapted from Reimer et al. [17].

Here, $\Psi_{sc} \ll \Psi_i$ and the resulting amplitude $\Psi_i + i\Psi_{sc}$ (light blue vector) has approximately the same value than the image amplitude Ψ_i , which means that the phase object is invisible.

In order to make the phase object visible, the phase of the scattered amplitude Ψ_{sc} needs to be shifted ideally by an additional 90° , now the phase of the scattered amplitude directly contributes to the resulting image contrast (light blue vector). This can be done by either a negative phase shift, fig. 2.3 (B), which leads to positive phase contrast or by positive phase shift, fig. 2.3 (C), leading to negative phase contrast.

For Zernike PPs, the amount of this additional phase shift is controlled by the retardation of the scattered electron beam inside the PP film. The amount of this retardation and the emerging phase shift results from the mean inner potential of the PP film and can be calculated by the following equation [17]:

$$\Phi = \frac{2\pi}{\lambda} \frac{eU_i}{E} \frac{E_0 + E}{2E_0 + E} t \quad (2.12)$$

Here, Φ is the phase shift, λ is the wave length, E_0 is the rest energy and E is the kinetic energy. The amount of phase shift of a thin film can be influenced by the thickness (t) and the mean inner potential of the PP material (U_i).

Over the last years, several attempts have been made to improve the performance of Zernike PPs. Zernike PPs come along with various obstacles such as contamination of the PP, leading to ageing and charging of the PP film. Besides, the fabrication process has been very complex and the centering of the PP has been difficult. Furthermore, PP acquisition using Zernike PPs show fringing artifacts in the images, resulting from the sharp phase jump at the PP hole edge. [33]

In this work, a Zernike-based metal-film PP for cryo-EM is implement and improved. Several improvements have been made to overcome the obstacles of Zernike PPs mentioned above.

2.4 Cryo-Electron Microscopy

During the last years, the interest in cryo-EM increased tremendously. Since the ‘resolution revolution’ [50], ongoing technical improvements helped to reach a resolution of 1.3 Å [51, 52]. With these improvements, new possibilities for the application of cryo-EM arose. It became a favored method to study the structure of viruses and proteins, e.g. the spike protein of SARS-CoV-2 reaching 3.5 Å resolution [53].

2.4.1 Cryo-Sample Preparation

Cryo-EM allows analysing biological samples close to their native state. In order to make them suitable for the acquisition with a TEM, the water in the samples needs to be immobilized or removed [54]. One way to immobilize the water in biological samples, and make them stable for the high vacuum of a TEM, is freezing. When water changes the aggregate state from liquid into frozen state, it normally tends to crystallize. To avoid crystallization and to obtain amorphous ice, the sample has to be frozen by a rate of approximately 10^5 °C/sec [55]. For thick biological samples, such as tissue or cells, vitrification can only be achieved under high pressure (≈ 2000 bar) [56]. Moor and Riehle introduced the high-pressure freezing technique in 1968 [57].

Smaller biological complexes, such as proteins or viruses, dispersed in an aqueous solution, can be vitrified using plunge freezing. Plunge freezing is the commonly used sample preparation technique for SPA. Here, the aqueous sample containing the biological molecule is applied onto a TEM grid covered with a holey carbon film. The surplus liquid is blotted with filter paper and then the grid is rapidly plunged into liquid ethane.

Ethane is condensed to a temperature between -150 °C and -170 °C using liquid nitrogen, to quickly cool down the sample below the devitrification temperature of around -135 °C. Once the samples are frozen, they need to be kept under cryo

conditions. If the sample exceeds the temperature of $-135\text{ }^{\circ}\text{C}$, it starts to crystallize and becomes intransparent for the electron beam. [6, 54]

Plunge freezing can be performed using manual or automated plunge freezers. As sample preparation in cryo-EM is still challenging, there is an ongoing development of various freezing techniques, such as jet-freezing [58, 59] or pin-printing [60] to vitrify biological samples.

Apoferritin

Apoferritin became a benchmark sample in cryo-EM after passing the difficulties in reconstruction at lower resolutions [61] back in 2014. Today, it is commonly used in cryo-EM facilities around the world for high-resolution tests [51, 62, 63, 64, 65]. Due to its molecular stability and octahedral symmetry, it allows high-resolution reconstructions from relatively few particles. The actual record of the highest resolution single-particle cryo-EM structure yet obtained is a 1.22 \AA resolution apoferritin structure by Nakane et. al in 2020 [51].

Ferritins are iron storage proteins with a structural motif of a bundle of four α -helices. Horse-spleen apoferritin has a molecular weight of about 440 kDa and is composed of 24 subunits (molecular weight 18 kDa) each containing 163 amino acids. The spherical hollow shell has an outside diameter of 130 \AA and an inside diameter of 75 \AA [66].

2.4.2 Single-Particle Analysis

In cryo-EM there are two common methods to gain a three dimensional structure of a biological sample.

One method is electron tomography, where the sample is tilted step-by-step between $\pm 70^\circ$. After each step, an image is taken, which later can be reconstructed to a three dimensional model.

The other method to study the structure of small biological complexes is called single-particle analysis. Here, a homogeneous population of purified protein or viruses are embedded into a very thin layer of amorphous ice using plunge freezing, which has been described earlier. At best, the ice layer is not much thicker than the largest diameter of the protein.

The particles are ideally randomly oriented. In order to statistically obtain an image of the protein from each angle, thousands of images are required. Some proteins tend to show preferred orientations inside the ice layer. To overcome this problem, the sample is tilted and images of the proteins are acquired under various angles. Once the micrographs have been acquired, various software programs support the determination of the three dimensional structure of the particle. During the reconstruction process, the software identifies the orientation of every particle in each micrograph. The program assumes that all images are projections of the same particle, only under various angles. Therefore, all images are used to reconstruct the 3D structure of the particle, which is also known as the density map.

2.4.3 Phase Plate Cryo-Electron Microscopy

A general problem when analyzing frozen biological samples in a TEM is the extremely weak image contrast. Especially the low image frequencies are poorly represented. Traditionally, this is compensated by recording micrographs using a defocused microscope. This additional defocus is up to several μm and introduces image artifacts affecting the image resolution. In conventional transmission-electron microscopy, the low spatial frequencies are poorly represented in the micrograph. Radiation sensitive proteins, which are embedded into amorphous ice for SPA, suffer from a low SNR. The contrast in conventional transmission-electron microscopy images can be increased by either moving the sample out of focus or by using PPs to increase low spatial frequencies.

The advantage of using PPs is the increased image contrast with constant resolution. With the help of PPs, small and light protein structures like haemoglobin could be solved reaching a resolution of 3.2 \AA [67].

Another advantage in using a PP is that due to the contrast improvement by the PP, less images are needed to solve a three dimensional structure compared to normal data acquisition without a PP. This would reduce the time for acquisition and reconstruction.

On the other hand, PP data acquisition can be more time consuming due to the additional preparation steps needed for operating the PP.

On top of that, the PP is an additional element in the beam path of the TEM that can lead to artifacts. Here, ageing of the PP is a problem that needs to be solved. Furthermore, the fabrication of the PPs can be very difficult. Reliable fabrication of free-standing metal films of only a few nanometers is very challenging.

Chapter 3

Materials and Methods

3.1 Materials and Devices

All materials and chemicals used for protein purification in this thesis are listed in tables 3.1 and 3.2. Their application is further described in more detail in section 3.2.1. A list of all used TEM grids can be found in table 3.3, section 3.2.2 gives a more detailed description of the cryo-TEM grids. Instruments are listed in table 3.4 while their usage is further described in the methods section 3.2.

Table 3.1: Materials and devices used protein expression and purification.

Materials	Source
Centrifuge tube filters 0.22 μm , Costar [®] Spin-X [®]	Corning Life Science
Cuvettes, PMMA, 1.5 ml	VWR
Falcon tubes, 50 ml	Sarstedt
Pipette tips	Nerbe Plus
Protein Marker (10-245 kDa) prestained	AppliChem
Reaction tubes, 1.5 ml	Sarstedt
Reaction tubes, 2.0 ml	Sarstedt
5-20% gradient SDS gel	self prepared with Bio-Rad gradient former
SEC column HiLoad 16/600 Superdex 200 pg	GE Healthcare
Spectra/Por2, 12-14 kDa MWCO, dialysis membrane	Spectrum
Syringe, 1 ml, Injekt [®]	Braun
Vivaspin Turbo4, 30 MWCO	Sartorius
Whatman filter paper, Grade 2 50 mm	Sigma Aldrich (<i>WHA1004050</i>)
Devices	
Beckman Avanti Centrifuge with rotor JLA 8.1 (For harvesting culture) and JA 25.50	Beckman Coulter
FPLC system NGC Quest	Bio-Rad
Incubator (Ecotron)	Infors-HT
Nano Photometer	Implen
SDS PAGE system	Bio-Rad
Ultrasonic device	Hielscher Ultrasonics
water purification system	Thermo Fisher Scientific

Table 3.2: Chemicals used for protein expression and purification.

Chemicals	Source
Acetic acid	Carl Roth
Acrylamid-, Bisacrylamid solution (ROTIPHORESE [®] Gel 30(37.5:1))	Carl Roth
Ammonium persulfate (APS)	Carl Roth
Ammonium sulphate, (NH ₄) ₂ SO ₄	Carl Roth
Bromophenol Blue	Sigma Aldrich
Coomassie Brilliant Blue R250	Sigma Aldrich
D(+)-Glucose	Carl Roth
DL-Dithiothreitol (DTT)	Sigma Aldrich
Ethanol, denatured	VWR
Glycerol	Carl Roth
Glycine	Carl Roth
HEPES PUFFERAN [®] ≤ 99.5 %, p.a.	Carl Roth
Hydrochloric acid (HCl), 1 N	Carl Roth
Isopropyl-β-D-thiogalactopyranosid (IPTG)	Carl Roth
Kanamycin sulphate	Carl Roth
LB agar (Lennox)	Carl Roth
LB medium	Carl Roth
Magnesium sulfate heptahydrate (MgSO ₄ * 7H ₂ O)	Merck
N,N,N,N-Tetramethylethylen diamin (TEMED)	Carl Roth
SDS pellets	Carl Roth
SIGMAFAST [™] Protease Inhibitor Tablets	Sigma Aldrich
Sodium chloride (NaCl)	Carl Roth
Sodium hydroxide (NaOH), 1 N	Carl Roth
Tris PUFFERAN [®] ≥ 99.9 %, p.a	Carl Roth

Table 3.3: TEM grids used in this work.

Grids	Source
Carbon Support Films Au 200 mesh	Quantifoil
Carbon Support Films Cu 200 mesh	Quantifoil
Holey Carbon Films R2/1 Au 200 mesh	Quantifoil
Holey Carbon Films R2/1 Cu 200 mesh	Quantifoil
Holey Carbon Films R2/1 Cu 200 mesh + 5 nm C	Quantifoil
C-Clips and C-Clip Rings	Thermo Fisher Scientific
Resolution Standard Test Samples	
Grating Replica, crossed line	Science Services
Latex Spheres on Grating Replica	Science Services
Gold Particles on Carbon Film	self made

Table 3.4: Instruments used for this thesis.

Instrument	Manufacturer	Name
Cryo Chamber	Leica Microsystems	EM UC7 / EM FC7
Quartz Film Thickness Monitor	BAL-TEC	QSG 100
Phase-Plate System	KonTEM	PhazR
Pipettes	Eppendorf	Research Plus
Plasma Cleaner I	BAL-TEC	MED 010
Plasma Cleaner II	Fischione Instruments	Model 1020
Plasma Cleaner III	ibssGroup, Inc.	GV10x
Plunge Freezer	Leica	EM-GP II
Sputter coater	BAL-TEC	MED 020

Sputter Coater BAL-TEC MED 020

For the fabrication of the PP, thin metal films of only a few nanometers are essential. Here, thin metal layers were produced by magnetron sputtering, a vacuum coating technique. Figure 3.1 shows the principle of the magnetron sputter coating process.

An argon plasma is created inside the reaction chamber by applying a high voltage between the anode ring and the target disk. The target is bombarded with energetic argon ions and by forceful collision of these ions with the target, metal atoms are ejected from the target into the vacuum chamber. These metal atoms further collide with residual argon atoms present in space. They lose kinetic energy, condense on the substrate and thereby form a metallic film. The target is cooled by water to minimize the radiation heat [68]. This stabilizes the process and allows longer sputtering times.

For the experiments described in this thesis, the sputter coater BAL-TEC MED 020 (*BAL-TEC*) was used. The high-vacuum coating system is equipped with an oil free vacuum pump system, consisting of a membrane pre-pump and a turbo molecular pump for high vacuum down to 10^{-7} mbar. Prior to each coating process, the reaction chamber was evacuated to a pressure of $< 1 \times 10^{-6}$ mbar. For sputter coating, Ar (purity grade 6.0) was injected into the reaction chamber by an electromagnetic needle valve to a final reaction pressure between 5×10^{-3} mbar and 5×10^{-2} mbar.

The high voltage system of the magnetron operates at a fixed voltage of 5 kV and a sputtering current of maximum 120 mA. The sputter rate can be set by tuning the reaction pressure, the sputtering current and the distance between the target disc and the substrate. For measuring the sputter rate and the final deposit layer thickness, the system is equipped with an oscillation quartz sensor QSG 100 (*BAL-TEC*).

For cleaning the target disc and stabilizing of the system settings, the MED 020 uses a mechanical shutter. This shutter separates the magnetron from the reaction chamber and prevents contamination of the substrate.

In a typical coating experiment, the substrate was placed on a glass slide. The target disc was mounted on the magnetron. The mechanical shutter was closed and the reaction chamber was evacuated to a pressure of $< 1 \times 10^{-6}$ mbar. Afterwards, the process parameters were set and argon was injected into the reaction chamber. The process was started and the shutter was kept close to allow a process stabilization. Once coating conditions had stabilized, the shutter was opened and the coating process started. To achieve a more precise layer thickness, the coating process was monitored and interrupted by manually closing the mechanical shutter. After that, the coating process was stopped and the reaction chamber was carefully vented.

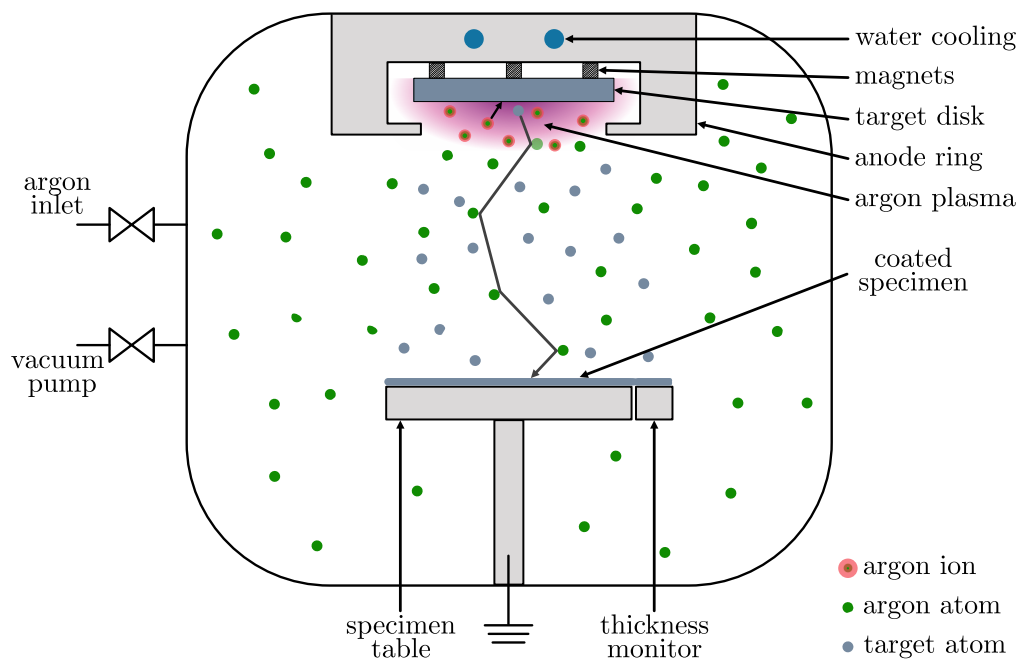


Figure 3.1: Basic mechanism of magnetron sputtering of the BAL-TEC MED 020. Plasma is generated by applying high voltage between the anode ring and the target. Argon ions are accelerated towards the target disk where by forceful collision of the ions with the target, metal atoms are ejected into the vacuum chamber where they condense on the sample. Thickness can be monitored by an oscillation quartz sensor.

FEI Titan Krios Transmission Electron Microscope

All cryo datasets were recorded using an FEI Titan Krios (*Thermo Fischer Scientific*) cryo-TEM. The FEI Titan Krios is a high-resolution cryo-TEM. SPA or tomography are only two of the main applications of the Titan Krios TEM to characterize three-dimensional structures of biological samples.

The Titan Krios at caesar is equipped with a Schottky FEG. The acceleration voltage can be set between 60 kV and 300 kV. A three lens condenser system provides parallel illumination of the sample over a wide and variable field of view, which is essential for cryo-electron tomography and SPA. The first condenser lens (C1) defines the spot size by the beam current. An increase of the spot size by one step leads to a reduction of the beam current by 50%. Changes of the second condenser lens (C2) result in a change of beam diameter and therefore in the size of the illumination area. The third condenser lens (C3) is continuously adjustable in a change of size and guarantees a parallel illumination and effectively minimizes off-axis coma. Normally, C2 and C3 are changed simultaneously. For manual fine tuning, the C3 lens can be varied within certain ranges by the *MF-Y Fine Focus Back Focal Plane* setting. This function is important to fine-tune the position of the diffraction plane, which is essential for focussing the PP in the back focal plane. The Titan Krios has an additional lens in the condenser system, the minicondenser lens. This lens demagnifies the beam and allows illumination areas five times larger. For cryo application it is essential to work with a very small illuminated area. The minicondenser lens can be switched off by selecting nanoprobe mode. This setting allows smaller illuminated areas, which is important to protect cryo-samples from further beam damage.

The TEM has an automated robotic specimen handling system (autoloader) with a capacity of 12 samples. The samples are mounted in special designed autogrid rings (*Thermo Fischer Scientific*), which are essential for the automated handling of the samples. Cryo-sample exchange can be done contamination-free and fully automated without manual interaction of the user.

The TEM is equipped with a C_s corrector, to correct for aberrations up to the 3rd order (spherical aberration). This is crucial for PP data acquisition. PPs undergo the process of ageing, which results in a charging of the PP. Charging of the PP, causes the PP to act like a lens [31, 32]. To facilitate the correction of aberrations produced by the PP, a TEM equipped with a C_s corrector is essential for this work.

A high speed digital camera (flu cam) replaces the typical fluorescent screen, which is normally used for adjustments and fast screening of the sample. For data acquisition the Titan Krios holds three detectors. The Orius SC1000 (*Gatan*), a scintillator based CCD¹ camera, is used to acquire images at low magnification. For high resolution images, a 4k x 4k CMOS² Falcon II DED (*Thermo Fischer Scientific*) is used, which records 17 frames per second. Furthermore, the microscope is equipped with a post-column GIF³ energy filter (*Gatan*), which is used for energy filtered imaging and spectroscopy applications.

Furthermore, the Titan Krios at caesar is equipped with the KonTEM phase-contrast system PhazR (*KonTEM GmbH*) for PP experiments. This system allows insertion of various types of PPs into the beam path of the microscope. All PP experiments described in this thesis were done using this PP system. A more detailed description of PhazR can be found in chapter 3.1.

The Titan Krios can be operated remotely to set up automatic acquisition. All functions apart from loading the sample cassette into the microscope can be set remotely. [69]

¹Charge-Coupled Device

²Complementary Metal-Oxide-Semiconductor

³Gatan Imaging Filter

KonTEM Phase-Plate System *PhazR*

KonTEM, a spin-off from the research center caesar and the Max-Planck-Society was founded in April 2010. After a successful development of the phase-plate system PhazR for various TEM models and the first installation into the FEI Titan Krios at caesar [70], KonTEM was sold to the FEI Company (now *Thermo Fisher Scientific*) in May 2014.

PhazR consists of two main components: the PP and an automatic nano-positioning mechanism controlled by the software KonTROL [71]. The KonTEM phase-plate system replaces the standard objective aperture system as the PP has to be positioned in the back focal plane of the TEM. The PhazR tip shown in figure 3.2 (A) holds four positions for apertures or PP grids. The first position is usually occupied by an objective aperture whereas the other positions are used for PP grids. The PP tip can be heated up to 100 °C by a PTC⁴ heater. The gap in the TEM column, where the PP system is installed, is very small (typically 100-200 µm) and the PP or parts of the TEM can be easily harmed. To prevent any damage, the system includes a touch alarm. In case the tip touches the column inside the microscope an acoustical signal occurs to alert the user to stop moving the PP.

Figure 3.2 (B) shows a CAD⁵ drawing of the KonTEM positioning device. It consists of three main components: a positioning rod for mounting the PPs or apertures, three piezo motors to position the rod inside the TEM column and a flange to fit the positioning system into the TEM column. Figure 3.2 (A) shows the adaption of the flange to the FEI Titan Krios TEM whereas the CAD drawing shows the modulation for the JEOL JEM-2200FS TEM (*JEOL*). Due to the modular design, only the front yellow part had to be adapted according to the TEM design.

⁴Positive Temperature Coefficient

⁵Computer-Aided Design

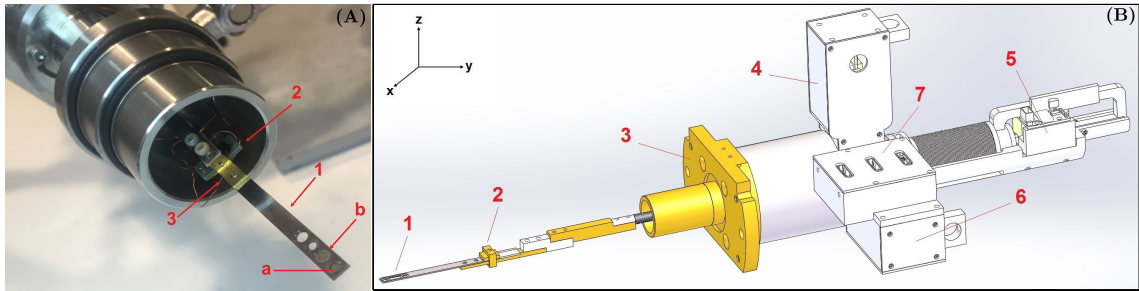


Figure 3.2: (A) Image of the KonTEM PP system for the FEI Titan Krios TEM showing (1) the tip of the holder. An objective aperture is installed in the first position of the tip (a). The second position is occupied by a PP grid (b). (2) shows the installed PTC heating element for the PP tip and (3) the touch alarm. (B) CAD drawing of the KonTEM PP system for a JEOL JEM-2200FS TEM showing: (1) tip of the positioning holder, (2) PTC heating element, (3) vacuum flange for JEOL JEM-2200FS TEM, three piezo leg motors: (4) Z, (5) Y, (6) X and (7) connections to the control computer [72].

The positioning system consists of three piezo leg motors (*PiezoMotor Uppsala AB*). Compared to standard stick and slip piezo drives, the leg motors allow higher forces along the motor axis [73]. The higher force is needed as the piezo leg motors have been installed outside the TEM column and the motor for the x-direction has to overcome the force by the vacuum inside the TEM [70].

All motion functions of the piezo leg motors are controlled by the KonTROL software. Figure 3.3 shows the KonTROL 1.9 user interface, which allows a user-friendly application of the PP system. The Python based software can store and recall up to 65 PP and five aperture positions. Light blue buttons indicate a stored position, pink stands for the actual selected and gray for available positions. The arrangement of the preset positions in the graphical user interface (fig. 3.3(A)) is based on the original KonTEM silicon wafer PP design, which was given up for experiments of this thesis. Here the positions 1 - 65 are used as random preset positions.

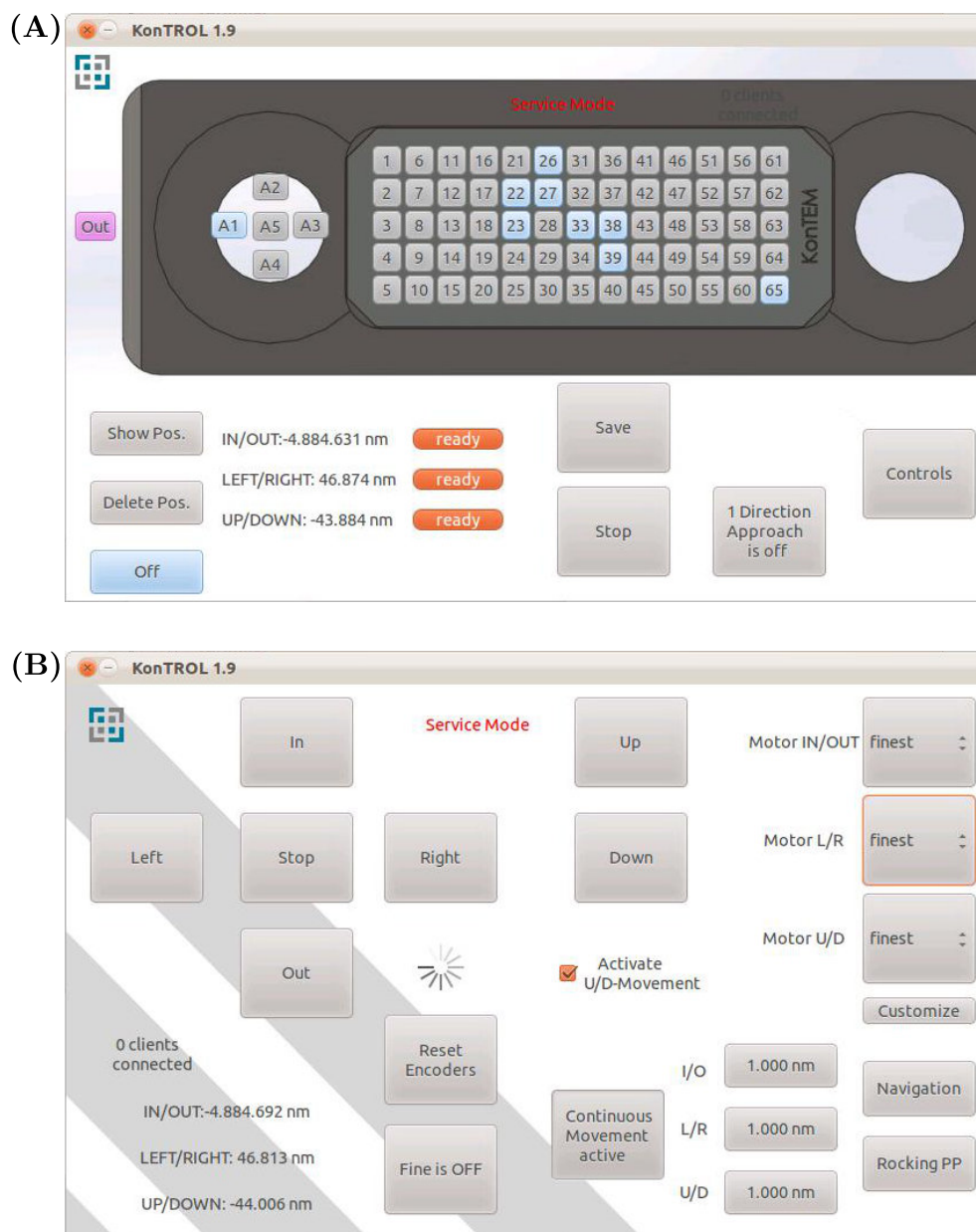


Figure 3.3: Graphical user interface of the KonTROL 1.9 software. (A) Up to 65 PP positions can be saved and recalled. Blue color indicates saved, pink current and gray available positions. (B) User interface for manual positioning of the PP in all spatial directions including an independent selection of motor speed.

The movement of the positioning system can be controlled in all spatial directions with a 60 nm precision [70]: up/down, left/right and in/out. The software also allows the selection of four different positioning-speeds (finest, fine, medium, fastest) for each motor (fig. 3.3 (B)).

As an additional feature the ‘*rocking*’ technique has been implemented into the KonTROL software. This ‘*rocking*’ mode allows a rotation of the PP in the back focal plane of the microscope column. Additional parameters can be set in the KonSHAKER task bar (fig. 3.4) to optimize the rotation on a circular path: circle-width, rotation speed and aspect ratio [74].

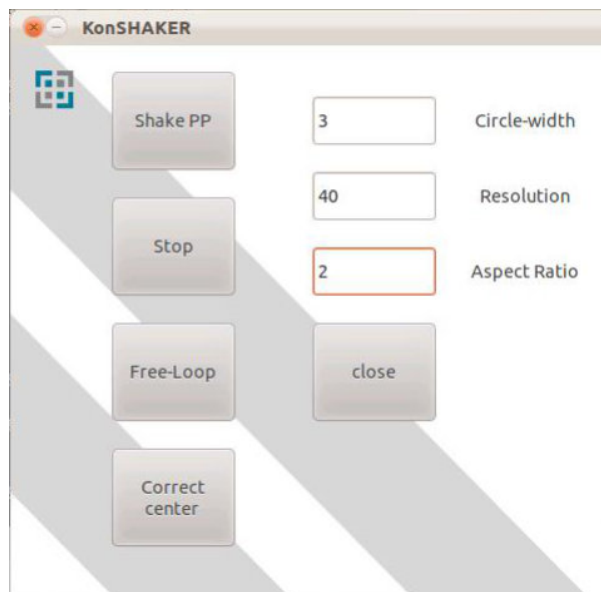


Figure 3.4: Graphical user interface of KonSHAKER. Three parameters can be set to control the circular rotation of the PP.

Zeiss Crossbeam XB1540 Workstation

In this work, a Zeiss Crossbeam XB1540 workstation (*Carl Zeiss AG*) was used for the fabrication of PP.

The Zeiss Crossbeam is a dual beam workstation with a Focused Ion Beam (FIB) and a Scanning Electron Microscope (SEM) column aligned to each other enclosing an angle of 54° . The beam crossing point is located about 5 mm below the vertically aligned SEM column. For simultaneous ion milling and electron imaging, the sample has to be set to the crossing point of both beams. The Zeiss Crossbeam workstation is equipped with a Schottky field emission electron emitter for the electron beam and an *Orsay Physics* Canion column (*Orsay Physics*) for gallium (Ga^{2+}) ions. The beam current of the FIB can be selected in fixed steps according to table 3.5. Beam current steps are generated by a combination of the FIB condenser lens settings and the beam forming aperture. These presets are calibrated by the service. The instrument has five apertures and 11 FIB current presets between 2 pA and 10000 pA. For the experiments herein, the preset of 50 pA and a FIB acceleration voltage of 30 kV was set. The acceleration voltage of the SEM can be set between 100 V and 30 kV. Typically the voltage was set to 2 kV for electron images in this work. The Zeiss Crossbeam workstation holds two detectors for imaging. A standard SE2 detector for secondary electron detection and an in-lens detector for small angle scattered secondary electrons. The ETD⁶ detector gives good detection of sample topography while the in-lens detector gives chemical information about the sample surface. Both detectors can be used for ion as well as electron images.

The scan system of FIB and SEM is 12 bit. This allows a maximum number of pixels of 3496 x 2048. For a PP hole of 2 μm diameter, this is not enough to ensure a smooth curvature. Therefore a second external scan system with 16 bit resolution was used (Raith Elphy Plus, *Raith GmbH*). This allows 65536 x 65536 pixel resolution. The Raith system was used for all experiments described in this work.

⁶Everhard-Thornley Detector

Table 3.5: Zeiss Crossbeam XB1540 Workstation settings

Aperture [μm]	Condenser [V]	Probe Current [pA]
30	12347	2.0
30	8880	10.0
30	5565	20.0
50	5848	50.0
50	5191	100.0
150	12173	200.0
150	7044	500.0
150	5005	1000.0
200	4815	2000.0
400	6831	5000.0
400	4983	10000.0

JPL NanoWizard Atomic Force Microscope

Atomic force microscopy was used in this thesis to verify the thickness of the PP films. The Atomic Force Microscope (AFM) installed at caesar is a JPK NanoWizard3 system (*JPK Instruments AG*). The AFM is installed on the manual stage of an inverted optical microscope (IX73, *Olympus*). For live imaging, and setting up the laser in transmission mode, the IX73 is equipped with an CCD camera (IMAGINGSOURCE DFK 31 BF03.H, *The Imaging Source Europe GmbH*). For setting up and live imaging in reflection mode, an identical CCD camera is mounted on a JPK optical microscope setup that can be moved into the beam path. Both cameras are controlled by the JPK NanoWizard Control SPM software (*JPK Instruments AG*). The top view camera is also used to adjust the laser on the cantilever. To minimize environmental influences, the microscope is mounted on an active anti-vibration table (accurion HALCYONICS.i4, *Accurion GmbH*) and inside a wooden enclosure against acoustic noise (*caesar, mechanical workshop*). The complete AFM setup is mounted on a granite table.

For experiments in this work, JPK NanoWizard3 was used in contact mode using commercial sharp microlever probes (MSNL-10 manufactured by *BRUKER*) made of silicon nitride with six cantilevers of a thickness between 0.5-0.6 μm .

The AFM cantilever is raster-scanned across the sample surface. In contact mode, the AFM tip is continuously in contact with the sample surface. The cantilever is deflected relative to the sample surface topography. The laser light is reflected by the backside of the cantilever onto a four-segment photodiode. The deflection of the laser beam from the center of the detector is measured and fed back to a computer and transformed into a height information. [75, 76]

3.2 Methods

In the following chapter, the workflow for SPA is described, starting with sample preparation including protein purification and cryo-sample preparation using plunge freezing and is followed by data acquisition and data reconstruction (fig. 3.5).

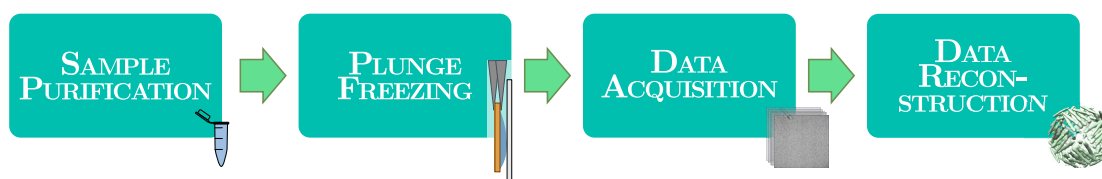


Figure 3.5: Schematic overview of the single particle analysis workflow from the protein sample to the three-dimensional structure of the protein. Beginning with the protein purification followed by plunge freezing and creating a cryo-sample. In the next step data have to be acquired at a cryo-TEM and processed in several data reconstruction steps to finally get the three-dimensional structure of the protein.

3.2.1 Sample Preparation

Sample preparation is the first essential step for a successful SPA. In the following, the methods of protein purification and plunge freezing are described in more detail.

Protein Purification of Horse and Mouse Apoferritin

Apoferritin was used for all single-particle experiments described in this work. Apoferritin is an iron-storage protein and is present in many living organisms. Apoferritin from horse (*equus caballus*) and mouse (*mus musculus*) apoferritin were used for the experiments.

Horse Apoferritin

For the experiments in the early stage of this thesis, horse (equine spleen) apoferritin (A3641) from Sigma-Aldrich (*Sigma-Aldrich*) was used. Protein parameters, according to the ProtParam analysis⁷ of ferritin heavy chain equus caballus, and ferritin light chain equus caballus can be found in appendix A.1 and A.2.

The protein was purified by Size-Exclusion Chromatography (SEC), using a Superose 6 10/300 column (*GE Healthcare*) equilibrated in TBS⁸ (150 mM NaCl, 50 mM Tris-HCl, pH 7.5). Three peak fractions corresponding to the highest purity of apoferritin (B/13, B/14, B/15, fig. 3.6) were concentrated to 6 mg/ml in TBS. Aliquots of purified apoferritin were flash frozen in liquid nitrogen and stored at -80 °C.

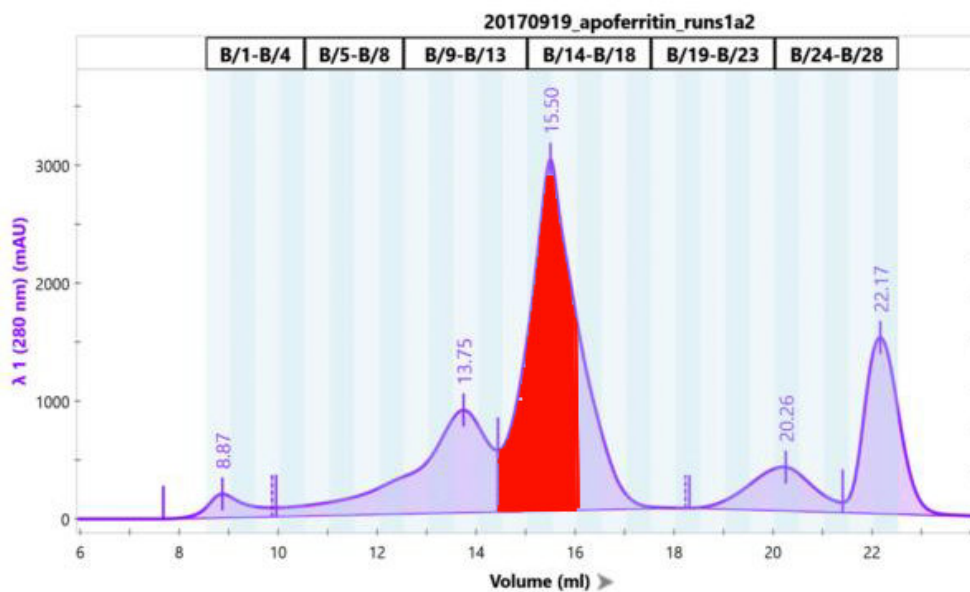


Figure 3.6: Purification of equine spleen apoferritin via SEC. SEC purification using a Superose 6 10/300 column (*GE Healthcare*). Protein eluted in one peak with retention volume of 15.5 ml. Absorption at 280 nm in arbitrary units is plotted versus elution volume in ml. Three peak fractions (B/13, B/14, B/15) were pooled and concentrated to 6 mg/ml in TBS.

⁷The ProtParam tool analyses physico-chemical properties of proteins [77].

⁸Tris-buffered saline

Mouse Apoferritin

For later experiments at higher resolution, mouse apoferritin was used, as the resolution of horse apoferritin is limited to 3.5 Å [78]. Protein expression and purification of mouse (*mus musculus*) apoferritin were adapted to the protocol of M. Wu et. al [64]. Protein parameters of ferritin heavy chain *mus musculus* can be found in appendix A.3.

A pET24a vector encoding the heavy chain of mouse apoferritin was received from M. Kikkawa (University of Tokyo). The vector was transformed into BL21(DE3) *E. coli* chemically-competent cells without modification. Cells were grown at 37 °C in LB media until an $OD_{600\text{nm}} = 0.5$ was reached. Protein expression was induced with 1 mM IPTG⁹ at 37 °C. After 4 hours, the culture was harvested at 3000 rpm for 20 min. The pellet was resuspended in lysis buffer (20 mM HEPES-NaOH pH 7.5, 300 mM NaCl, 1 mM MgSO₄), supplemented with lysosome to a final concentration of 1 mg/ml (1:100) and DNase I to a final concentration of 5 µg/ml (1:2000). Cell debris were centrifuged at 70,000×g for 30 min (10 °C) and the supernatant was heat-treated at 70 °C for 10 min to denature endogenous *E. coli* proteins. Denatured proteins were pelleted at 70,000×g for 30 min (4 °C). Ammonium sulfate was then added to the supernatant to a final concentration of 52.5% while gently stirring at 4 °C for 10 min. The precipitant was harvested at 50,000×g for 20 min (4 °C), gently resuspended in 2 ml buffer (20 mM HEPES-NaOH pH 7.5, 300 mM NaCl) and subsequently dialyzed in buffer (20 mM HEPES-NaOH pH 7.5, 300 mM NaCl) at 4 °C over night. The dialyzed protein was concentrated to a volume of 1 ml using 30 kDa MWCO¹⁰ concentrator at 1000×g for 5 min. The protein was further purified by SEC using a HiLoad 16/600 Superdex 200 column (*GE Healthcare*) equilibrated in buffer (20 mM HEPES-NaOH pH 7.5, 300 mM NaCl) (fig. 3.7). Peak fractions of apoferritin were pooled corresponding to 5-20% SDS-PAGE¹¹ analysis (fig. 3.8) and concentrated to a final concentration of 7-8 mg/ml using a 30 MWCO concentrator. Aliquots of purified protein were flash frozen and stored in liquid nitrogen.

⁹Isopropyl β-d-1-thiogalactopyranoside

¹⁰Molecular weight cut-off

¹¹sodium dodecyl sulfate polyacrylamide gel electrophoresis

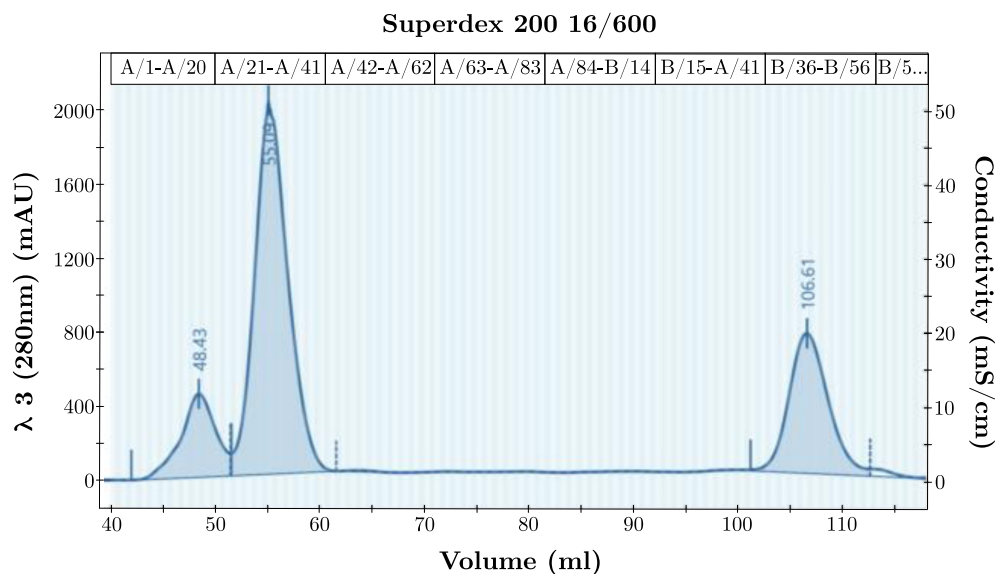


Figure 3.7: Purification of mus musculus (mouse) apoferritin via SEC. SEC purification using a Superdex 200 16/600 column (*GE Healthcare*). Protein eluted in three peaks with retention volume of 48.43 ml, 55.09 ml and 106.61 ml. Absorption at 280 nm in arbitrary units, is plotted versus elution volume in ml. Fractions A26 - A40 were pooled and concentrated to 7 - 8 mg/ml.

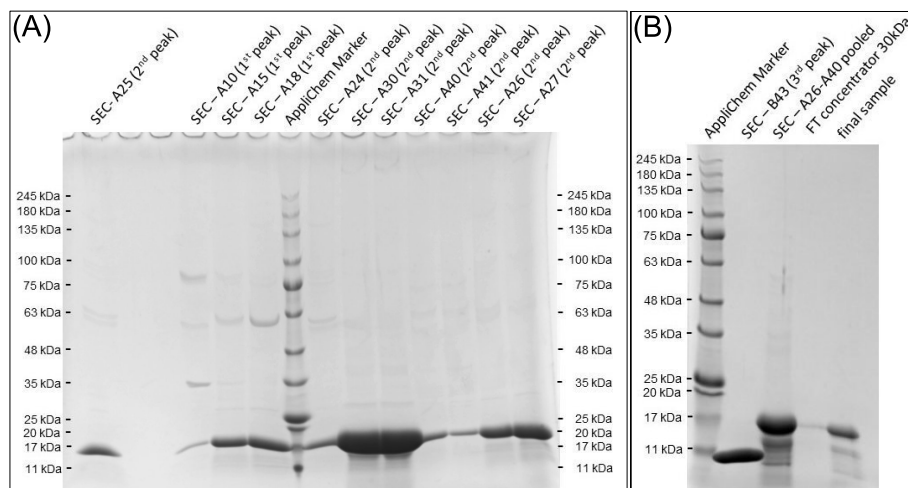


Figure 3.8: (A) 5-20 % SDS-PAGE of SEC fractions: A10, A15, A18 (1st peak), A24, A25, A26, A27, A30, A31, A40, A41 (2nd peak); (B) 5-20 % SDS-PAGE of SEC fractions: B43 (3rd peak) and A26 - A40 pooled (2nd peak). Fractions A26 - A40 were pooled and concentrated to 7 - 8 mg/ml.

Plunge Freezing

Plunge freezing was performed using a Leica EM-GP II plunger (*Leica Microsystems*). The Leica EM-GP II plunger allows the control of various settings such as humidity and temperature inside the blotting chamber or three different blotting times: pre-blot, blot-time and post-blot time. In addition, the Leica EM-GP II comes with an integrated sensor to automatically control force and blotting time. The various adjustments make the result as reproducible as possible.

For the preparation of apoferritin grids, humidity, temperature and blotting times were set according to the parameters listed in table 3.6, which have been previously determined in several trials. Holey carbon grids (R1/2, 200 mesh) (*Quantifoil*) were freshly plasma-cleaned for two minutes using an Argon plasma cleaner MED 010 (*Balzers*). 4 μ l sample solution (4.5 μ l apoferritin 6 mg/ml in TBS + 0.5 μ l 0.1% fOM [10 mM HEPES pH 7.4, 150 mM NaCl]) were applied onto the hydrophilic grid in a temperature and humidity controlled chamber. Automated blotting was performed for 2-3 seconds using Whatman filter paper grade 2 (*Whatman*). The integrated sensor was activated to control the force and blotting time. The samples were immediately plunge-frozen into liquid ethane, cooled down to -175°C using liquid nitrogen. Grids were kept for one minute in liquid ethane to avoid devitrification before being stored in a grid box in liquid nitrogen at -196°C .

For the transfer into the Titan Krios TEM (*Thermo Fisher Scientific*), grids have to be mounted in special carriers, Autogrid rings (*Thermo Fisher Scientific*). Therefore grids were clipped at -170°C in a cryo chamber of an Ultramicrotome UC7 (*Leica Microsystems*). Samples were stored in liquid nitrogen or transferred into the Titan Krios TEM for sample quality check or data acquisition.

Table 3.6: Plunge freezing parameters for apoferritin.

Leica EM-GP II	
humidity	95 %
temperature	20 °C
pre-blot	0 s
blot-time	2 - 3 s
post-blot	0 s
sensor	yes
sample volume	4 μ l

3.2.2 Cryo-Transmission Electron Microscopy Grids

For cryo-sample preparation, Quantifoil Holey Carbon 1/2 Cu 200 mesh TEM grids (*Quantifoil*) were used. Figure 3.9 shows a light microscopy image of this grid at three different magnifications. TEM grids have a diameter of 3.05 mm. The metal meshes support a thin film, here a perforated carbon film of 10-12 nm. The number of meshes across the grid is defined by the number of squares in one inch, e.g. a 200-mesh grid has 20 squares in each direction [79]. The Quantifoil Holey Carbon 1/2 grid has a hole diameter of 1 μ m and a spacing in between the holes of 2 μ m shown in the figure 3.9. During plunge freezing a very thin amorphous ice layer is formed on the carbon film, filling the holes with proteins embedded in vitrified ice (chapter 3.2). Images are acquired inside the holes as the thin amorphous carbon film can scatter electrons inelastically and contribute to background noise. In this work, various TEM grids listed in table 3.3 have been used for cryo-sample preparation (chapter 3.2) or PP fabrication (chapter 4.1.2).

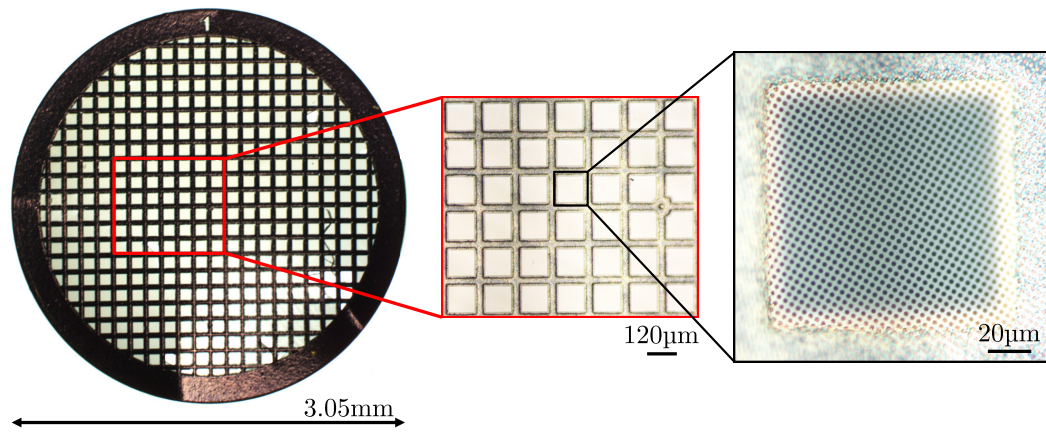


Figure 3.9: Light microscopy images of a Quantifoil Holey Carbon 1/2 Cu 200 mesh TEM grid at three different magnifications (10x, 25x and 50x magnification). The images show the TEM grid with a diameter of 3.05 mm with 200 meshes divided by grid bars and the perforated carbon support film with 1 μm holes and a spacing of 2 μm between the holes.

3.2.3 Single-Particle Data Acquisition Workflow

Once sample preparation is finished, the process continues with data acquisition. Various software for automated SPA and transmission electron tomography have been developed in the early 2000s [80, 81].

In this work, the freely available software, Leginon is used for automated single particle acquisition. Leginon was first developed in 2000 and got redesigned changing to the programming language Python in 2005. It was the first software that integrated the control of the electron microscope and image acquisition with machine vision algorithms to run a fully automated data acquisition [82].

Leginon (version 3.1) was used for SPA. The software is operated via a graphical user interface and can run unattended for several days. Various microscope settings can be saved in the software and recalled at a later time. A set of parameters can be selected and the microscope changes the parameters such as magnification, illumination area, spot size and exposure time according to the previously saved parameters of that setting. This allows a fast change between magnifications, which is essential for the SPA workflow. Leginon offers various workflows to select from, but also allows for changes or completely new workflows.

One of the predefined workflows is MSI¹²-Edge, used for SPA. A prerequisite of the MSI-Edge workflow is a couple of presets (tab. 3.7). These presets are used to acquire an overview atlas of the complete grid (gr) and images of individual grid meshes (sq) at low magnification, images of the sample filled holes in the carbon film (hl) at an intermediate magnification and exposure images (ef) at high magnification. Two additional setups are required to set the correct defocus (fc) and eucentric height (eu). All presets described in table 3.7 are optimized for the Titan Krios at caesar. They can vary depending on the desired target resolution as well as on the microscope setup.

In the following, the MSI-Edge (3.0) workflow integrated in Leginon, is described. Figure 3.11 shows an overview of the five different steps of the workflow.

¹²Multi-Scale Imaging

Previous to the acquisition setup, cryo-samples were transferred into a Titan Krios TEM (*Thermo Fisher Scientific*) operating at 300 kV in nanoProbe mode. Sufficient ice quality and protein concentration were ensured by screening of the samples at low dose settings of the microscope.

In the first workflow step, micrographs were acquired at low magnification (81x). These low magnification images were automatically stitched together by the Legion software to an **ATLAS** image of the whole grid (fig. 3.11(A)).

The resulting mosaic was used in the second step (**SQUARE TARGETING**) to find and select usable meshes for acquisition (indicated by green cross in fig. 3.11 (A)). In the third step, holes covered with amorphous ice of a suitable thickness were automatically identified or manually selected in images acquired at 165x magnification (**HOLE TARGETING** fig. 3.11 (B), green crosses). To compensate for height variations of the grid, an additional focussing target was selected in the center of each mesh, indicated by blue cross. This was used to determine the eucentric (mechanical) focus for each mesh.

Micrographs recorded at a magnification of 6500x (9.93 Å/pixel) were used to set targets during the **EXPOSURE TARGETING** step (green crosses in fig. 3.11 (C)). Exposure targets were set automatically or selected by the user. Depending on the hole diameter and microscope settings, up to three exposure targets per hole were possible at the Titan Krios at caesar. Furthermore, a focus target was set next to the target hole on the carbon film (blue cross in figure 3.11 (C)) to adjust the defocus. For this work, the focus was remeasured every three micrographs using low dose focus settings (ef).

In the final **EXPOSURE** step, movies with 51 frames were acquired at 59000x (1.06 Å/pixel) magnification at each exposure target position (fig. 3.11 (D)).

Simultaneously, with data acquisition, the recorded micrographs are fed into a pipeline for motion correction and a first quality assessment. The complete pipeline is controlled by a set of python scripts, written by Elmar Behrmann and Stephan Irsen at caesar. All scripts give a first quality information about the sample and images during the process of data acquisition. The scripts calculate outputs for defocus, astigmatism and resolution. Results are presented in a graph representation allowing for a faster inspection of the acquisition quality. Fig. 3.10 shows a typical

output of the preprocessing script. This allows an interfering with the data acquisition while it is running. A detailed description of the individual pre-processing steps is given in chapter 3.2.4.

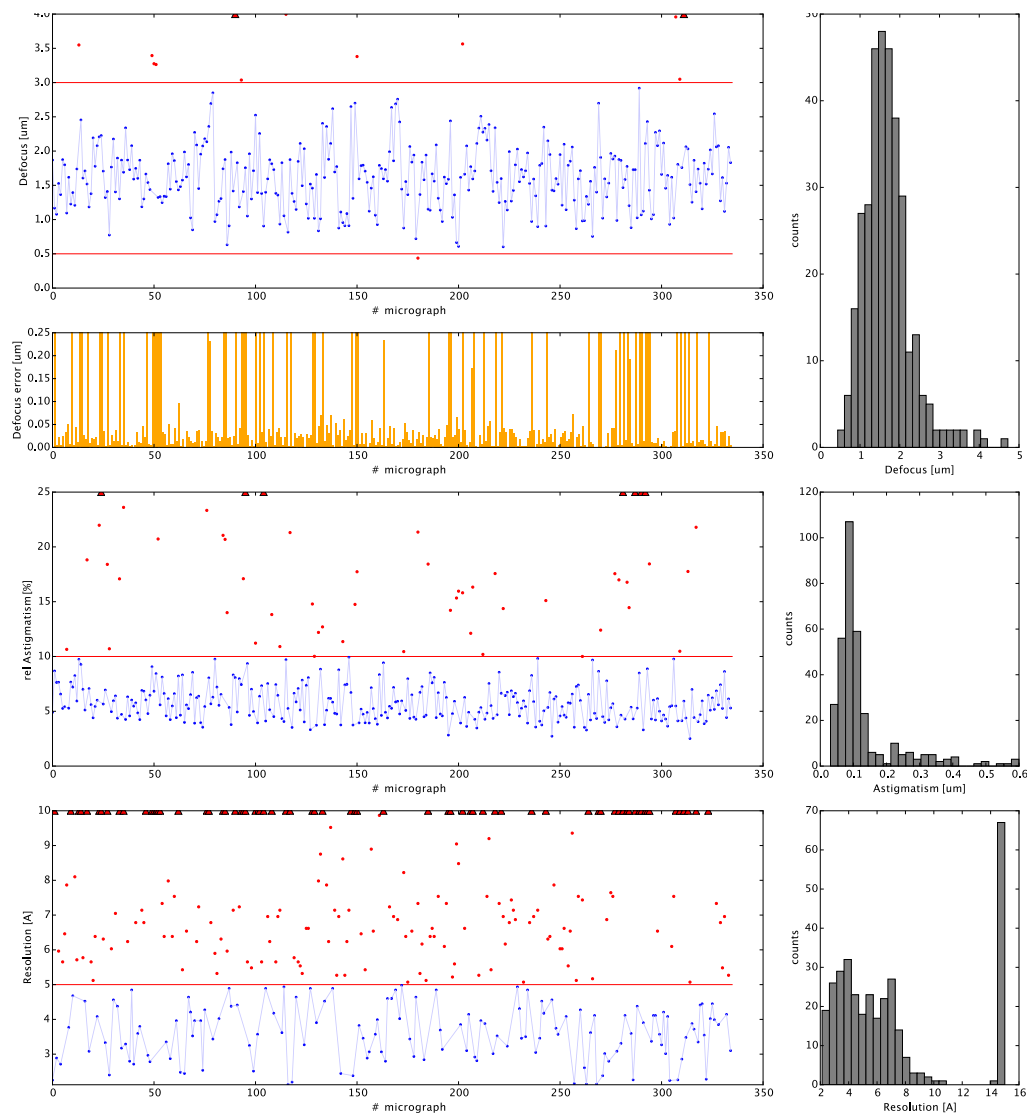


Figure 3.10: Example of a typical output of the preprocessing script of an apoferritin dataset. The output gives information about defocus, astigmatism and resolution. The red lines of the diagrams indicate the threshold.

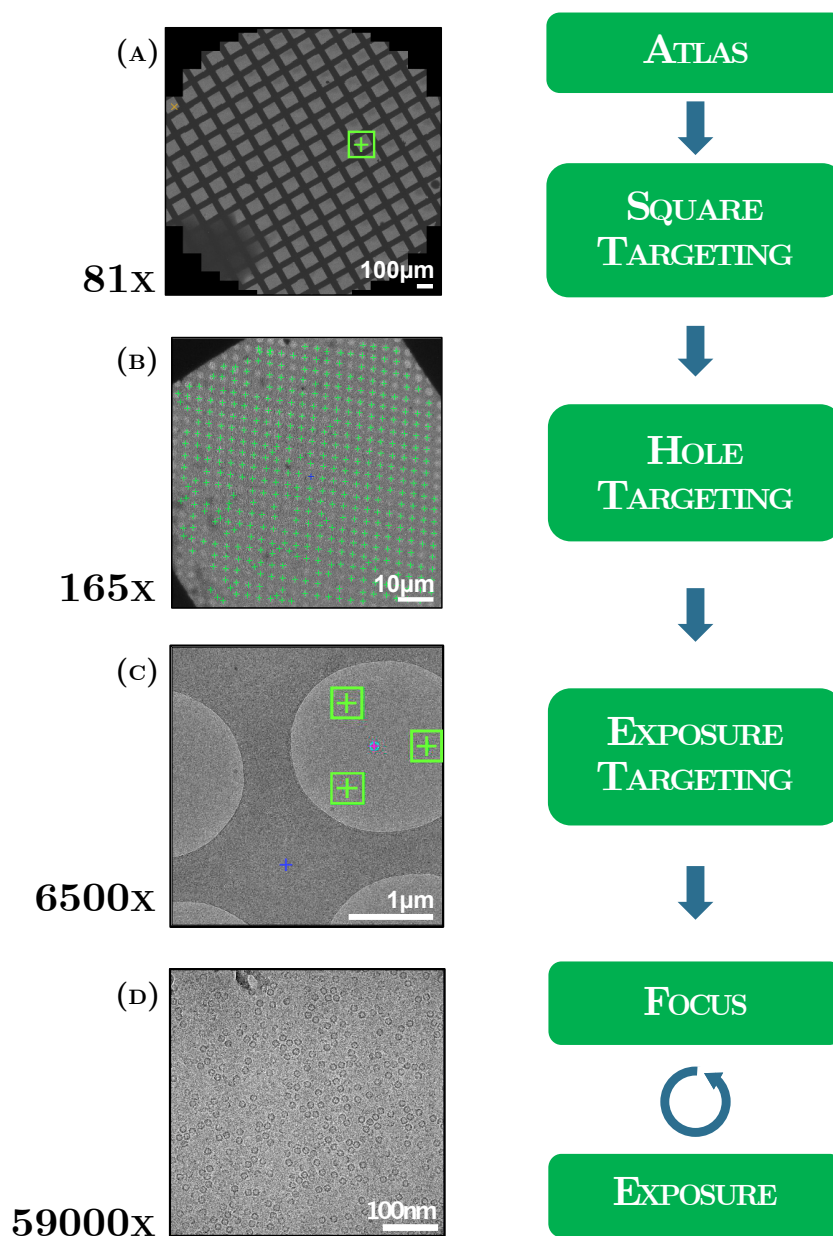


Figure 3.11: Schematic overview of the standard MSI-Edge acquisition workflow using Leginon 3.1. (A) The ATLAS is a composition of several low magnification images acquired at 81x magnification. Meshes for further acquisition are selected indicated by green cross. (B) Low magnification images at 165x. Holes with suitable ice thickness are manually or automatically selected shown by green crosses. Blue cross indicates the position for an eucentric height focus determination. (C) Image acquired at 6500x intermediate magnification showing a complete hole filled with thin amorphous ice. Green boxes indicate the position for high magnification exposure images. Blue cross stands for the position of the focus target. (D) Final exposure image acquired at 59000x magnification showing apoferritin proteins embedded in vitreous ice.

Table 3.7: Microscope settings used in this work for the Legikon MSI-Edge 3.0 workflow at the Titan Krios TEM at caesar. The presets can vary depending on the desired target resolution as well as on the microscope setup.

Preset Name	gr	sq	hl	ef	fc	eu
MSI-Edge Function	ATLAS	Square Targeting	Hole Targeting	Exposure	Focus	Eucentric Focus
Magnification	81x	165x	6500x	59000x	59000x	3800x
Pixel Size [nm]	-	-	0.993	0.106	0.106	1.720
Spot Size	8	8	9	6	6	10
Illumination Area [μm]	1000	700	8	1.25	0.8	12.5
Exposure Time [ms]	500	1500	500	3000	1000	3000
Detector	Orius CCD	Orius CCD	Falcon II	Falcon II ¹³	Falcon II	Falcon II

¹³in frame read out mode 17 frames/second

3.2.4 Data Reconstruction

For three-dimensional protein structure determination, based on cryo-EM data, these data are processed in various steps. Figure 3.12 shows a schematic overview of a reconstruction workflow following the RELION¹⁴ pipeline [83].

RELION is an open-source software for 3D structure determination by SPA of cryo-EM data and was first introduced in 2012 [84]. RELION uses a Bayesian approach to infer parameters of a statistical model from the data. This allows high-quality reconstructions and reliable resolution estimates with minimal user intervention [85].

In this work, RELION version 3.1-beta was mainly used for single-particle data reconstruction. Additionally, also programs from other reconstruction packages like SPHIRE [86] or EMAN2 [87] were used for selected tasks in this workflow. All programs used for data reconstruction herein are listed in table 3.8.

Table 3.8: Software used for single particle data acquisition, processing and reconstruction.

Software	Version
crYOLO [88, 89]	1.6.0
CTFFIND4 [90]	1.14
EMAN2 [87]	2.21
Gctf [91]	1.06 & 1.18
Gautomatch [92]	0.56_sm62_cu8
KonTROL	1.9
Leginon [80]	3.1
MotionCor2[93]	1.2.0
RELION [83]	3.1-beta
SPHIRE [86]	1.3
UCSF Chimera [94]	1.14
Fiji [95]	2.1.0/1.53c

¹⁴REgularized Likelihood OptimizatiON

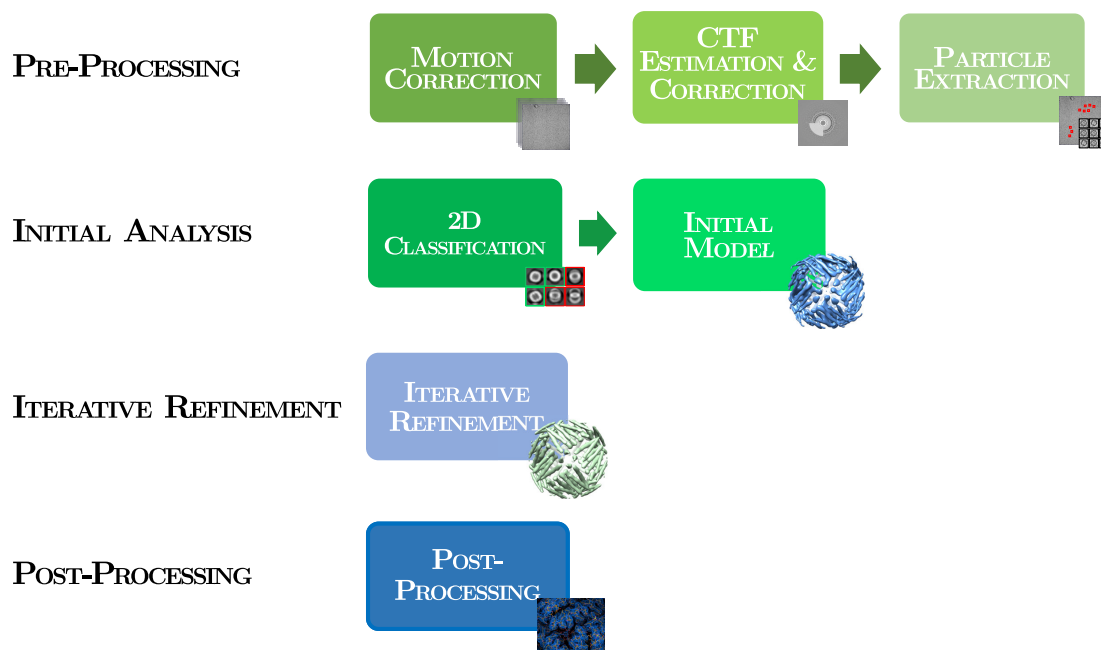


Figure 3.12: A schematic overview of the data reconstruction pipeline in RELION. The workflow can be classified in four major processing steps. **Pre-processing** consists of beam-induced motion correction, CTF estimation and correction and particle picking and extraction. The **initial analysis** steps include 2D Classification to remove false positives and the creation of an initial model. During the **iterative refinement**, a 3D classification is performed where particles are grouped based on their similarity. With sufficient homogeneity, the fully automated 3D auto-refinement is started to receive a refined three dimensional structure. The 3D model of the protein further sharpened by the post-processing to improve and estimate the final resolution of the protein structure.

Pre-Processing

The first step of the processing pipeline is a pre-processing of the acquired frame movies. All images are corrected for beam induced motion. Therefore, **MOTION CORRECTION** is performed using the software MotionCor2 [93]. MotionCor2 combines the correction of uniform whole-frame motion and anisotropic local motion, to calculate an average of every image. Motion correction takes a lot of processing time and therefore it runs parallel to data acquisition (chapter 3.2.3).

Before further processing, micrographs are manually checked using e2boxer (EMAN2) [87]. Bad Micrographs showing ice contamination, no ice or too much carbon film, were discarded at this step.

The remaining micrographs undergo the second pre-processing step called **CTF ESTIMATION**. The micrographs are transferred into Fourier space where the CTF parameters can be determined by fitting the Thon rings of the Fast Fourier Transform (FFT). For estimating the CTF CTFFIND4 [90], Gctf [91] or Cter (SPHIRE) were used.

In the **PARTICLE EXTRACTION** step, automated particle picking was performed using the software crYOLO [88, 89] or Gautomatch [92]. These software tools use template matching algorithms for particle identification. Additionally, crYOLO uses a convolutional neural network approach. The crYOLO installation provides three different general models, which contain a set of commonly used particles. In case the general models do not give satisfactory results, the user can train a specific model using their own dataset. For the pipeline described here, the general model for cryo images (low-pass filtered) was used for particle picking in crYOLO. A template was generated for Gautomatch using the own data as an input for the algorithm. Selected particles were extracted with a particular box size (fig. 3.13) and images were saved as stacks. The output of this particle extraction step is a text file containing coordinates of the individual particles in each micrograph.

Until to here, a collection of software tools were used. They were selected on the basis of success. Various tools were tested and the tool with the highest success rate was then selected for the workflow. All remaining steps of the workflow were carried out in RELION.

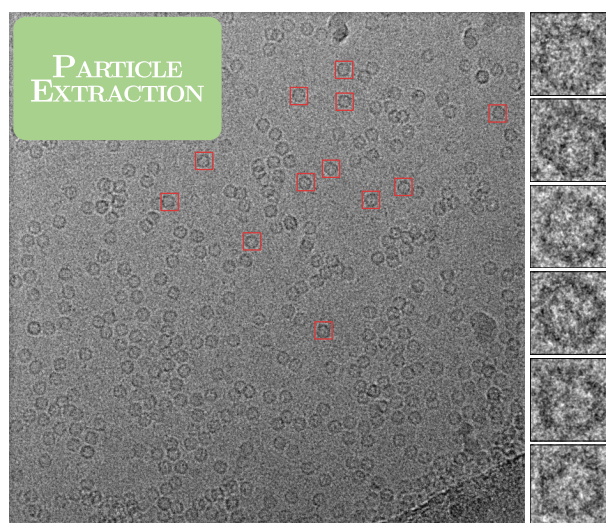


Figure 3.13: Particles were picked automatically in all micrographs. Particles were extracted using a particular box size and particle coordinates were saved in a text file.

Initial Analysis

From here on, the reconstruction is carried on the extracted particle images instead of micrographs. Therefore, the individual particles are boxed out with a desired box size from the acquired micrograph based on the output coordinate files created in the particle extraction step (fig. 3.13).

After the extraction of particles, it is important to perform a **2D CLASSIFICATION**. RELION includes a reference-free 2D class averaging. In this step several 2D orientation parameters (x -, y -shift and in-plane rotation) have to be determined to align particles of similar view and group them together into homogeneous subsets. These subsets are averaged to 2D class averages, which enhances the SNR. Besides an improved SNR, the 2D classification step is useful to select suitable particles for high-resolution structure determination. Running 2D classification cleans the dataset from contaminants and aggregated or denatured particles.

Good 2D class averages show strong white density of the protein and a black featureless background and are selected for further processing (fig. 3.14). This step can be repeated several times to further exclude bad particles [96, 97, 98].

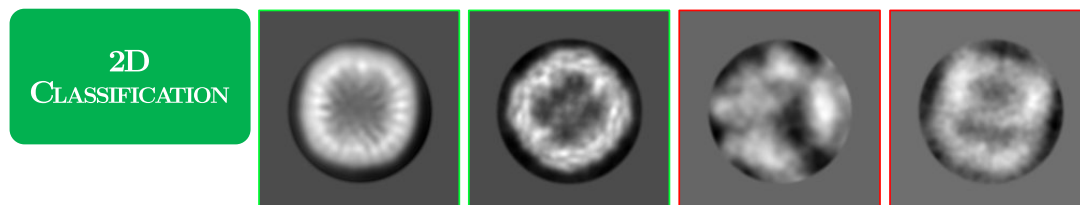


Figure 3.14: 2D class averages from an apoferritin dataset. The two class averages on the left marked in green show good class averages. These class averages are well aligned, show white protein density on a black featureless background and are selected for further processing. However the two images on the right marked in red, show bad class averages, which will be discarded.

From the good 2D class averages, a 3D **INITIAL MODEL** can be calculated, which is required for the following iterative refinement steps (3D classification and 3D refinement). RELION uses a SGD¹⁵ algorithm [99] to generate a *de novo* 3D initial model from 2D particles of the same dataset (fig. 3.15). SGD uses a different small random initialization at each iteration step, starting with a set of raw images and an initial symmetry of the 3D structure of the protein. During each iteration the 3D model is refined and updated against the raw data. Alternatively, a downsampled structure of external data (e.g. X-ray structure, negative stained data) can be used. This is in case the data do not provide enough viewing directions or detailed class averages in 2D classification.

¹⁵Stochastic Gradient Descent

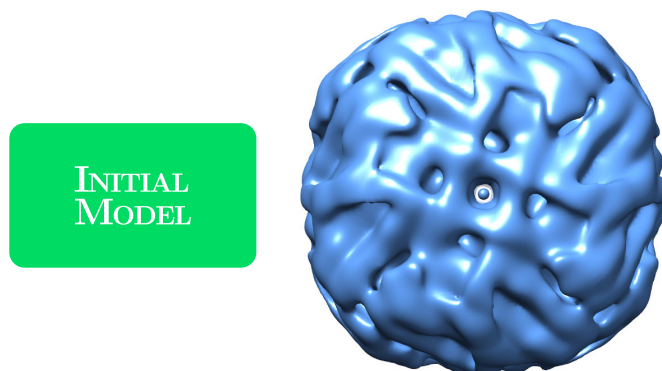


Figure 3.15: Low resolution initial model of an apoferritin dataset.

Iterative Refinement

Proceeding the workflow, the next step is the iterative refinement of the data to gain a high-resolution structure of the protein.

The first optional procedure is a second classification step, **3D classification**. Here, the projections from the previously generated 3D initial model are computed for a complete set of angles. These computer generated projections are compared with each experimental particle image, which provides the required information about the relative orientation. The extensive angular search is performed to later group the particles into 3D class averages based on their similarity.

Figure 3.16 (A) shows the output of a 3D classification of an apoferritin reconstruction. Only the green 3D class average on the left was selected for further processing. The other two 3D classes did not provide particles of sufficient quality for high-resolution reconstruction and were not kept in the particle subset. This step is used to further identify and delete bad particle images and therefore improve the quality of the remaining data [100, 101].

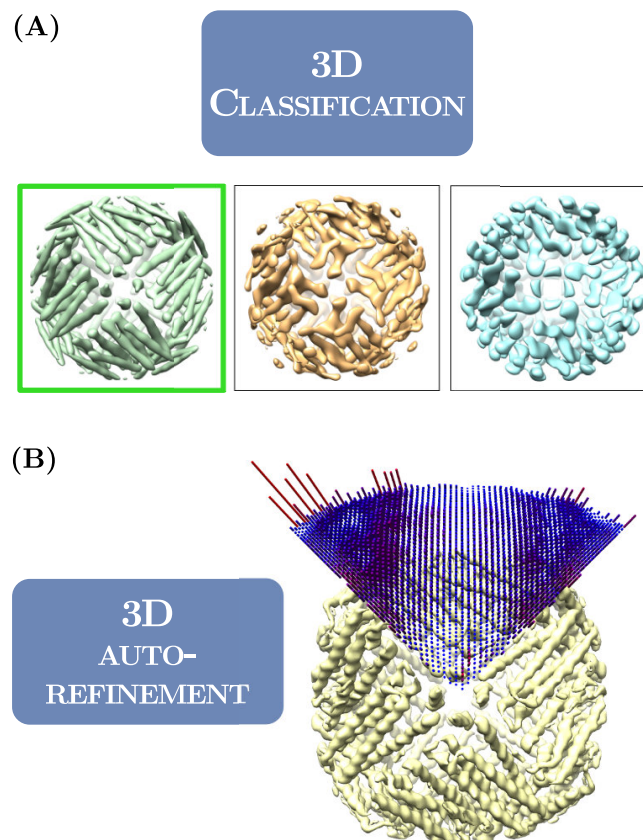


Figure 3.16: (A) 3D class averages of an apoferritin dataset. The green class on the left was chosen for further high-resolution reconstruction. The other classes were not contributing to the following reconstruction steps. (B) 3D model generated from the 3D auto-refinement step in RELION. Length and color of each cylinder shown in this image correspond to a number of particles at a specific Euler angle.

Once the data have reached sufficient homogeneity, one can proceed with the next iterative refinement step, **3D auto-refine**. For this fully automated refinement step, the particles of the good 3D class average and the initial model is requested. The dataset is equally divided into two parts to run two independent refinement reconstructions. A gold-standard Fourier Shell Correlation (FSC) curve is calculated to quantify the quality and estimate the resolution of the analysis. Thereby, self-enhancing overfitting may be avoided. The FSC is computed by estimating the local resolution between equivalent local regions of maps computed from half

maps [102]. The refinement repeats iteratively until it converges [85].

The result of this step is a refined 3D structure (fig. 3.16 (B)). The cylinders shown in figure 3.16 (B) correspond to the number of particles at a specific Euler angle, which gives information about the distribution of particle viewing directions. Here, the particle viewing directions are well distributed.

Post-Processing

During **POST-PROCESSING**, the 3D model of the protein is further sharpened to improve and estimate the final resolution of the 3D protein structure. Therefore, a mask is generated from the high-resolution model to define where the solvent region starts and the protein ends. The mask is made in an additional mask-creation step integrated in the RELION software. For sufficient noise reduction in the data, the mask needs to be tight. However, at the same time, it must be sufficiently wide, as to not cut off any protein density [103].

The gold-standard FSC curves calculated in the previous 3D auto-refine step were calculated including noise. The noise present in that step leads to underestimated resolution. During post-processing, noise that lowers the FSC curves is filtered to achieve a higher resolution.

Figure 3.17 shows the post-processing output. The sharpened high-resolution 3D structure of apoferritin at 3.4 Å resolution (A) and the gold-standard FSC curves of an apoferritin dataset are presented here.

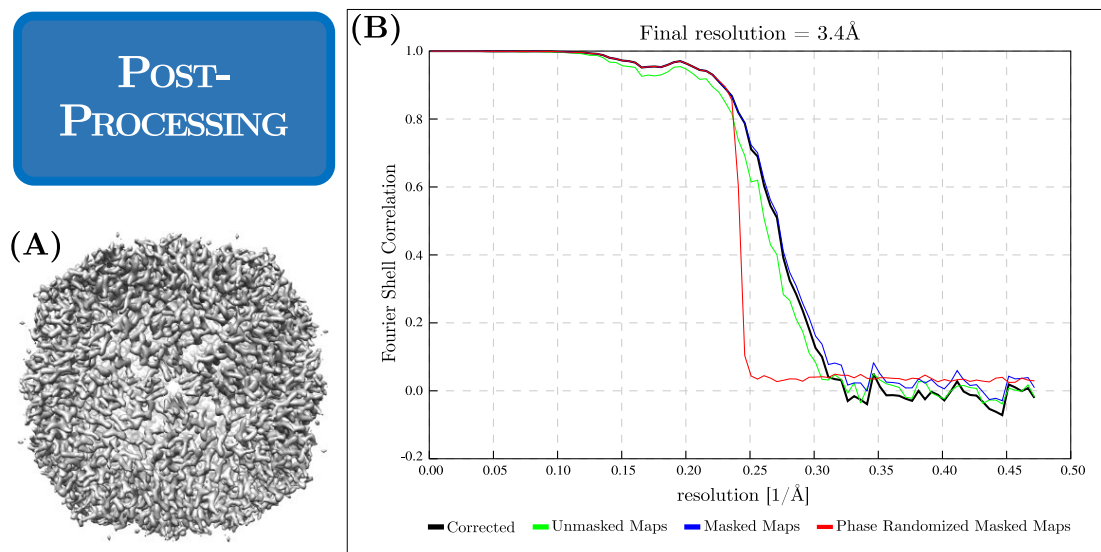


Figure 3.17: (A) 3D map of apoferritin at 3.4 Å resolution after post-processing. (B) Gold-standard FSC curve calculated during the post-processing step. The FSC is computed by estimating the local resolution between equivalent local regions of maps computed from half maps. The estimated local resolution is that of the Fourier shell where the black corrected FSC drops below the threshold of 0.143, which in this example leads to a resolution of 3.4 Å. To exclude under-estimation of the resolution the red curve (Phase Randomized Masked Maps) needs to be close to zero at the resolution estimate of each maps (Corrected, Unmasked Maps, Masked Maps).

Chapter 4

Development of a Metal-Film Zernike Phase Plate

At the time KonTEM was developing the phase-plate system, the engineers focused on the development of the PP hardware and software to control the PP inside the microscope. Except for a basic analysis, systematic experiments on the PP itself, e.g. PP material, film thickness, PP hole diameter or methods to prevent the PP from ageing were not performed. To get a better understanding of the PP, a series of experiments dealing with properties and behavior of a metal film-based PP were performed. These experiments are described in this chapter.

While the first part of this chapter deals with the fabrication of the PP, the second part describes experiments investigating the behavior of the PP inside the TEM. The chapter starts with the installation of the PP inside the Titan Krios at caesar, followed by experiments characterizing the PP while using it. The final part of the chapter introduces the PP *rocking*-mode, an operation mode to minimize imaging artifacts caused by the PP.

4.1 Phase Plate Fabrication

The two major characteristics of a Zernike-based PP are the PP film and the PP hole. Choice of material, thickness and structure of the PP film have a significant impact on the PP performance [33, 17, 16]. The effect of the PP hole is of equal importance. The diameter of the PP hole is directly connected to the lowest resolution that is affected by the PP (cut-on frequency) [104]. PP holes have to be very small, typically 0.5 μm to 4 μm in diameter. A Focused Ion Beam microscope provides the nanometer precision needed to cut holes of such a small size. Even the cutting technique has to be considered as it influences the PP hole edge, which needs to be smooth. Considering all essential details mentioned above, several steps were needed to establish a reliable fabrication process. The following chapters describe the strategies and processes to fabricate the PPs used in this thesis. A list of all fabricated and installed PPs can be found in appendix B.1

4.1.1 Preliminary Experiments

The fabrication of the PP hole is a crucial step for the function of the PP. Therefore, the milling process of the PP hole is further investigated in this chapter.

For PP hole milling a Zeiss Crossbeam XB1540 (*Carl Zeiss AG*) (chapter 3.1) workstation in ion-beam lithography setup was used. Here, the beam is controlled by an external scan system (Raith Elphy Plus, Raith GmbH) that can process graphical patterning files. These files control the beam path and the applied dose. Figure 4.1 (A) shows the FIB beam path for the PP cutting process. The arrows indicate the individual beam patterns and the directions of the ion beam. Circles were cut starting with the smallest radius in the middle and increasing it step by step towards the outside. This cutting strategy led to a sharp PP hole edge, which is essential for the PP performance.

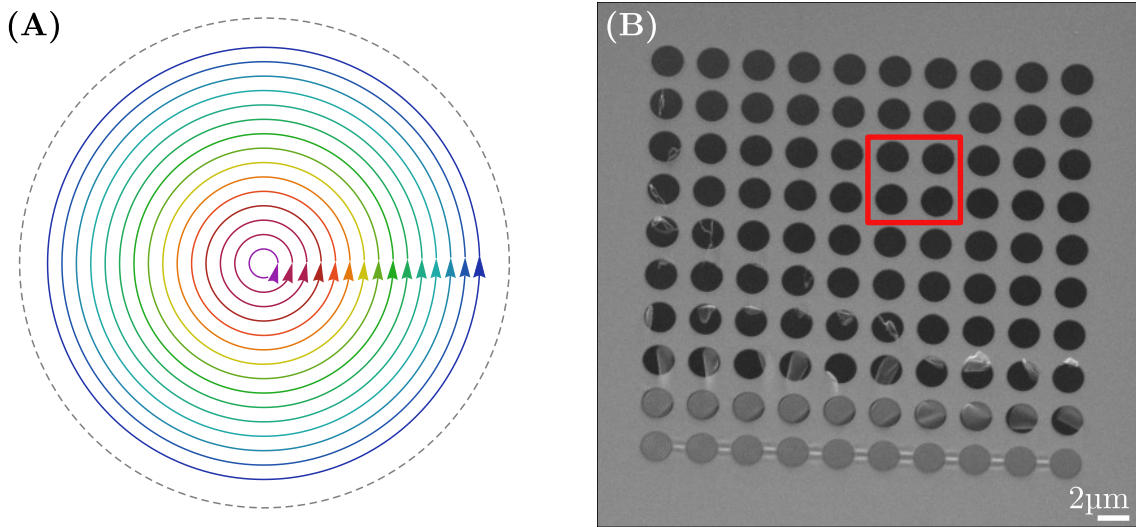


Figure 4.1: (A) FIB beam path for the PP hole cutting process. The arrows indicate the individual beam path and its direction. Circles were cut beginning with the smallest radius in the middle, increasing it with each step. (B) SEM image of a dose test. Along the x-axis the number of rings was increased while the dose was enhanced along the y-axis. Settings in the red-marked area were used for the experiments herein.

In a second step, optimal FIB settings were determined performing a dose test. Using a correct dose is important, because an insufficient dose will lead to incomplete milling (fig. 4.1 (B)) while a too high dose may lead to damages in the hole edge.

Therefore, a pattern of 10x10 holes, of the favored hole diameter, was programmed. The number of lines was increased along the x-axis while the dose was enhanced along the y-axis. This test was performed for multiple hole diameters used in this work (1 – 3 μm). Figure 4.1 (B) shows a SEM image of the dose test performed for the hole diameter of 2 μm . For a low dose and a low number of rings, the dose was not sufficient to cut a hole. In the case of insufficient dose, fragments of the cut carbon film can be seen around the hole edge. The upper right corner shows holes of sufficient accuracy without any remaining carbon film around the hole edge. As by increasing the dose and number of rings, cutting times rise too. Therefore, settings in the marked area of figure 4.1 (B) were selected to have a sufficient dose and a reasonable milling time.

The used FIB settings depending on the hole diameter are listed in table 4.1.

Table 4.1: FIB settings for hole diameters determined by dose test.

Phase Plate Hole Diameter	1 μm	2 μm	3 μm
Beam current [pA]	50	50	50
Dose 50000 [pAs/cm]	0.5x	0.8x	0.8x
Diameter [μm]	0.8	1.8	2.8
Total number of rings	5	10	15

4.1.2 Phase Plate Fabrication Workflow

Zernike-based PPs require a homogeneous, flat and thin PP film as well as a small, sharp PP hole. The fabrication of previous PPs, of this kind, required costly equipment and careful work [32]. Here, a reliable fabrication process for Zernike based PPs in only three steps using ion-beam lithography, sputter coating and plasma etching, was established. For a start, a base layer was needed, which had to be stable, smooth and easy to remove without leaving any residue. Copper or gold grids with an amorphous continuous carbon film (*Quantifoil* Cu/Au continuous C 200 mesh) turned out to be the best choice. These grids can be purchased with a constantly good quality of an amorphous and flat carbon film, which can be removed by plasma etching. In this work, two different processes were used to fabricate PPs of Zernike configuration, which will be presented in the following sections in further detail.

Workflow I

The first fabrication process carried out in this work is shown in figure 4.2. As a starting point, standard gold or copper TEM grids were used as substrate for the PPs. These grids are coated with an amorphous continuous carbon layer (*Quantifoil* Cu/Au 200 mesh grid).

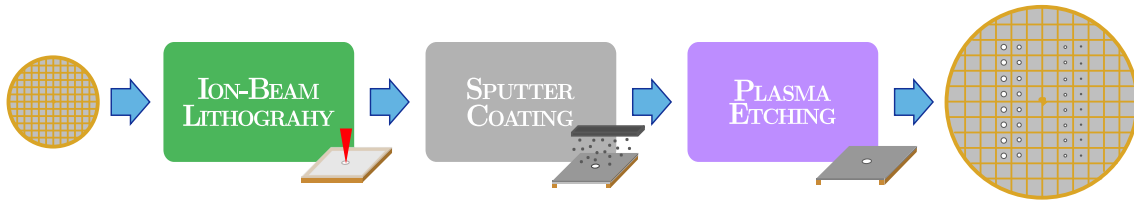


Figure 4.2: PP fabrication workflow I. In the first step a continuous carbon film TEM grid was transferred into the Zeiss Crossbeam workstation. By ion beam lithography, PP holes were milled into the carbon film. In a second step, a thin metal layer was sputtered on top of the carbon layer. Afterwards the carbon support layer was removed by plasma etching.

The first step in the PP creation process is the cutting of the PP hole. Therefore, a hole of a few micrometers in diameter was cut into the carbon film using ion-beam lithography. In this work, a Zeiss Crossbeam XB1540 workstation (*Carl Zeiss AG*) with a Raith Elphy Plus system (*Raith GmbH*) was used for ion-beam lithography (chapter 3.1). PP holes were cut in circles of increasing diameters up to the favored hole size (chapter 4.1.1). PP holes were cut into the middle of a grid mesh (fig. 4.3 (B),(C)). Positioning of the holes was performed without visual inspection to minimize the applied electron dose. Electron imaging on the carbon support film inside the FIB turned out to lead to a film contamination, which can be seen in the metal film of the PP shown in figure 4.4 indicated by the red arrows. The PP hole edge is indicated by a blue arrow in the top of the image.

The PP grid held PPs with multiple hole sizes, which were required for the experiments in this work.

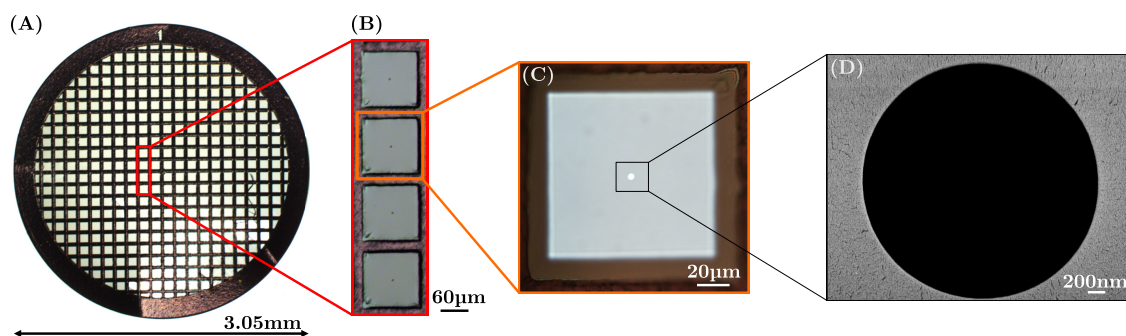


Figure 4.3: (A) Light microscopy image of a gold-palladium PP grid. (B) Magnified AuPd PP grid showing four meshes, each mesh contains a PP hole of $2\ \mu\text{m}$. (C) Magnified AuPd PP grid shows one mesh with a PP hole of $2\ \mu\text{m}$. (D) SEM image of the PP hole.

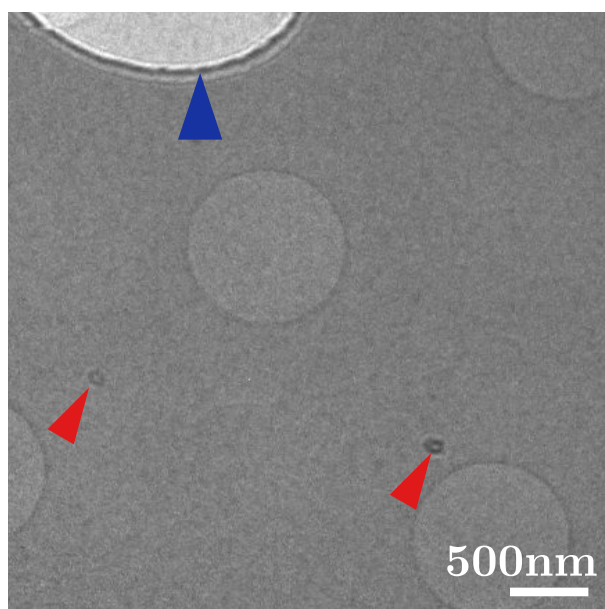


Figure 4.4: TEM image of an iridium PP. The image shows contaminations in the iridium PP film indicated by red arrows. The blue arrow in the upper left of the image points at the PP hole edge. Pattern of darker holes present the sample and not the PP.

In the second fabrication step, the carbon film of the PP grid was coated with the actual thin metal film that later forms the PP. This film, with a thickness of a few nanometers, was applied by magnetron sputtering. Therefore, the ion

milled TEM grids were placed on a glass slide (carbon film facing up) inside the reaction chamber of a MED 020 sputter coater (*BAL-TEC*) (chapter 3.1). The object slides were further used for remeasuring the layer thickness using atomic force microscopy (chapter 4.1.3). The settings used for sputter coating are listed in table 4.2.

Table 4.2: MED 020 settings for sputtering process of the two metals used for PP films in this work.

	Gold	Palladium	Iridium
Current [mA]	55	55	55
Pressure [mbar]	1×10^{-2}	1×10^{-2}	1×10^{-2}
Working Distance [cm]	8	8	8
Density [g/cm³]	17.85	22.42	22.42
Mean Inner Potential [V]	32.18	37.24	37.24
Layer Thickness [nm]	12	6.5	6.5

The carbon support film of the PPs was removed by plasma etching shortly before the installation of the PP inside the TEM. The carbon was plasma etched in an 80:20 argon-oxygen plasma at 2.6 μ bar for 7 min using a Model 1020 plasma cleaner (*Fischione Instruments*). Afterwards, the PP was immediately installed in the Titan Krios.

PP grids were stored after the ion-beam lithography step in a desiccator. Preparation steps two and three (magnetron sputter coating and plasma etching) were always prepared immediately before insertion into the Titan Krios TEM. In case the PP had to be stored after coating or plasma etching, the PPs were always kept under vacuum conditions.

Quality assessment of the PP was done by scanning-electron microscopy. Figure 4.3(D) shows an SEM image of a gold-palladium PP. The PP hole shows a sharp circular hole edge without any damages. Therefore, PP fabrication process I can be considered as a good PP production workflow.

Workflow II

An open question in the fabrication of the PPs was the order of the process steps. Is the order 1-2-3 (fabrication process I) leading to the best possible PP hole or does an alternative order of steps 2-1-3 (fabrication process II) produce even smoother hole edges? In a second series of experiments this alternative workflow was tested (fig. 4.5). The single steps were identical to fabrication process I with the exception of the order of the changed steps.

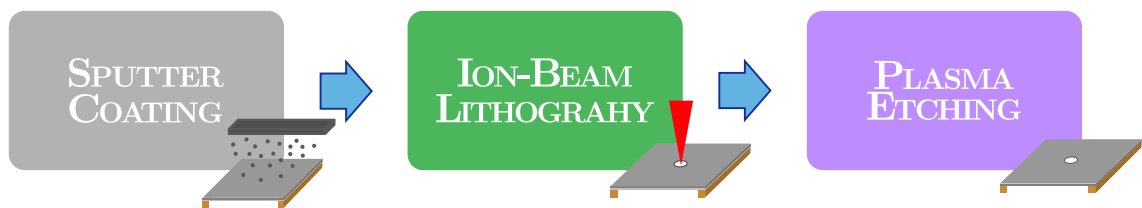


Figure 4.5: Second fabrication workflow starting with sputter coating of the TEM grid. Followed by ion-beam lithography cutting the hole into the PP and removing the carbon support film by plasma cleaning in the last step.

Figure 4.6 shows an example of such a PP hole produced via fabrication process II. It can be seen that the film structure, as well as the hole edge, was damaged during the fabrication process. The hole edge shows a lift of the metal film around the PP hole. The PP hole edge is not sharp and shows lots of cracks, which are also present in the metal film. This makes the PP unusable for PP experiments as the distribution of an equal phase shift requires a sharp and fine-grain PP film.

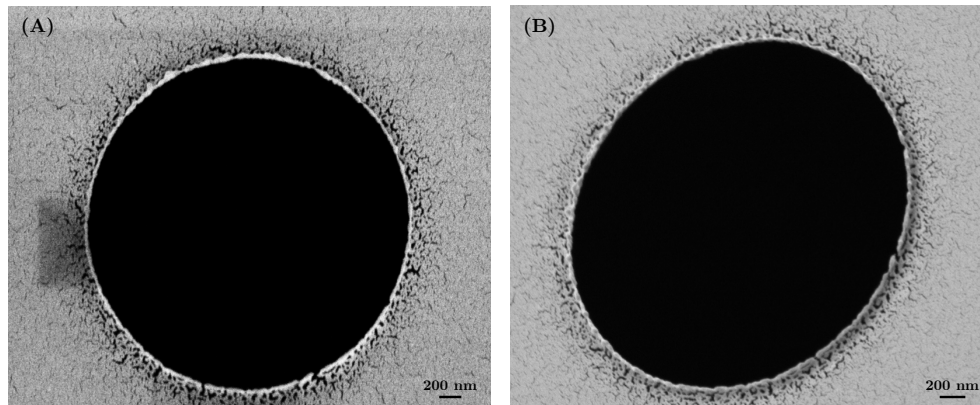


Figure 4.6: Two SEM images of the same PP hole with a hole diameter of $2\ \mu\text{m}$. (A) shows the PP hole from 90° top-view, while (B) shows the same sample tilted by 30° . Both images show a PP hole edge, which bends upwards and strong crack structures around the edge can be seen. The dark square on the left side of the hole edge in fig. (A) comes from the imaging the sample with the SEM.

4.1.3 Thickness Measurement of Phase Plate Films by Atomic Force Microscopy

During MED 020 (*BAL-TEC*) sputter coating process, PP film thickness was measured by an integrated quartz sensor QSG 100 (*BAL-TEC*) (chapter 3.1). To confirm the accuracy of the quartz sensor, the sputtered layer thicknesses were measured by AFM (JPK NanoWizard3, *JPK Instruments AG*) (chapter 3.1).

For sputtering of gold-palladium (AuPd) TEM grids were placed on a cleaned glass slide (carbon film facing up). The object glass slide was sputtered in the same way and could be used for remeasuring the layer thickness by atomic force microscopy. For the AFM measurement, part of the gold-palladium layer was removed from the object slide by scratching with a razor blade to create a sharp edge required for the measurement. Afterwards, the scratches in the gold-palladium layer were measured.

During the application of the PPs (chapter 4.2.2), gold-palladium turned out not to be the best possible material for PPs. Iridium was found as a better material choice. For measuring the iridium layer thickness, the measuring procedure had to be adapted. Iridium is a very hard metal and cannot be removed easily from the glass surface by scratching. Therefore, PMMA¹ coated glass slides (*Uni Bonn, AG Linden*) were used for iridium film deposition. PMMA can be removed by washing in organic solvents. For measuring the iridium layer thickness, the PMMA was partly removed by scratching a pattern into the PMMA coated object slide. TEM grids were placed on the PMMA coated object plate (carbon film facing up) for sputtering. After sputter coating the PMMA layer was removed by several washing steps using acetone, isopropanol, ethanol and double-distilled water.

The result is a glass slide with a thin line of iridium. The height profile is then measured between the glass surface and the iridium line. Figure 4.7 shows an image of such a prepared slide inside the AFM. The image shows iridium as a dark horizontal line. In the left part of the image the AFM cantilever can be seen as a dark triangle. The purple reflections are from the laser that is focused on the tip for measuring the movement of the cantilever.

¹Poly(methyl methacrylate)

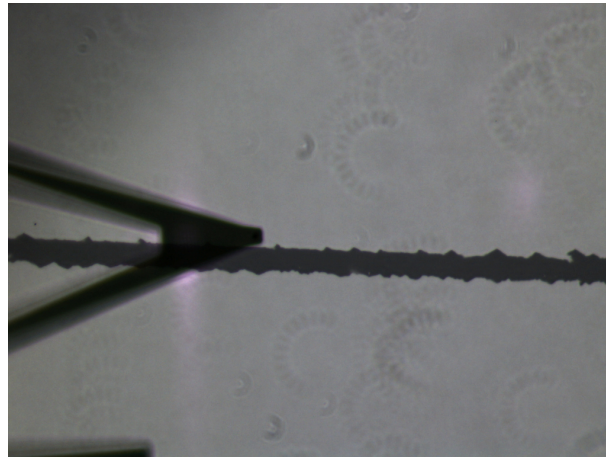


Figure 4.7: Light microscopy image showing the iridium line on a glass object slide measured by the AFM cantilever tip. The triangle on the left side represents the AFM cantilever. The horizontal line is the iridium layer.

The layer thickness was measured in contact mode. Contact mode is recommended for hard materials, leading to a high resolution, which was required for the thin metal layers of just a few atoms.

For the measurement, the cantilever tip was positioned in direct vicinity to the iridium line. To detect the motion of the tip, the laser was focused onto the end of the cantilever. The reflected beam was centered onto the four-segment photodiode, and afterwards the measurement was started.

In a typical experiment, 10 lines were measured and averaged across the iridium edge. Figure 4.8 shows two examples for the resulting height profiles. The curves show measurements for the PPs IrNo4 and IrNo 5-7. The graphs show the average of 10 line scans. For calculation of the layer thickness, the mean value of the glass slide was subtracted from the mean of the iridium layer. The graphs show that the homogeneity of the iridium layer is very good. This is promising for the later use of this material for PPs.

The results of further measurements performed in this work can be found in appendix B.2.

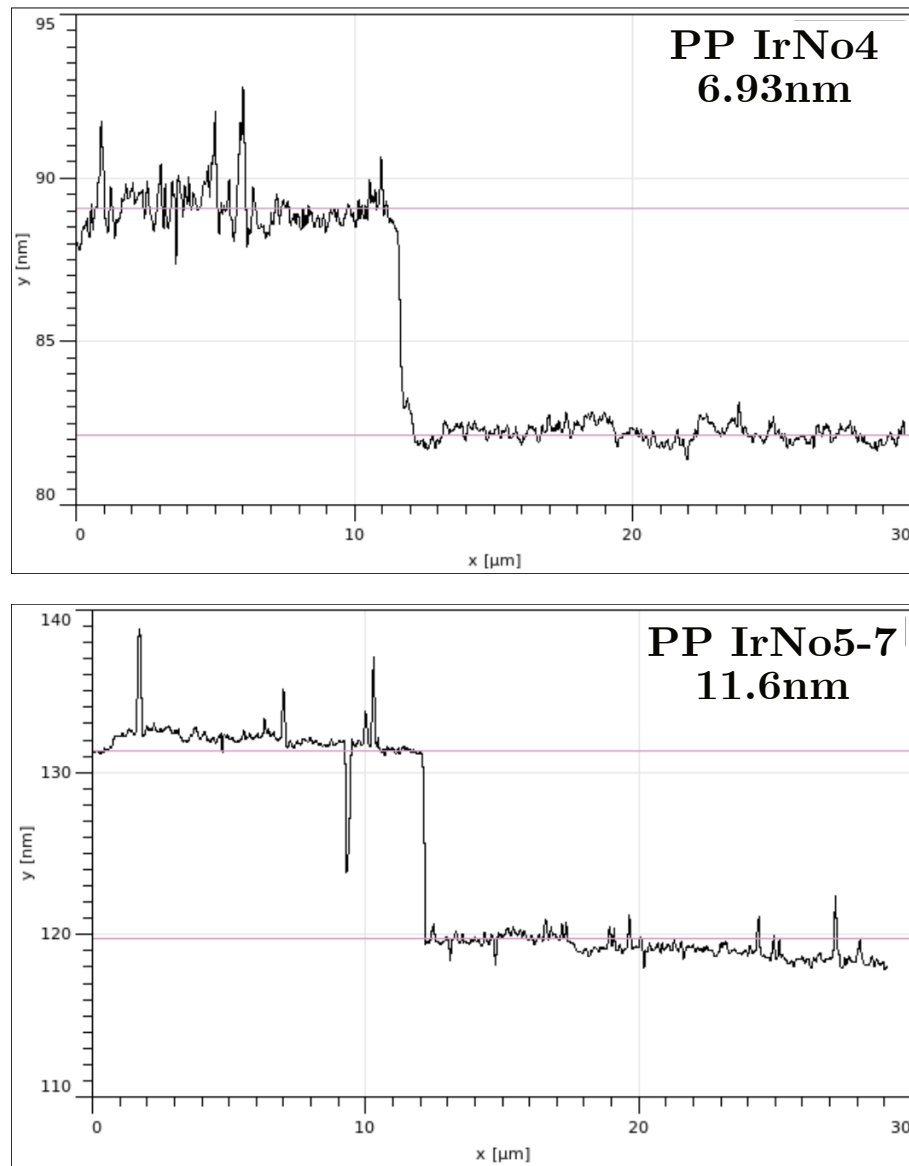


Figure 4.8: Plots of AFM measurements of iridium PPs No4 and No5-7. The graphs show the average of 10 line scans. Layer thickness is calculated by subtracting the mean value of the glass slide from the mean of the iridium layer.

4.2 Phase Plate Characterization

The majority of the previously described Zernike-PPs used amorphous carbon as a PP film [38, 33]. These PPs usually suffered from limited stability and other accompanying obstacles. Several alternative materials for thin-film PPs have been investigated over the past decades but no material, other than carbon, took hold [105]. In this work a Zernike based PP using a thin metal film is described.

Ageing and charging are two known problems of thin-film PPs, which reduce their lifetime. Here, two methods were implemented to reduce ageing and charging effects of the metal-based PP, which will be described later in this section.

The PP hole diameter has a direct effect on the performance of the PP. Therefore, different hole diameters were tested and the results are presented in section 4.2.4. Kurth et al. firstly introduced the *rocking*-technique as a method to reduce charging of Zernike-PPs [74]. In this work, the idea of a *rocking*-PP is taken up to overcome multiple obstacles of Zernike-PPs at the same time.

Furthermore, lifetime and the need to replace the PP in regular intervals is an ongoing topic. Therefore, hardware changes were made to improve and facilitate the installation and exchange of PP grids into the Titan Krios TEM.

A more detailed description of these hardware improvements will follow in the coming section.

4.2.1 Phase Plate Installation

The KonTEM PP system installed in the TEM at caesar is the first PP system installed in a Titan Krios TEM [70]. In the beginning of this work, the system was in a prototype state and not prepared for an every day PP exchange. Especially during the PP development experiments, a frequent exchange of the PP was inevitable. The necessary modification to empower the system for my experiments will be described later in this section.

First, a brief description of the exchange procedure will be given.

For a PP exchange, the microscope column needs to be vented first. After the TEM column reached ambient pressure, the PP holder had to be extracted.

Maximum care had to be taken during this step to avoid damage of the PP. It has to be mentioned that the available space inside the TEM is in the range of approximately 100 μm . After the extraction, the microscope column was sealed and set under vacuum to prevent contamination of the TEM column. This accelerates evacuation time after reinstalling the PP and greatly reduces the time until the microscope is ready to use. The extracted PP holder was transported to the lab to exchange the PP grid. The PP was installed into the PP tip, followed by plasma etching the PP to remove the carbon support film (section 4.1.2). The PP was transferred to the microscope and immediately reinstalled to minimize contaminations.

At the start of the project, the PP holder and the control unit were hardwired. The cable connecting the two units of the system could not be detached. This made the transport of the PP system very difficult. Two people were needed to move the system out of the TEM room. Alternatively, all operations had to be done in the limited space at the microscope. In this case, plasma etching of the PP was not possible at the TEM. Even when transporting the complete PP system to the lab and running the plasma etching of the PP there, the time between plasma etching and reinstallation took so long that contamination of the PP film was inevitable. Therefore, hardware changes of the PP system were necessary to improve, simplify and speed up the PP grid exchange process.

The following modifications were made to the system to improve its usability. The first step in speeding up the exchange process was a change of the wiring between the PP holder and the control units. Therefore, the existing undetachable wiring was replaced by HDMI connections.

Standard HDMI cables, known from computer and TVs, provide highly shielded connection for high-speed digital data transfer. The multiple wires of an HDMI were found to be ideal to connect the control signal between the controller and the piezo motors of the PP system. Today, the PP holder can be detached from the control unit by unplugging only three HDMI cables.

The former control unit was integrated into the existing TEM control rack for better protection of the control devices. Due to this modification it is now possible to perform a PP exchange by only one person. Additionally, it comes along with a

substantial time saving. Before the changes, it was not possible to exchange a PP in just one day. Due to the modifications, the exchange process can be performed in less than one day.

4.2.2 Material Selection

The PP material is essential for its performance. For an equally distributed phase shift, the PP needs to consist of a smooth and uniform PP film. In previous studies, multiple materials were tested for PPs of Zernike configuration. Silicon wafer with a thin layer of chromium [106], iridium, rhodium or platinum [105] were tested as PP materials.

Here, a pure thin metal film without any additional support layer was used. For the first PPs produced in this work, gold-palladium 80:20 (*BALTIC Präparation e.K.*) was used.

Figure 4.9 shows images of a gold-palladium PP. The left image (A) shows a low magnification TEM image of one mesh of the PP grid. The PP hole can be easily seen close to the center of the square as a white spot. During the lithography process, the positioning of the holes was done without visual inspection to minimize the applied electron dose. Therefore, the holes can be slightly off centered. Electron imaging on the carbon support film inside the FIB turned out to lead to a film contamination, which could later be seen in the metal film of the PP (chapter 4.1.2). A slight offset of the hole from the center of the mesh does not influence the usability of the PP inside the TEM. Figure 4.9 (B) shows a TEM image of the PP hole. Normally, the PP hole is not visible in TEM images. Here the illumination of the TEM was changed (using condensed beam illumination instead of parallel illumination) to visualize the PP hole. The red arrows show cracks in the gold-palladium PP film. These cracks are a possible source for aberration when using the PP and must be avoided. They may come from the tendency of gold to form clusters or island type structures during sputter deposition. These clusters grow, due to a rather high surface tension of the gold films [107], which can be a possible explanation for the crack formation of such thin gold films.

For a more detailed analysis of the PP film, SEM images were taken once the PP was removed from the Titan Krios TEM. Figure 4.9 (C) shows a SEM micrograph of the gold-palladium film after being used inside the TEM. The film is not homogeneous, and shows a high granularity. It shows several islands of material and cracks inside the film (red arrows).

All of this led to the conclusion that gold-palladium is not the best material choice for metal-based thin film PPs.

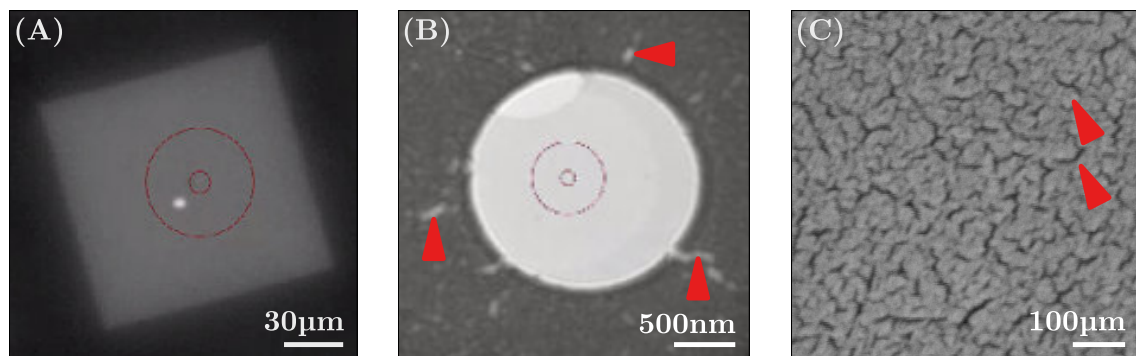


Figure 4.9: (A) TEM image of an AuPd PP (B) TEM image of an AuPd PP showing cracks around the PP hole indicated by red arrows. (C) SEM image of an AuPd PP, showing the high granularity of the PP film.

The PP film needs to be smooth and uniform to distribute the phase shift equally over the PP. Therefore, metals, which form an equally distributed film during magnetron sputtering, such as chromium, were needed. Chromium forms very smooth thin films, but it is not suitable for PP films as it oxidizes very fast. The time between the fabrication of the PP and the installation into the TEM would already be sufficient to reach full oxidation of the PP film. In previous studies, chromium, titanium and aluminum have been tested as potential PP materials but they are not qualified for this purpose as oxide layers occur very fast [108].

Iridium is known as a metal with superb corrosion-resistance. Furthermore, Marko et al. showed the good resistance to charging of thin iridium films [105]. Hence, iridium was chosen as an alternative PP material. For the fabrication of the iridium PP, a 1 mm iridium sputter target 99,9% (*Goodfellow GmbH*) was used. Figure 4.10 shows two TEM images of iridium PPs.

PPs were checked by SEM after the removal from the TEM. Unfortunately, iridium PPs seem to be mechanically less stable compared to gold-palladium PPs. A used iridium PP could never be rescued intact from the TEM. They were all already damaged inside the TEM. Consequently, they could not be checked by SEM after use.

Therefore, comparisons have to be made between figure 4.10 and figure 4.9 (B). The PP hole shown in figure 4.10 (A) shows a very sharp PP hole edge. The iridium film in this image is homogeneous and shows a very fine grain. Therefore, iridium was further used as PP material.

However, very small denser spots could also be detected in the iridium film (fig. 4.10 (B)). These small clusters may occur during the sputtering process, either from contaminations on the carbon support film or due to larger grain formation of iridium. Influences of these clusters on the performance of the PP were observed if the dense spots were found close to the PP hole.

Clusters in the direct vicinity of the PP hole favor charging of the PP and disqualify PPs for high-resolution cryo applications. Since there are always multiple PPs on each grid, this was usually no problem during this project.

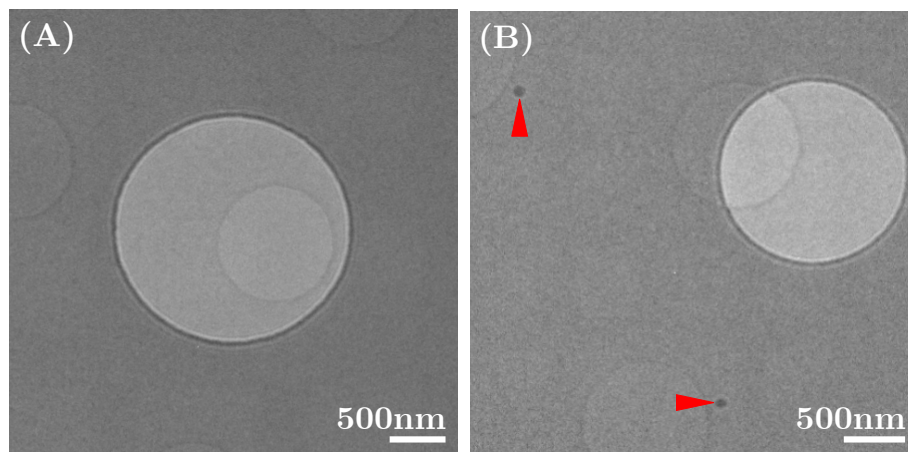


Figure 4.10: (A),(B) TEM images of iridium PPs. Both images show a homogeneous iridium film with a sharp hole edge. (B) shows darker spots in the iridium film, indicated by red arrows. The small hole pattern represents the sample.

4.2.3 Phase Plate Lifetime and Ageing Experiments

Besides material choice, ageing of the PP is another obstacle influencing the usability of a PP. Ageing, in this context, means a combination of effects that are caused by an alteration of the PP film over time. Contaminations can be present from the beginning, caused during the ion-beam lithography fabrication step (chapter 4.1.2). Nonconductive contaminations can also build up over time inside the TEM or occur in areas where the intense unscattered electron beam hits the PP. Figure 4.11 shows an iridium PP with several contamination spots caused by the unscattered electron beam (red arrows).

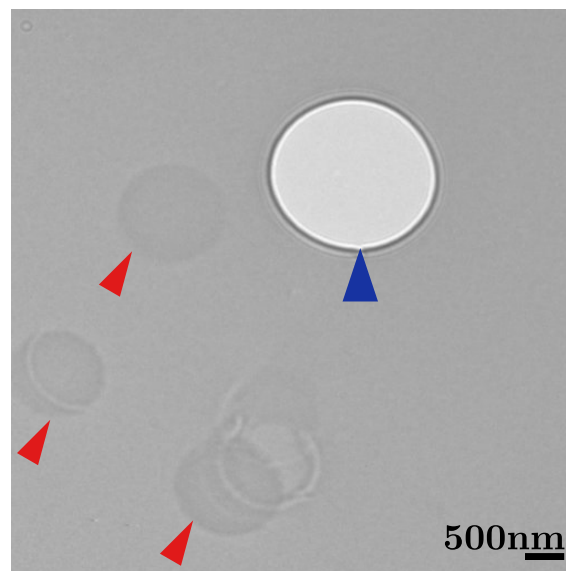


Figure 4.11: TEM image of an iridium PP. Red arrows point the contamination spots caused by the unscattered electron beam. The blue arrow indicates the PP hole.

Ageing provokes charging, which causes the PP to act like a lens, and effects the CTF [31, 32]. Figure 4.12 shows three Fourier Transforms of TEM micrographs. Here, the influence of the charging effect can be seen. The normally round Thon rings shown in Figure 4.12 (A) are severely distorted due to influence of the ageing of the PP film. This has a great effect on the CTF and leads to an incorrect phase shift.

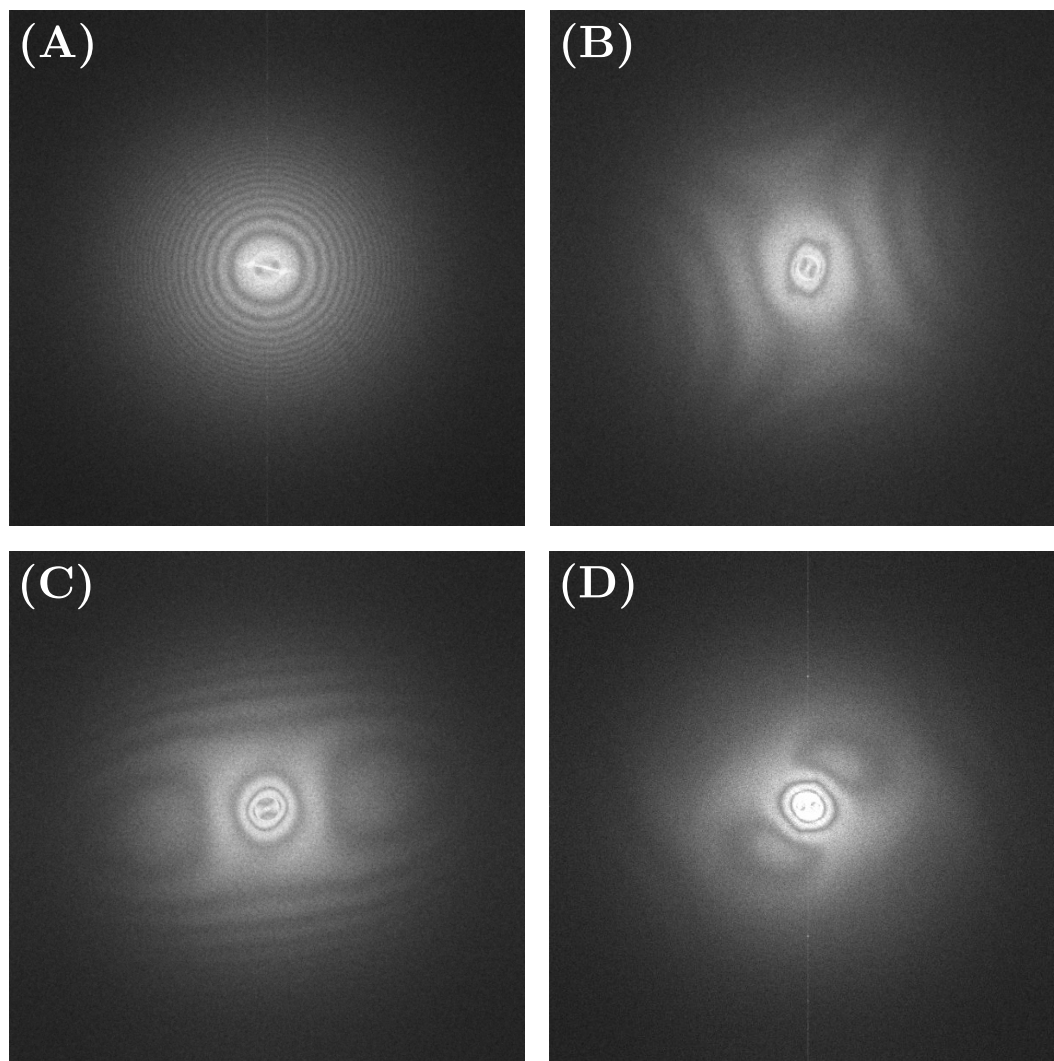


Figure 4.12: Fourier Transforms of TEM micrographs acquired with an iridium PP. (A) shows a FFT with round Thon rings, no astigmatism or charging. (B)-(D) show FFTs with distorted Thon rings caused by ageing of the PP film.

In order to prevent and reduce ageing and charging of PPs, two methods were tested.

One method to prevent adsorption and reduce contamination is heating the PP [105, 47]. The KonTEM PP system was originally designed including a heating element. This heater was reactivated. The KonTEM PP holder is equipped with a

PCT² heating element, which heats up to a temperature of 105 °C. The advantage of a PCT heater is that they are self-regulating and don't need any additional electronics. During the process of heating up the PP tip, drift occurs. Therefore, after the installation of a new PP and activation of the heating, the PP had to stabilize over night to settle for the thermal drift. The PP was heated at all times.

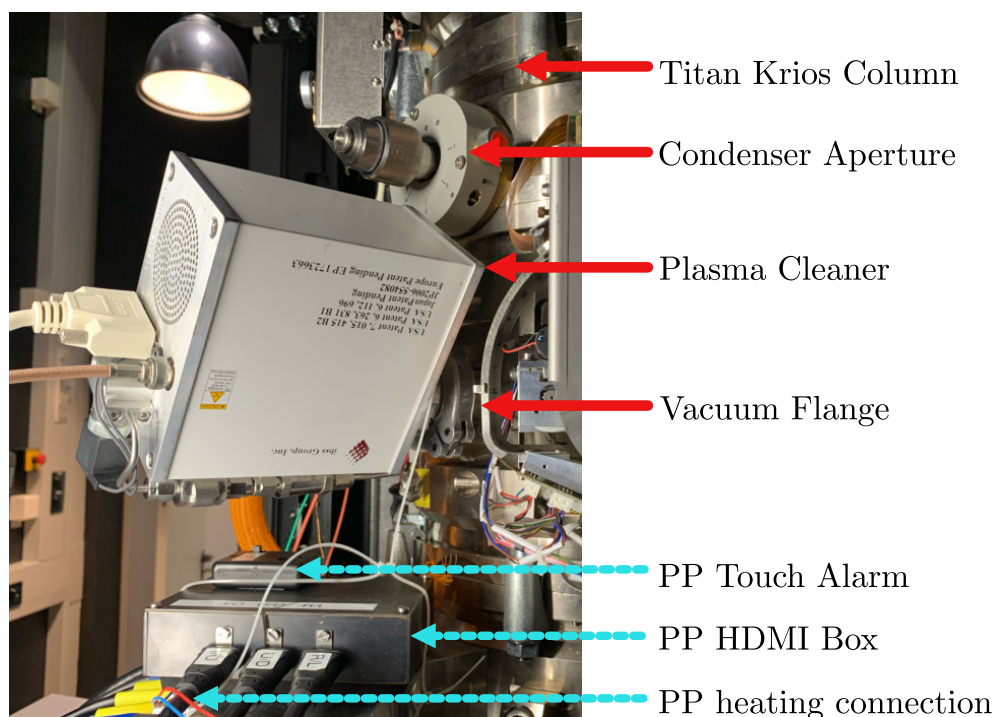


Figure 4.13: Installation of GV 10xDS Asher (*ibss Group, Inc.*) plasma cleaner at Titan Krios TEM at caesar.

Another way to remove carbon-based contamination is plasma etching in an oxygen containing plasma. Since the main source for contamination inside a TEM are hydrocarbons, plasma etching should be able to remove such contaminations effectively.

To completely rule out carbon contamination of the PP a plasma cleaner was installed directly inside the Titan Krios TEM (fig. 4.13). Therefore, a customized adapter was built to attach the plasma cleaner to the TEM column. The inside

²Positive Temperature Coefficient

of microscope column was cleaned using a GV 10xDS Asher (*ibss Group, Inc.*) plasma cleaner (30 min / 50 W / air). Contaminants were eliminated by atomic oxygen and hydrogen. The surface carbon is converted into gas phase molecules and pumped out of the microscope column. By cleaning the PP inside the microscope column, contaminations that result from the transport and installation of the PP into the TEM could be removed or at least reduced.

The plasma cleaner was also used to clean the PP after the build up of some contaminants in areas hit by the intense unscattered beam around the PP hole. The effects of a plasma cleaning cycle of 30 min can be seen in figure 4.14. Here, two images of the same PP are shown (A) before plasma cleaning, showing contaminants in the marked area and (B) showing the cleaned PP after 30 min plasma cleaning.

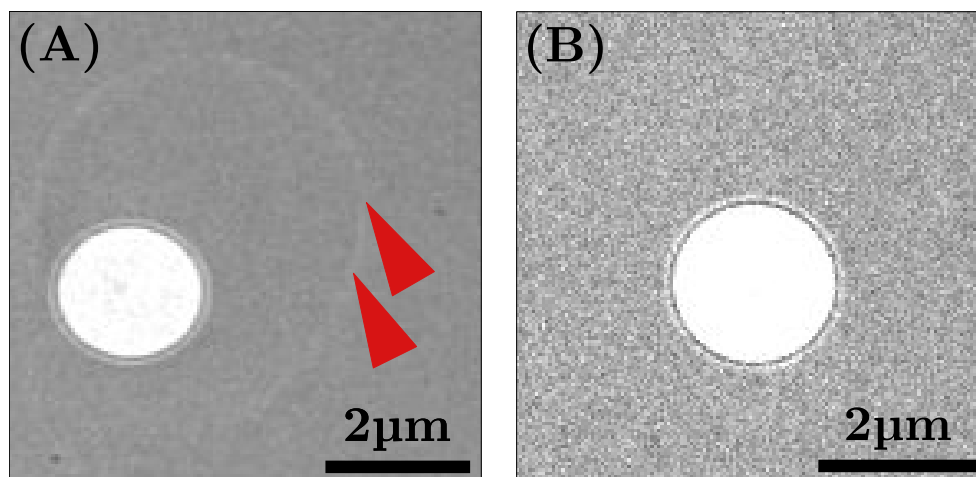


Figure 4.14: TEM images of an iridium PP. (A) PP before plasma cleaning, showing contaminants in the marked area indicated by the red arrows. (B) image of the same PP after 30 min plasma cleaning. Contaminants in the marked were removed by plasma cleaning.

4.2.4 Phase Plate Hole Size

Several experimental and theoretical studies were made to determine the optimal hole diameter of Zernike PPs [104, 109]. It is crucial, that inside the TEM, the unscattered electron beam does not get in contact with the PP film. Therefore, the PP hole must be of sufficient diameter for the central beam to pass through. The size of the central beam is related to the electron source and mainly the focal length of the objective lens of the TEM. Transmission-electron microscopes equipped with a field-emission gun have a central spot size of approximately tens of nanometers [110].

The artifact that correlates with the PP hole size is the occurrence of halos in the micrograph, which is known as fringing or ‘ringing’. Halos around high-contrast objects occur due to the sharp onset of the phase shift at the PP hole edge. On the other hand the hole diameter is directly connected to the contrast gain. Fukuda et al. showed in simulations that the ideal PP hole needs to be infinitely small to gain maximum contrast [109].

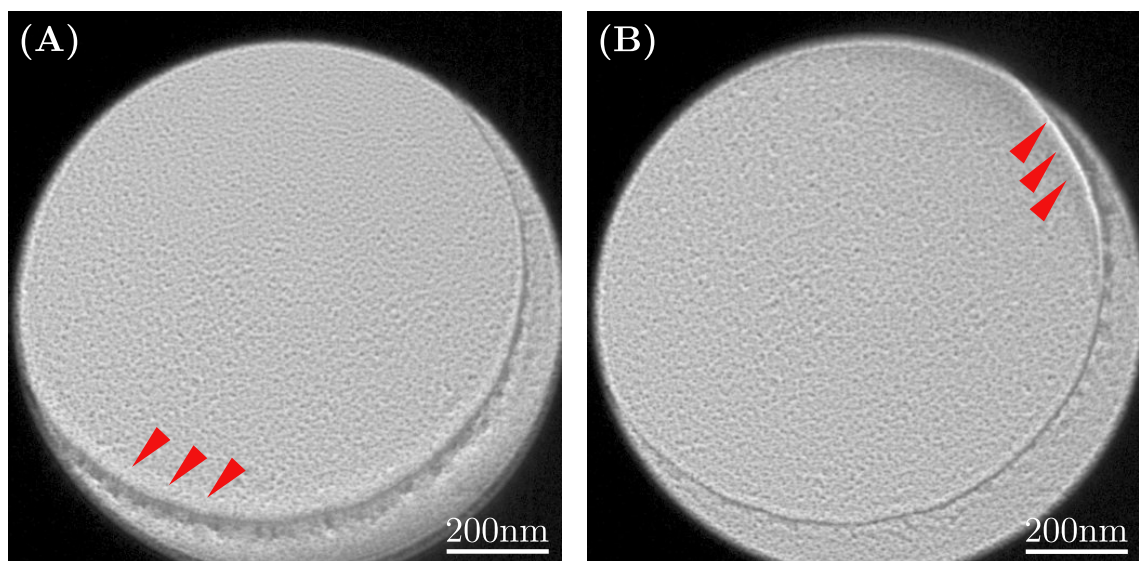


Figure 4.15: TEM images of a PP with a hole diameter of 1 μm . Artifacts caused by the hole edge of the PP are indicated by the red arrows.

In this work, PP grids were fabricated with multiple PP hole diameters between $0.5\ \mu\text{m}$ and $4\ \mu\text{m}$. Figure 4.15 shows two TEM images acquired with a $1\ \mu\text{m}$ PP hole. The red arrows point at the halos occurring at the edge of the carbon film of the sample. The technical conditions of the Titan Krios TEM at caesar did not permit centering the $1\ \mu\text{m}$ PP hole without visible fringing artifacts in the micrograph. Therefore PP holes with a diameter of $1\ \mu\text{m}$ or smaller were not used for further experiments.

In order to determine the influence of the hole diameter on the resolution, an experiment using a gold-on-carbon sample was performed. Here, micrographs of a gold-on-carbon sample (fig. 4.16(A)) using PPs with hole diameters of $2\ \mu\text{m}$, $3\ \mu\text{m}$ and $4\ \mu\text{m}$ were taken at 59,000 magnification ($1.06\ \text{\AA}/\text{pixel}$). The Fourier transform of a PP image using a $2\ \mu\text{m}$ PP hole is shown in figure 4.16(B). The yellow line in the Fourier transform indicates the gold reflexes at $2.36\ \text{\AA}$. This reflex can be seen in all images acquired using PPs with hole diameters of $2\ \mu\text{m}$, $3\ \mu\text{m}$ and $4\ \mu\text{m}$, which shows that the resolution up to $2.36\ \text{\AA}$ is not limited by the hole diameter.

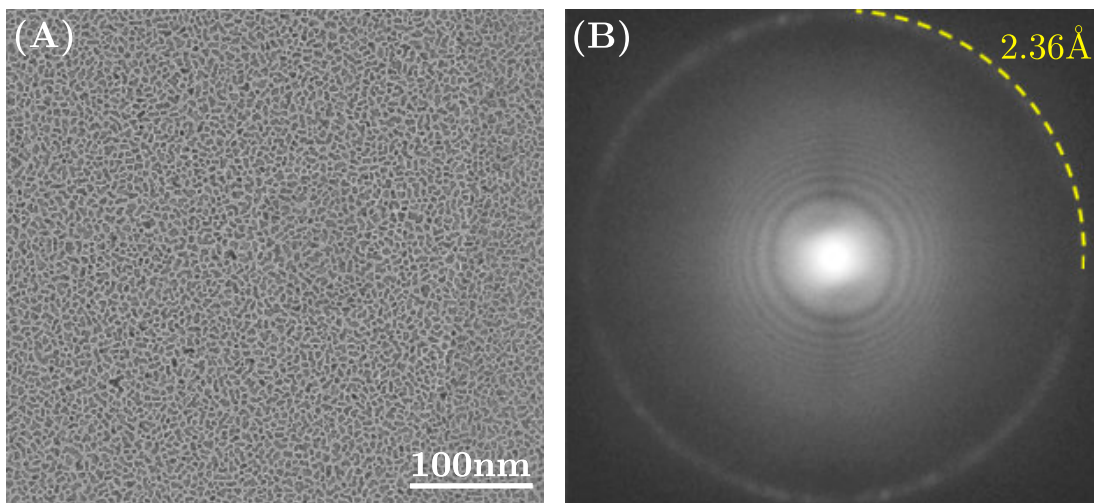


Figure 4.16: (A) TEM micrograph of gold-on-carbon acquired without a PP. (B) Fourier transform of gold-on-carbon image acquired with PPs in static mode with a hole diameter of $2\ \mu\text{m}$. Fourier transform was gamma stretched to visualize the gold reflexes on the outside and the Thon rings in the middle of the image at the same time. [111]

4.3 The *Rocking*-Phase Plate

The continuous rotation of a PP around an adjustable center of rotation is called the *rocking*-technique and was presented in 2014 by Kurth et al. [74]. KonTEM integrated the software KonSHAKER to rotate the PP using the piezo drives of the KonTEM PP positioning system (chapter 3.1). Although the *rocking*-feature was implemented by KonTEM, the *rocking*-mode was never extensively tested. Therefore, a series of experiments were performed herein to establish the *rocking*-technique.

The previous chapter addressed the fringing artifact that occurs due to the sharp cut-on of the phase shift at the PP hole edge [110]. Several attempts were made to reduce fringing artifacts by applying software filters to enhance low-frequencies [104] or by fabricating a phase-plate film with a tampered PP hole edge [112]. Here the *rocking*-technique is used, to virtually smoothen the PP hole edge by the continuous rotation of the PP. The stable circular movement of the PP during acquisition behaves like a smoother cut-on of the PP hole edge.

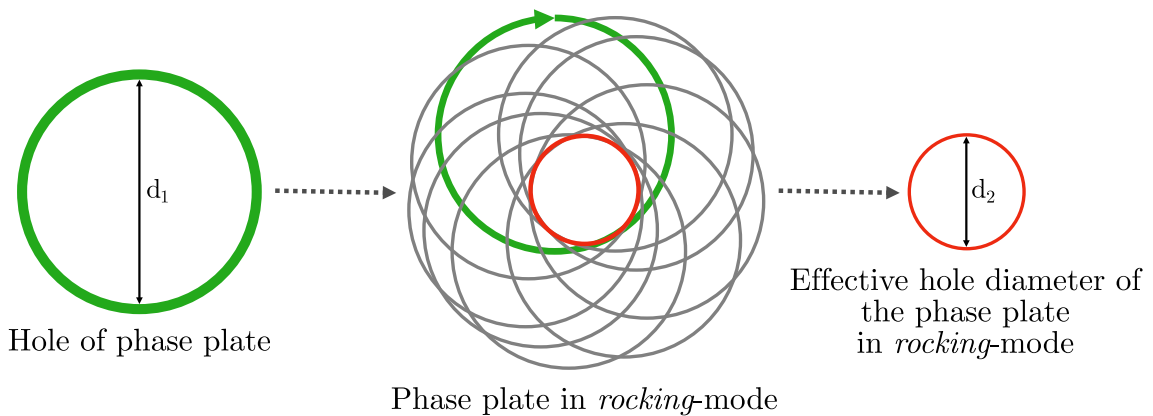


Figure 4.17: Schematic drawing of the *rocking*-PP principle. The PP hole diameter d_1 virtually decreases due to the continuous movement of the PP to an effective smaller hole diameter d_2 . Adapted from [111].

Besides the effect of smoothing the PP hole edge, the effective hole diameter of the PP changes due to the continuous movement. Figure 4.17 shows the PP hole diameter d_1 in static-mode. In *rocking*-mode the PP is continuously moved in a circular rotation around an adjustable center. Therefore, the effective hole diameter is virtually decreased to a smaller diameter d_2 . A smaller PP hole diameter reduces fringing artifacts and at the same time increases the contrast [104]. The effect of the *rocking*-mode is shown in figure 4.18. Figure 4.18 (A) shows a micrograph of a gold-on-carbon sample acquired with a PP in static-mode. The fringing artifact of the PP hole edge causes a contrast reversal in the image. Therefore, the gold clusters occur bright on a dark carbon film. Furthermore, the borders of the gold clusters are blurred, due to the fringing artifact. In comparison figure 4.18 (B) shows a micrograph of a gold-on-carbon sample acquired with a PP in *rocking*-mode. Here the sample is shown as it should be without inverse contrast. The thick and dense gold clusters appear dark on the lighter gray carbon film.

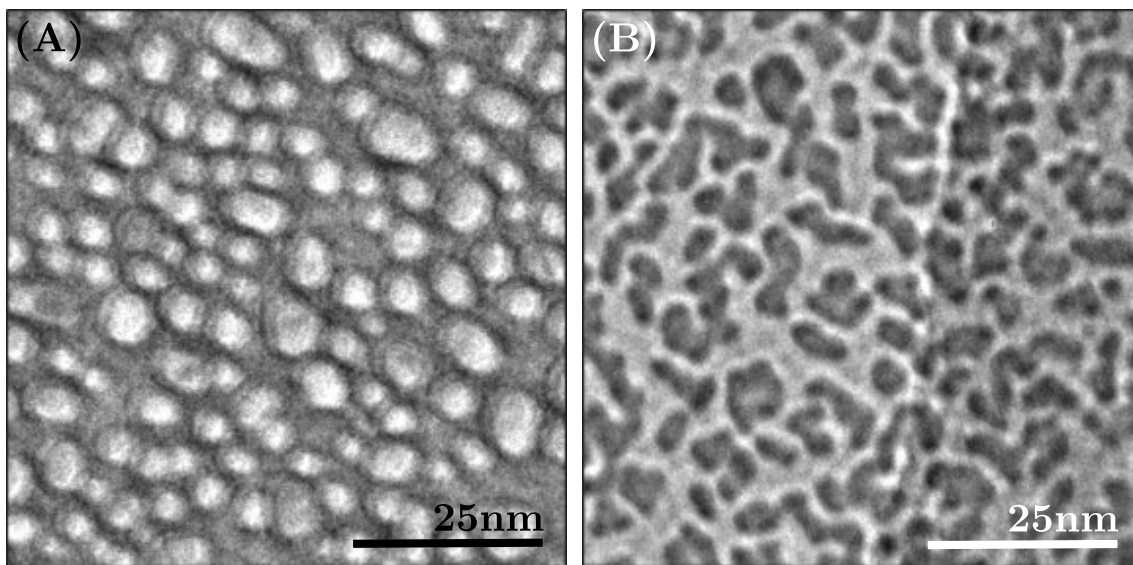


Figure 4.18: TEM micrographs of gold-on-carbon. (A) Image acquired with a $2\mu\text{m}$ PP hole in static-mode. (B) PP image using a $4\mu\text{m}$ PP hole in *rocking*-mode. [111]

In a second set of experiments, the effect of the *rocking*-mode on the CTF was investigated. Therefore, images with identical microscope settings were acquired [59,000x magnification ($1.06 \text{ \AA}/\text{pixel}$)], first in static and second in *rocking*-mode using an iridium PP with a $2 \mu\text{m}$ PP hole. Afterwards, the micrographs were transformed into Fourier space to compare the two Fourier transforms (fig. 4.19). Figure 4.19 (A) shows a Fourier transform of a micrograph acquired in static-mode. The PP is slightly off center, which can be seen in the bright middle of the Fourier transform. However, figure 4.19 (B) was acquired in *rocking*-mode. It can be observed that the PP in *rocking*-mode is less prone to misalignment. Therefore, it can be expected that the *rocking*-PP is less sensitive concerning drift and more stable over time. The two Fourier transforms are compared side by side in figure 4.19 (C)).

In the very low frequency regime, it can be seen that the frequency transmission is more homogeneous in *rocking*-mode. This is expected because of the virtually smooth PP hole edge due to the *rocking*-motion. At frequencies above 0.11 1/\AA representing structures smaller 9 \AA , a Thon ring shift can be detected between static and *rocking*-mode. Most probably, this shift is present in the whole image but is less visible in the broader transmission bands in the low - medium frequency regime. An interpretation for this phenomenon is more difficult. A possible explanation may be that static charging, which typically builds up on the surface of a PP in static-mode is effected, either reduced or even destroyed by the *rocking*-motion of the PP. Static charging of the PP can either influence the phase shift itself or add an additional focus change [105] both manifesting in a shift of the Thon rings. The transmitted resolution itself is not influenced by this. Since the primary goal of the current experiment was the effect of the *rocking*-mode on the resolution this Thon-ring shift was not further examined.

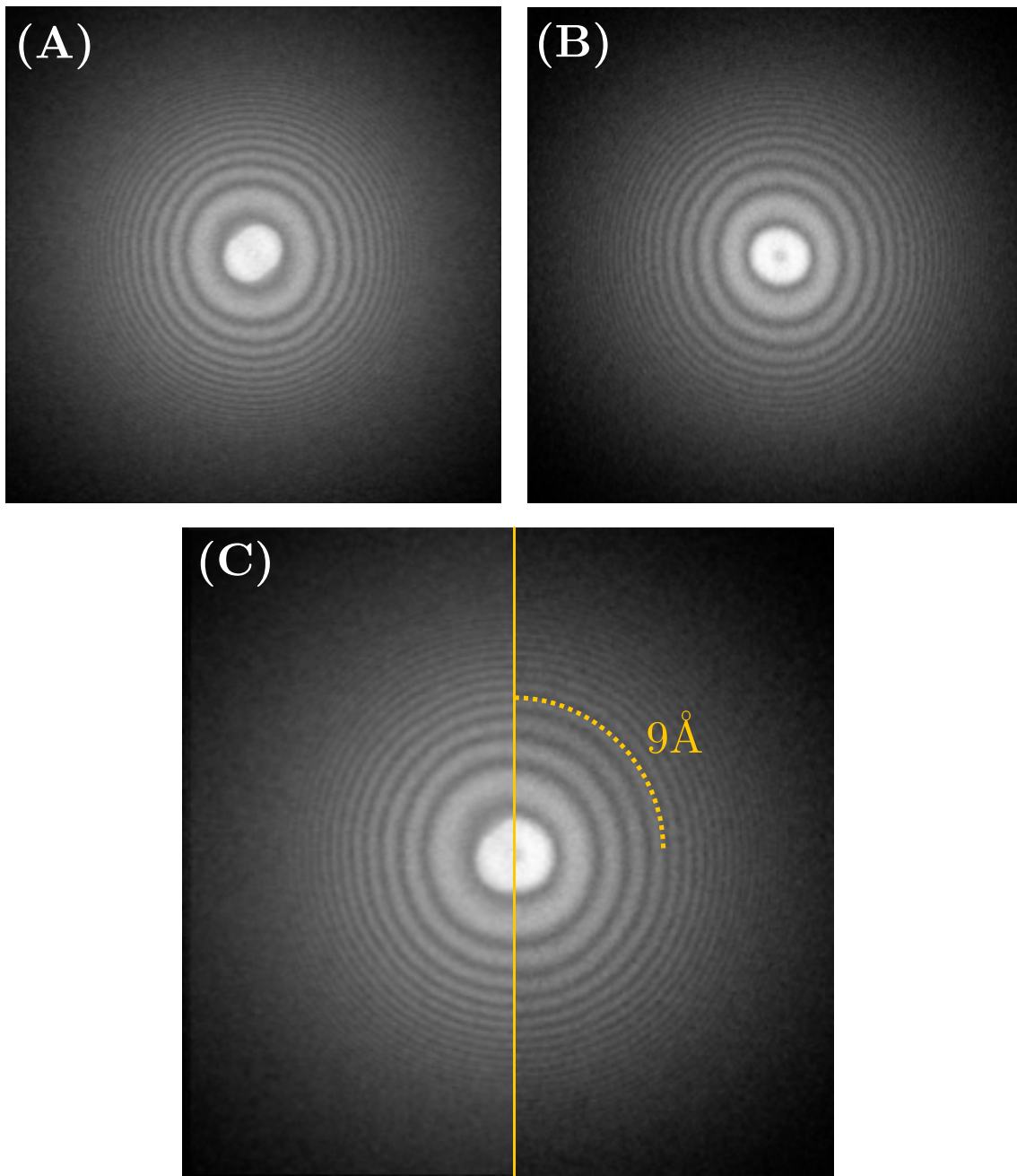


Figure 4.19: Fourier transforms of TEM micrographs acquired with PP in static-mode (A) and *rocking*-mode (B). (C) Side-by-side comparison of (A) and (B). [111]

***Rocking*-parameters**

The circular movement of the PP in *rocking*-mode can be adjusted by three parameters: circle-width [a.u.], rotation-speed [Hz] and aspect ratio [a.u.] (chapter 3.1).

At the beginning of this work, the *rocking*-mode was already implemented in the KonTEM software KonSHAKER [74], but this feature had never been tested in detail and no parameters were provided to set up proper phase-plate rotation.

Therefore, preliminary experiments were performed using *rocking*-mode to investigate the effect of the three *rocking*-parameters on resolution and signal transmission.

As a first step, the *rocking*-amplitude was tested. Micrographs of negatively stained apoferritin on carbon film were recorded at 59,000x magnification using the PP in *rocking*-mode. Figure 4.20 shows four Fourier transforms of TEM micrographs using multiple values for the *rocking*-amplitude while the other two parameters were kept unchanged (rotation-speed 25 Hz, aspect ratio 2 [a.u.]). The yellow arrows mark the information limit. Amplitude values, below or equal 12 [a.u.], do not have an effect on the resolution (fig. 4.20 (A)-(C)). Values higher than 12 [a.u.] limit the resolution significantly and information below 11 Å is not transmitted (fig. 4.20 (D)).

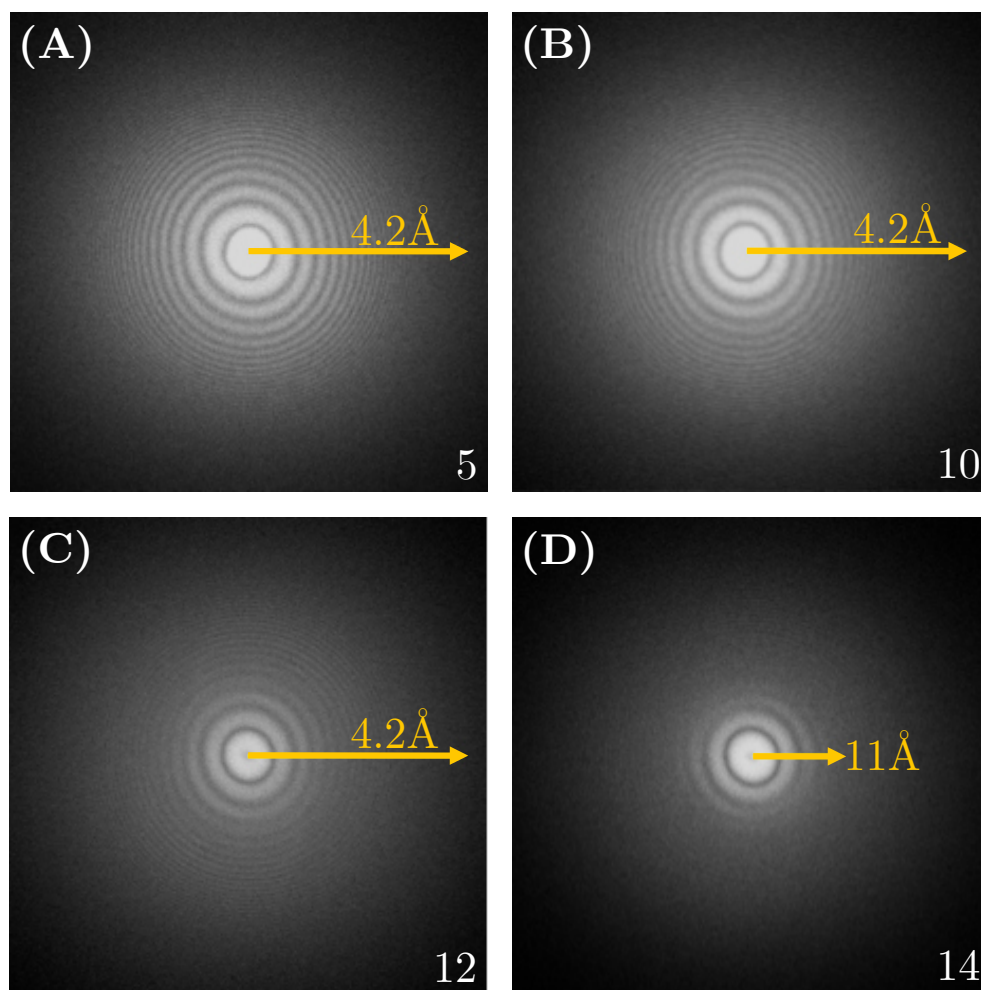


Figure 4.20: Variation of *rocking*-amplitude [a.u.]. Resolution limits are marked with yellow arrows. Values above 12 [a.u.] limit the resolution significantly and signals below 11 Å are not transmitted [111].

In further experiments, the *rocking*-speed [Hz] was investigated. Like the experiment described above, micrographs of negatively stained apoferritin on carbon film were recorded using the same parameters as above [59,000x magnification (1.06 Å/pixel)]. Now the behavior of the PP using various rotation speed settings was tested. Circle-width and aspect ratio were kept constant during these experiments at 10 [a.u.] and 2 [a.u.]. Figure 4.21 shows that a change of the rotation-speed between 1 Hz and 5 Hz does not influence the resolution and signal transmission up to 4 Å. As the rotation-speed does not limit the resolution, the

value was selected in regards to the number of frames recorded per second. During data acquisition, 17 frames per second were recorded. Therefore, the rotation speed was typically set to 17 Hz for datasets acquired in *rocking*-mode.

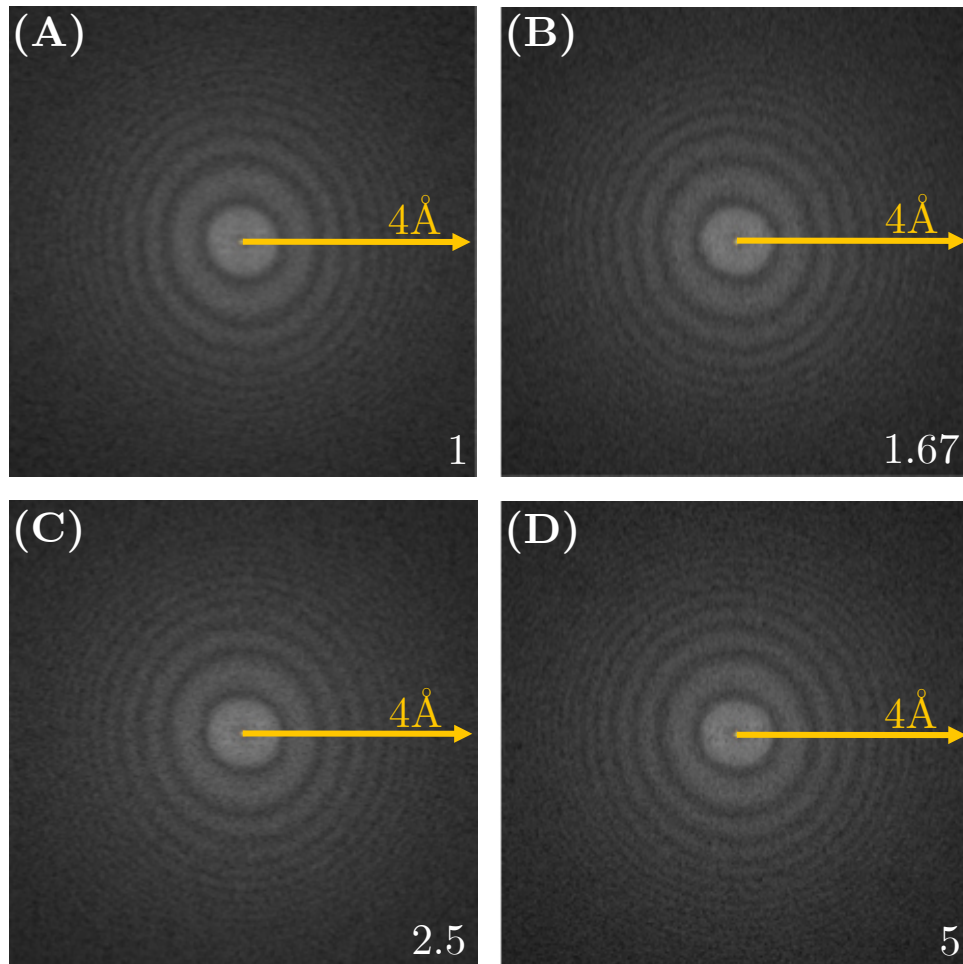


Figure 4.21: Variation of *rocking*-speed [Hz]. Resolution limits are marked with yellow arrows. Rotation-speed does not effect the information transfer up to 4 Å [111].

The third parameter, the aspect ratio, was selected based on visual check. In order to make the PP visible on the screen, the electron beam was diverged. To perform a circular movement, the PP aspect ratio value was set accordingly. Typically, the value was set between 1.5 and 2.5 [a.u.].

4.4 Discussion

In the current chapter, two possible fabrication processes for metal-based Zernike PPs are presented. Although the applied techniques are identical in both workflows, the results were significantly different. These differences and their advantages or disadvantages concerning the usability of the fabricated PPs are discussed in the following chapter.

Phase Plate Fabrication Workflows

From the two tested workflows herein, workflow I led to higher quality PPs. FIB milling of the amorphous carbon film allowed the fabrication of a PP hole with a sharp edge. FIB milling of a metal-coated carbon film instead, was less optimal. Here the PP film around the hole edge was bursted and the hole edge was bent upwards (fig. 4.6).

One explanation for the behavior of the metal film might go back to tensions between the two layers that arise during the sputtering process [113]. The energy that is brought into the system by the focused ion beam of 30 kV, can cause an immediate relaxation of the tension between the two layers, which might cause the deformation of the metal film. Gold, in particular, is known to build up high internal tensions.

An alternative explanation is that it is also possible that the metal film and the amorphous carbon film react differently on the bombardment with Ga ions. Potentially, the two materials could heat up differently. As the films are very thin (5-15 nm), and therefore not much energy will be absorbed, this explanation might be less likely.

It would have been interesting to further investigate the behavior of compounds of metal and carbon, for example, to analyze the bombarding direction by turning up the carbon film or by milling a pure metal film in the FIB. In the progress of the experiments, workflow I turned out to be an appropriate method for PP fabrication.

In workflow I, only the amorphous carbon film was milled using the FIB, leading to PP holes with sharp hole edges. Amorphous carbon film, in contrast to partly crystalline metal structures, might be better suited to mill structures into

an ultra-thin free-standing film (5 nm - 15 nm).

Impact of the Mean Inner Potential on the Phase Shift

The most crucial parameter of a thin film PP is its thickness. The thickness has to be set to a value that shifts the phase of the transmitted electron beam by, ideally, 90° . The phase shift is created by the inner potential of the thin film material [17]. The mean inner potential of a metal can be determined theoretically or experimentally. Experimental values of the mean inner potential can be obtained by measuring the deviation of an electron beam when it enters and leaves the crystal [114]. On the other hand, calculations of the mean inner potential are extremely difficult because no analytical expression for the mean inner potential is known [114]. On this account, it was too time-consuming to determine the mean inner potential of the used metals. Therefore, literature values were used for the calculation of the PP thickness.

Anishchenko et al. compared values of the mean inner potential using the TFD³ and TF⁴ models of a compressed atom with calculated and experimental values of the mean inner potential of some metals [115]. For the same metal, several values of the mean inner potential were published. This makes the exact calculation of the PP film thickness nearly impossible. Due to this difference between the values, a certain deviation from the ideal phase shift of 90° was expected. As one example, the mean inner potential of iridium [34.3 V (TFD), 37.8 V (TF)] results in a layer thickness of 7.02 nm (TFD) and 6.37 nm (TF) [115]. Ultimately, the difference in the layer thickness with just 0.65 nm is very small and corresponds to approximately four atom layers. To achieve this precision of the layer thickness is unlikely considering the production process for the thin metal film used herein. The magnetron sputtering process used for the fabrication of the PP film is terminated manually by closing the shutter a few seconds before the measuring quartz reaches the desired layer thickness. After closing the shutter, still some atoms in the vacuum chamber settle down on the target, which adds up to the metal layer. Therefore, a precision in the range of a few atom layers is not likely to accomplish. The layer thicknesses calculated based on the literature values was used as a refer-

³Thomas-Fermi-Dirac

⁴Thomas-Fermi

ence. Therefore, the actual phase shift had to be confirmed during the application of the PP in the TEM. During the first single-particle data acquisitions with the PP, an average phase shift of 60° was determined. Hence, the thickness of the PP was adapted for the production of further PPs.

Gold-Palladium Phase Plate Films

Besides the thickness of the PP film, the morphology of the film is of similar importance for the performance of the PP. A PP film should show an even thickness, since already small variations will change the phase shift. A second important point is crystallinity of the film. Ideally, the film is amorphous, to ensure an homogeneous scattering of the beam. In crystalline films, it can occur that image artifacts appear, caused by the diffraction of the electron beam by the PP film. Therefore, amorphous carbon was typically used for Zernike PPs. The PP films used in this work are nano- or polycrystalline and were tested to not limit the resolution or information transfer by such effects.

In previous studies, metals showed good properties as a potential PP material but have never been tested as a PP without additional support layers. Here, pure metal films without additional support layers were used.

The first batch of PPs was made of gold-palladium alloy. Figure 4.9 shows images of such a gold-palladium PP. The PP film shows cracks and material clusters. These clusters grow due to a rather high surface tension of the gold films [107]. Such inhomogeneous metal films stand in contradiction to the requirements for an optimal PP film. Cracks, as well as irregular density of material in the PP film, adversely influence the phase shift. This led to the conclusion that gold-palladium is not suitable as a material for a metal based thin film PP.

Iridium Phase Plate Films

As a second PP material, iridium was used. Iridium is a material known to form homogeneous metal films when using sputter deposition. A variation in density as observed in the gold-palladium films could not be found in the fabricated iridium films (fig. 4.10 (A)). The performance of iridium PP films will be discussed further down in this chapter.

However, very small denser spots could also be detected in the iridium film (fig. 4.10 (B)). One possibility for these small spots can be contaminations of the carbon support film, which are present from the beginning or occur during the ion-beam lithography fabrication step. During the magnetron sputtering process, the contaminants are enclosed by the iridium atoms and cannot be removed by plasma etching.

Another explanation might be that larger iridium grains are formed during the sputtering process. Influences of these clusters on the performance of the PP were observed if the dense spots were found close to the PP hole.

Clusters in the direct vicinity of the PP hole favor charging of the PP and disqualify PPs for high resolution cryo applications. Since there are always multiple PPs on each grid, this was usually no problem during this project.

Phase Plate Durability Optimization

Charging and ageing are known obstacles of PPs. Marko et al. showed that iridium shows a good charging resistance [105]. However, charging of iridium PP could be observed during PP application.

Charging is mainly caused by contaminations on the PP film. Contaminations can already be present from the beginning, caused during FIB milling of the PP hole. Oxid layers, as a source of contamination, might occur during the installation of the PP into the TEM, but can be ruled out for iridium PP films, due to the chemical characteristics of iridium. Besides, nonconductive contaminants, which are present in the TEM column can build up on the PP film over time. Additionally, contaminations grow based on electron-beam induced decomposition and deposition [116].

In order to prevent and reduce charging, two methods have been applied in this work. One known method to reduce charging is heating the PP [105]. Therefore, a heating element was used herein. Heating the PP can drive-off contaminants and might reduce their build-up [105]. However, in our case, heating the PP does not completely solve the charging problem.

To further reduce contaminations, a plasma asher was attached directly to the TEM column. By plasma etching the TEM column using a nitrogen/oxygen plasma, existing contaminants inside the microscope can be reduced or even com-

pletely eliminated. Besides, contaminations on the PP film occurring during the installation or application of the PP, can be removed from the PP film by plasma etching. The reduction of contaminants inside the TEM as well as on the PP film, can still not avoid charging effects completely. It could be observed that the reduction of contaminants results in a significant lifetime extension of the PP.

Phase Plate Hole Diameter

The performance of a PP is not only determined by the mean inner potential and the layer thickness of the PP material. Yet another crucial parameter, influencing the phase shift, is the diameter of the PP hole respectively the cut-on periodicity. Fukuda et al. investigated the relation between phase-contrast enhancement and the hole diameter of a Zernike PP [109]. Simulations of an infinitely small central hole, of a Zernike PP, showed an extensive contrast enhancement. In reality, the minimal usable hole size depends on the parameters of the TEM [110]. Limiting factors are the electron source and the lenses, which determine the size of the central beam in the diffraction plane. The PP hole must be of sufficient diameter for the unscattered part of the electron beam to pass through.

In this work, experiments were made with a PP hole diameter of 1 μm . Figure 4.15 shows that centering the 1 μm PP hole in the diffraction plane was not possible without artifacts appearing in the image caused by the PP hole edge. Even if microscopes, as the Titan Krios, equipped with a FEG have a central spot size of just tens of nanometers [110], the microscope conditions did not allow small PP hole diameters of 1 μm or smaller.

This was not a problem as a PP grid possessed meshes with several PP hole diameters between 0.5 μm - 4 μm . Therefore, further experiments were carried out using PPs with a hole diameter of 2 μm or bigger. Here, artifacts from the PP did not appear in the image.

The *Rocking*-Phase Plate

Increasing the phase-plate hole diameter is one method of avoiding fringe artifacts from appearing in the image. However, a smaller hole diameter correlates with a contrast enhancement as more scattered electrons are phase-shifted by the PP. Here, a method called the *rocking*-technique is presented, which virtually reduces

the size of the PP hole by performing a circular motion (fig. 4.17). This allows the use of a larger PP hole diameter, which simplifies the centering process of the PP in the back focal plane. Fringing artifacts caused by the PP hole edge do not appear in the TEM micrograph, while virtually reducing the PP hole diameter to enhance contrast.

Besides the effect of a virtually reduced hole size, the *rocking*-technique also has an effect on the behavior of the hole edge. A sharp PP hole edge, resembling a top hat like function, causes fringing artifacts due to an abrupt cut-on of the phase shift. Several attempts were made to reduce fringing artifacts by applying software filters to enhance low-frequencies [104] or by fabrication of a phase-plate film with a tapered PP hole edge [112]. Here, the *rocking*-technique is used, to virtually smoothen the PP hole edge by the continuous circulation of the PP. The stable circular movement of the PP during acquisition allows a more gaussian-like cut-on behavior of the PP hole edge.

Figure 4.19 shows the comparison of two Fourier transforms of TEM micrographs acquired with an iridium PP in static and *rocking*-mode.

In the region of very low frequencies, represented in the middle of the Fourier transform, it can be seen that the frequency transmission is more homogeneous in *rocking*-mode. This is expected because of the virtually smoothened PP hole edge due to the *rocking*-motion. At higher frequencies representing structures, smaller 9 \AA a Thon ring shift can be detected between static and *rocking*-mode. This shift might be present in the whole image, but is less visible in the broader Thon rings at low and medium frequencies.

An interpretation for this Thon ring shift might be static charging, which typically builds up on the surface of a PP in static-mode, is effected when moving the PP. Charging may possibly be reduced or minimized by the *rocking*-motion of the PP. Static charging of the PP can force the PP to act like a lens and either influence the phase shift itself or add an additional focus change [105], both manifesting in a shift of the Thon rings. The transmitted resolution itself is not influenced by this. If the *rocking*-mode has any effect on the resolution it will be discussed in the following section.

***Rocking-PP* Parameters**

Kurth et al. presented the *rocking*-technique in 2014, but the parameters regulating the circular movement of the PP were never investigated. Therefore, the influence of the *rocking*-mode on the transmitted resolution was examined in this work. The circular movement can be adjusted by three parameters: circle-width [a.u.], rotation-speed [Hz] and aspect ratio [a.u.].

Figure 4.20 (A)-(D) show the effect of increasing the circle-width [a.u.], respectively the *rocking*-amplitude. At higher amplitudes above > 12 [a.u.], the resolution is limited to 11 \AA . One possible explanation may be that by increasing the amplitude, the PP hole gets virtually smaller. At a certain amplitude the PP hole is so small that even the unscattered part of the electron beam is passing through the PP film and therefore also phase shifted. Thereby, the principle of a Zernike-based phase shift by adding a phase shift to the scattered part compared to the unscattered part of the electron beam is no longer given.

The aspect ratio may behave in a comparable way as the circle-width, as these two parameters are describing the circular deflection. The aspect ratio was set to a value to adjust the circular movement of the PP. If this parameter is set to a value, which causes the PP to perform a non circular movement, it may limit the resolution in a similar way as the *rocking*-amplitude, but primarily in one direction. Compared to the other two *rocking*-parameters, the *rocking*-speed (rotation-speed [Hz]) did not show any limitations in the transmitted resolutions. Figure 4.21 shows Fourier transforms of TEM micrographs acquired with a *rocking*-PP at different rotation-speed. Here, no resolution limitation could be observed.

Chapter 5

Application of the Phase Plate for Single-Particle Analysis

Once the development and pre-experiments for the PP were determined, the acquisition of single-particle datasets could start. Before generating phase-plate data, it was necessary to establish a standard workflow for single-particle acquisition and processing. According to the Nyquist theorem, the resolution is limited to 2x the detector pixel size. For the microscope at caesar, at a magnification of 59,000 (pixel size 1.06 Å), the theoretical resolution limit would therefore be 2.12 Å. In order to identify the actual resolution limit at a magnification of 59,000, a cryo-dataset without PP was acquired as a starting point.

Apoferitin was used for all experiments in this project. Apoferitin is an ideal benchmark sample and is used as a standard cryo-test sample in labs all over the world. It is a very stable protein, easy to obtain and the structure of apoferitin is well-known [51, 62, 63, 65]. For the first experiments horse apoferitin (A3641), which is commercially available (*Sigma-Aldrich*), was used. Later, it was found that the resolution of horse apoferitin from *Sigma-Aldrich* is limited to a resolution of 3.5 Å [78]. Hence, the sample was changed from horse to mouse apoferitin from the Kikkawa lab (University of Tokyo). Mouse apoferitin has been proven to exceed a resolution of 3.5 Å [64] and was therefore, used as the sample for the compared datasets in this work.

5.1 Sample Preparation and Vitrification of Mouse Apoferritin

The mouse apoferritin used in this work was provided by the Kikkawa lab at the University of Tokyo [24]. Protein expression and purification of mouse (mus musculus) apoferritin were adapted to the protocol of M. Wu. et al. [64].

Holey carbon grids, (R1/2, 200 mesh *Quantifoil*) were plasma cleaned for two minutes using an Argon plasma cleaner MED 010 (*Balzers*). 4 μ l sample solution (4.5 μ l apoferritin 6 mg/ml in TBS + 0.5 μ l 0,1 % fOM [10 mM HEPES pH 7.4, 150 mM NaCl]) was applied onto the hydrophilic grid in the chamber of the Leica EM-GP II plunger (*Leica Microsystems*). Automated blotting was performed for 2-3 seconds using Whatman filter paper grade 2 (*Whatman*). The chamber of the Leica EM-GP II plunger was set to 95 % humidity and 20 °C temperature. The TEM grid was plunged into liquid ethane cooled by liquid nitrogen. The grids were stored in a cryo grid box in liquid nitrogen until the data acquisition.

Protein purification and vitrification of mouse apoferritin used herein, is further described in chapter 3.2.1.

5.2 Prerequisites

Independent from the mode - normal cryo-EM or PP cryo-EM - several alignment steps have to be performed to prepare the Titan Krios for single-particle data acquisition.

The microscope alignment procedure was performed on continuous carbon film at eucentric height and eucentric focus following the FEI manual [69].

Gun shift is the first alignment step to be made. During the data-acquisition workflow, magnifications and spot sizes change back and forth. To minimize the movements between different spot numbers, and to assure a correctly aligned beam along the optical axis for all spot numbers, the gun shift has to be adjusted.

For high-resolution imaging, the pivot points are the second important calibration. Here, the tilt and shift of the double deflection coils are decoupled. This alignment

guarantees a pure shift and no tilt if a shift is intended and vice versa.

The beam shift alignment is performed by adjusting the beam deflection coils. They are situated above the objective lens and are important in many alignment steps. The beam deflection coils are used to align the objective lens and the correct beam movement, caused by the condenser stigmator.

The rotation center calibration makes sure that the beam is aligned along the optical axis of the objective lens. This minimizes lens aberrations and image movement during focusing. Before the final adjustment, the condenser stigmator has to be aligned to make the focused beam circular.

As a final pre-alignment, the C_s corrector has to be checked prior to data acquisition. The C_s corrector minimizes the effect of delocalization, which corresponds to the correction of spherical aberrations.

Leginon MSI-Edge workflow

Data acquisition was performed using the software Leginon 3.1. [82]. After recording an ATLAS to get an overview of the complete grid, good meshes with sufficient ice quality were selected in the square target step. During hole targeting, positions for the later acquisition were selected. The final target to acquire the high magnification micrographs were set in the exposure targeting step.

A more detailed description of the software composition and a schematic overview (fig. 3.11) of the standard MSI-Edge acquisition workflow used herein, can be found in chapter 3.2.3.

5.3 Reference Dataset - Single-Particle Analysis of Mouse Apoferritin without a Phase Plate

5.3.1 Data Acquisition - Electron Microscopy

For the reference dataset, 872 movies were automatically acquired using the FEI Titan Krios operated at 300 kV equipped with a FalconII detector. Each movie includes 17 frames with a total dose of $35.7 \text{ e}^-/\text{\AA}^2$ at a nominal magnification of 59,000x ($1.06 \text{ \AA}/\text{pixel}$). Images were acquired using the MSI-Edge workflow in Legion3.1 [82] with a set defocus range of $-1 \mu\text{m}$ to $-2.5 \mu\text{m}$.

A list of all data acquisition parameters is shown in table 5.1. An overview about all parameters, including data collection, sample information and data processing can be found in appendix C.9.

Table 5.1: Data collection parameters of the mouse apoferritin reference dataset.

Mouse Apoferritin Reference Dataset without PP	
Instrument	Titan Krios
Voltage [kV]	300
Magnification	59,000x
Pixel size [\AA]	1.06
C2 aperture [μm]	100
Objective aperture	yes
Exposure time [s]	3
Electron dose per frame [$\text{e}^-/\text{\AA}^2$]	0.7
Total electron dose [$\text{e}^-/\text{\AA}^2$]	35.7
Defocus range [μm]	-1 – -2.5
Number of frames per movie [no.]	17
Total number of micrographs [no.]	872

5.3.2 Single-Particle Reconstruction - Image Processing

Image processing started with motion correction of the 872 movies using the software MotionCor2 [93]. The first and last two frames were discarded due to shuttering artifacts caused by the mechanical camera shutter. The remaining frames were averaged over three frames to improve the signal to noise ratio. A selection of motion-corrected micrographs is shown in figure 5.1.

The averaged micrographs were then manually inspected using e2boxer (EMAN2) [87]. Images of insufficient quality, e.g. showing no particles, ice contamination or too much carbon film on the image were discarded. 476 images were left for further processing. In the next step, dose weighted micrographs were imported into the software package RELION [83] followed by CTF estimation using CTFFIND4 [90] (tab. 5.2). After CTF-estimation, images ran through a second quality check. In this step, CTF is numerically fitted to the images power spectra and images are then selected based on thresholds for e.g. focus ($-0.5\ \mu\text{m}$ to $-2.5\ \mu\text{m}$), resolution ($6\ \text{\AA}$) and astigmatism ($0.15\ \mu\text{m}$). After this step, 311 micrographs were left for processing.

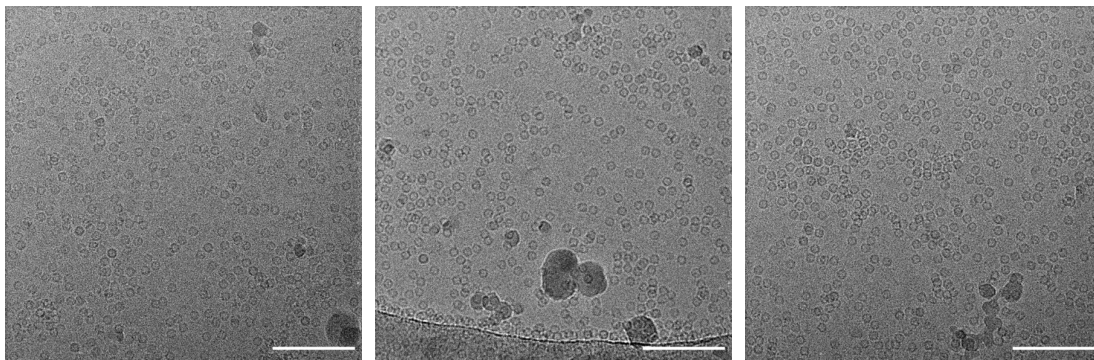


Figure 5.1: Selection of motion-corrected micrographs from the reference dataset acquired without PP. The contrast was enhanced by histogram equalization. Scale bars: 100 nm.

Table 5.2: Parameters used for CTF estimation in CTFFIND4.

Parameters for CTF estimation	
Spherical aberration [mm]	0.01
Voltage [kV]	300
Amplitude contrast	0.1
Magnified pixel size [\AA]	1.06
Amount of astigmatism [\AA]	500
FFT box size [pixel]	512
Minimum resolution [\AA]	30
Maximum resolution [\AA]	5
Minimum defocus value [\AA]	5000
Maximum defocus value [\AA]	50000
Defocus step size [\AA]	500

Automated particle picking was performed using crYOLO [88, 89]. crYOLO uses neuronal networks for particle picking. Particles were picked without training using the general model trained for low-pass filtered images on the remaining micrographs. 94,488 particles were found in 311 micrographs, which were imported and extracted in RELION.

2D classification, with 94/91 classes, was performed four times on the picked particles applying a circular mask of 136\AA to remove false positives. 91,591 particles out of the best two dimensional classes were used to create an initial model in RELION shown in figure 5.2 applying a circular mask of 160\AA and octahedral symmetry. The initial model in figure 5.2 shows already the helices of the protein as well as the four-fold, two-fold and three-fold channel.

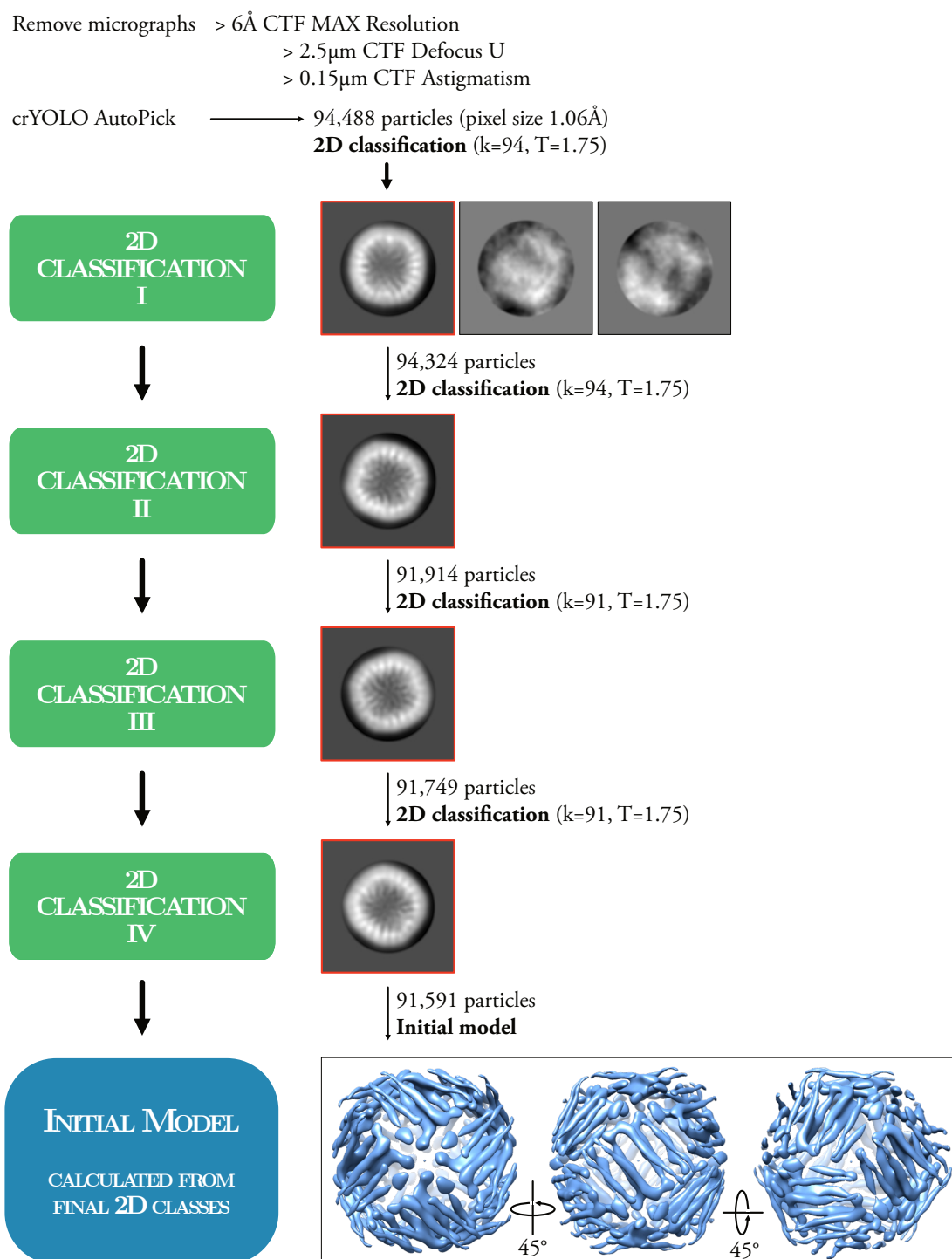


Figure 5.2: Data reconstruction workflow showing the processing steps using the software RELION. Micrographs were discarded according to resolution, defocus and astigmatism thresholds. 94,488 particles were picked out of 311 micrographs. 2D classification was performed four times to remove false positives. The best 2D class average from 2D classification IV consisting of 91,591 was selected to create an initial model, which is shown here in blue from three different directions. Densities of the different helices can be seen as well as the four-fold, two-fold and three-fold channel.

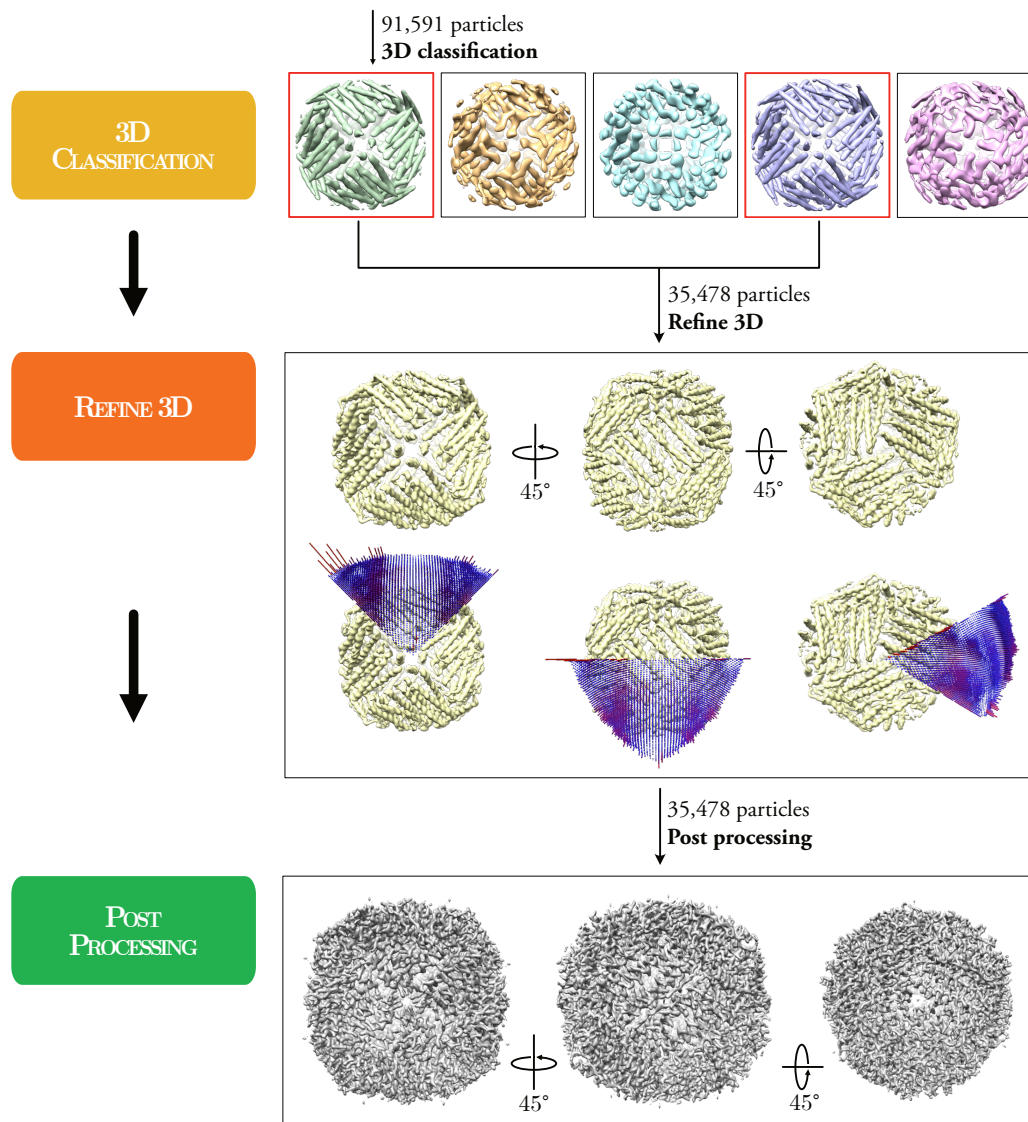


Figure 5.3: The 91,591 out of 2D classification IV were further used for 3D classification with five classes applying a circular mask of 160 Å and octahedral symmetry. Two out of this five 3D classes, here marked in orange, containing 35,478 particles were selected for 3D auto-refine. After the 3D refinement step, the turns of the single helices can be seen in the map. The red and blue columns shown around the 3D refined model indicate the distribution of the views. It can be seen that the angles are well distributed around the particle. Post processing was the last performed reconstruction step where the previous map was further sharpened down to 3.4 Å resolution.

The same particles were used for 3D classification with five classes applying the same mask and symmetry.

The two orange marked, best looking classes (fig. 5.3), including 35,478 particles were selected for 3D auto-refinement with imposed octahedral symmetry. The 3D refined density map shows already increased resolution as the turns of the helices are visible. The blue and red columns in figure 5.3 give information about the distribution of views of the protein. Here, the views are well distributed over the protein density map.

The unfiltered half map from 3D auto-refinement was sharpened during post processing, resulting in a final resolution of 3.37763 Å shown in the FSC (fig. 5.4).

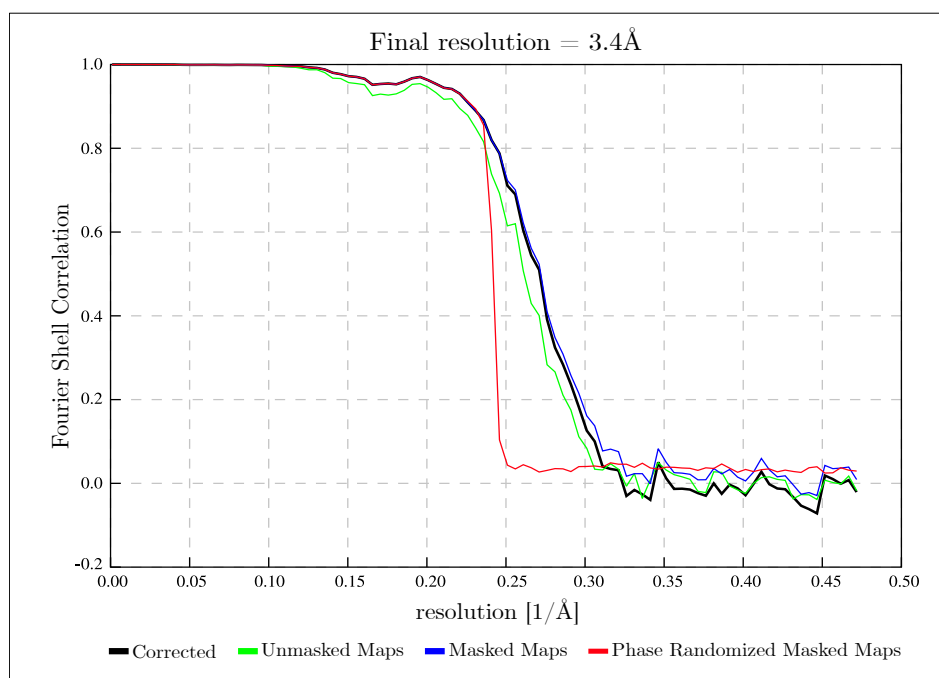


Figure 5.4: Fourier shell correlation plot for the final 3D reconstruction shown in figure 5.3. At an FSC of a reported value of 0.143 the resolution reaches 3.4 Å.

Figure 5.5 shows apoferritin chains I, K, and E segmented out of the final 3.4 Å post-processing density map. The PDB¹ model (light blue) (PDB code 6v21) was fitted to the electron density map (gray mesh) reaching a correlation of 0.8058.

¹RCSB Protein Data Bank

Local resolution of this map is good enough to see the side chains.

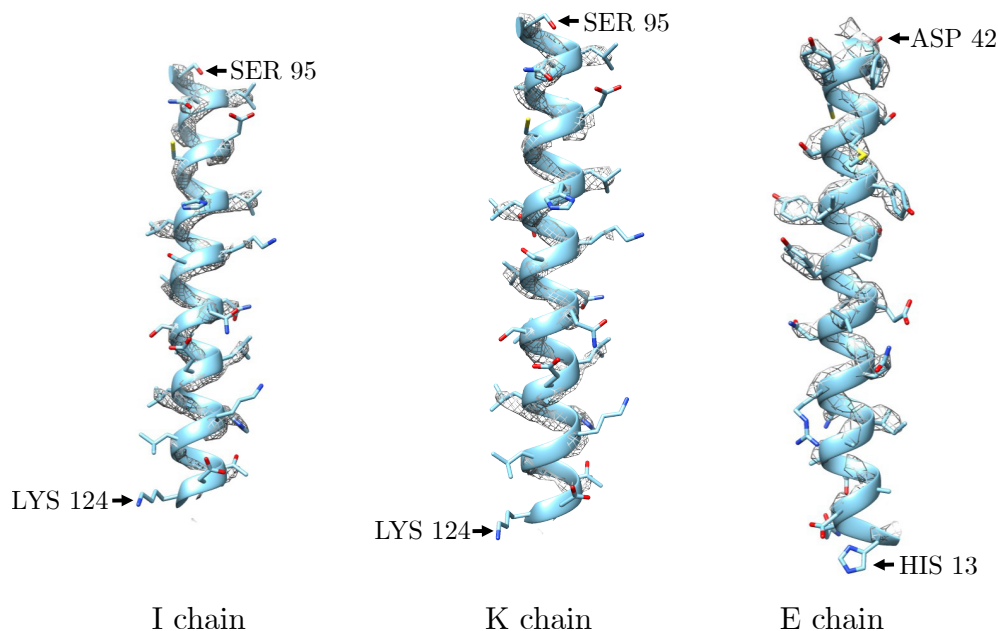


Figure 5.5: Selection of apoferritin helices of the final post-processing cryo-EM potential map (gray mesh) with fitted PDB model (light blue) (PDB code 6v21 [64]). All EM densities are shown in contour level 0.192.

For this final reference dataset with a resolution of 3.4 \AA , a lot more datasets were acquired. Table 5.3 lists all datasets acquired in 2020 without a PP. Earlier datasets were not considered for further investigation.

Table 5.3: List of apoferritin datasets acquired without a PP.

Dataset	Magnification	Sample	No of Micrographs
2020-03-08-Apo	75k	horse apoferritin	1159
2020-03-31-mApo	59k	mouse apoferritin	2265
2020-04-05-mApo	59k	mouse apoferritin	2215
2020-05-18-mApo	59k	mouse apoferritin	2218
2020-06-30-mApo	59k	mouse apoferritin	1946
2020-11-23-mApo	75k	mouse apoferritin	177
2020-11-23-mApo	59k	mouse apoferritin	872

5.3.3 Discussion

Several reference datasets were recorded during the process of this thesis (tab. 5.3). Improvements of alignment procedures and sample preparation constantly enhanced the quality of the reference datasets.

The final dataset consisting of 872 micrographs reached a resolution of 3.4 Å. 311 micrographs were for refinement while 396 images had to be discarded due to bad sample quality e.g. ice contamination, crystalline ice, no ice or bad protein distribution. Another 165 images had to be removed because of high astigmatism and high defocus. An even better alignment of the microscope might reduce the number of discarded micrographs due to astigmatism and defocus. But, the effort for a more precise alignment is disproportionate to the amount of micrographs gained by a better alignment. The faster and more efficient way is to acquire more data.

Finally, 311 micrographs containing 94,488 particles were used for processing. 35,478 particles contributed to the final three dimensional model resulting in 3.4 Å resolution. Further improved acquisition and reconstruction procedure led to a protocol for a quick microscope quality check. A fast acquisition and reconstruction procedure for test datasets allow a regular resolution quality check of the microscope e.g. after microscope maintenance.

A 3.4 Å structure of mouse apoferritin acquired with the Titan Krios at caesar is a good result. Nevertheless, 3.4 Å does not match the theoretically achievable resolution. According to Nyquist, the resolution for a nominal magnification of 59,000 should be double the pixel size of 1.06 Å, which corresponds to 2.12 Å.

Compared to the recent record of resolution for apoferritin, reaching 1.2 Å [65] in 2020, 3.4 Å sounds like a lot, but there are several things to keep in mind while comparing the two results. The first difference is the magnification Yip et. al used. By using a higher magnification (0.457 Å pixel size) and super resolution mode, higher resolution can be achieved.

Apart from higher magnifications, resolution can be improved by several technical improvements.

The Titan Krios at caesar is equipped with a Schottky-FEG, whereas the Titan

Krios G4 used in the studies of Yip et al. comes with a cold-FEG. A cold-FEG increases the SNR for high-spatial frequencies [65]. Besides a new generation of field-emission guns, DEDs have improved over the last years. While the Titan Krios at caesar is equipped with a Falcon II DED, more recent microscopes come with a Falcon 4 DED. The Falcon II camera has a frame rate of 18 Hz. Compared to this, the 3rd generation had already a frame rate of 40 Hz, whereas the Falcon 4 detector operates at 248 Hz. Yin et al. shows that using the same microscope equipped with a cold-FEG, a Falcon 4 detector, and a new energy filter improved the resolution from 1.65 Å to 1.2 Å using even less particles. Therefore, it can be expected that with a new cold-FEG, an energy filter and a new detector, the resolution could be further increased.

Another factor that affects the resolution is the alignment of the microscope. Furthermore, the resolution of the final three dimensional map can be improved during the reconstruction process. Wu et al. shows an improvement in resolution achieved by the different processing steps [64]. Besides the resolution improvement through the various reconstruction steps, the number of particles used for reconstruction has an influence on resolution. Yin et. al and Wu et. al show that the resolution increases with increasing numbers of particles used for resolution.

Keeping in mind that the older generation detector of the microscope, as well as the lower number of images and particles used for the reconstruction, 3.4 Å resolution is a good result for the given hardware.

5.4 Modifications for PP Application

A PP is an additional device inserted into the microscope column. This causes some limitations and requires modifications of the standard acquisition workflow. Some steps could not be implemented the same way with and without PP. The required modifications and final protocol for PP data acquisition are presented in the following chapter.

5.4.1 Leginon Workflow for Phase Plate Data Acquisition

The MSI-Edge workflow, which is part of the Leginon software package, presented in chapter 3.2.3 served as a template for data acquisition experiments with the PP. The order of the independent acquisition steps, starting with acquiring an atlas mosaic, the selection of the meshes, followed by the selection of holes and finally exposure targets had to remain the same as for standard acquisition. Also, when using the PP, the magnification is changed from low (85x) to high magnification (59,000x). In the process of the experiments, I found that not all steps of the workflow could be performed with the PP inserted. This will be discussed later in this section. The first question that needed to be answered was, which steps could be performed with the PP inserted and which steps had to be done without the PP.

Here, it turned out that all steps using a magnification $< 59,000$ ($1.06 \text{ \AA}/\text{pixel}$) and all steps that were recorded at a different illumination than the final acquisition setting had to be recorded without PP. For small magnifications, the micrograph would always overlap with an image of the PP. While in low magnification mode, the complete PP grid would overlap with the micrographs for slightly smaller magnifications than 59,000x ($1.06 \text{ \AA}/\text{pixel}$). Only the PP film and the PP hole would appear in the micrograph. For very thin PP films such as the iridium PPs with a fine-grain thin film of just a few nanometers thickness, the holes of the grid should still be visible. Thicker PPs of other materials would completely cover the original sample image and no other structures could be seen in the micrograph. Besides, the PP would be unnecessarily exposed to the electron beam, which speeds

up the process of charging and ageing of the PP. The PP needs to be prevented from unnecessary exposure to the electron beam to not reduce the lifetime of the PP. Therefore, the idea was to just use the PP for the final exposure micrographs at a nominal magnification of 59,000 (1.06 Å/pixel).

The Leginon MSI-Edge workflow used for the reference dataset (chapter 3.2.3) changes the microscope settings for each acquisition step. Hence, the workflow had to be divided into two parts: with and without the PP. Figure 5.6 shows the workflow with the changes made for PP data acquisition. First, all steps starting from atlas acquisition (**A**) up to exposure targeting (**C**) were made without the PP. Then, the PP was inserted and properly aligned in the back focal plane of the objective lens. Once the drift of the PP had settled, the acquisition of the exposure targets were started. Leginon provides such possibilities. It is possible to send image positions to a queueing system and process this queue in a separate run. Using this technique allowed us to completely setup the experiment without the PP. After all preparations had been finished, the PP was inserted and all acquisition targets could be recorded without changing any microscope settings. Dividing the workflow into two cycles required further changes.

For good micrographs, it is important to determine the correct defocus value. The MSI workflow determines the defocus at two points during the data acquisition process. At first, a eucentric focus target is set during the hole targeting step. In this step, the mechanical height of the sample inside the microscope is adjusted. The eucentric focus routine is performed before each exposure targeting step. In order to assure the correct focus of the final micrographs, the defocus is rechecked in an additional defocus measurement. The defocus is measured and corrected if needed after every third exposure micrograph. Here, the defocus is rechecked by performing a focus routine, using image shift and beam tilt. This second focus routine is performed during the final exposure run and would be thus performed with the PP inserted. However, once the PP is centered, every setting that affects the beam leads to a misalignment of the PP. As the focus routine uses image shift and beam tilt to determine the defocus, the PP will appear in the image. During the defocus determination process, the PP overlaps the micrographs. On the basis of these micrographs, the defocus value is estimated.

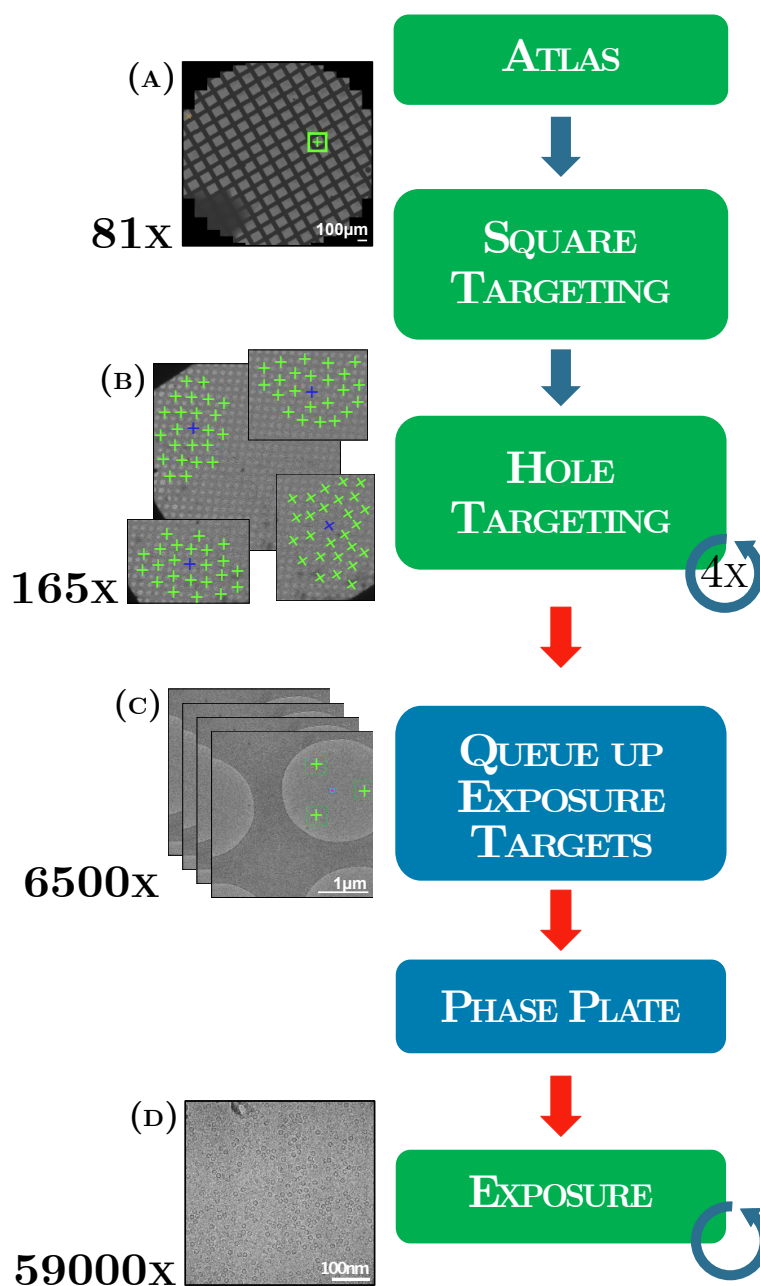


Figure 5.6: Schematic overview of the modified MSI-Edge workflow using Legion 3.1 for PP data acquisition. (A) The ATLAS is a composition of several low magnification images acquired at 81x magnification. Meshes for further acquisition are selected and indicated by a green cross (Square Targeting). (B) Low magnification images at 165x. Holes with suitable ice thickness are manually selected, shown by green crosses. A blue cross indicates the position for a eucentric height focus determination. This step is repeated four times per mesh as targets are selected in one quarter of a mesh. (C) Images acquired at 6500x ($9.93 \text{ \AA}/\text{pixel}$) intermediate magnification showing a complete hole filled with thin amorphous ice. Green boxes indicate the position for high magnification exposure images. This step is repeated till all exposure targets are set. The exposure target positions are queued until the PP is inserted and centered. (D) Final exposure image acquired at 59,000x magnification ($1.06 \text{ \AA}/\text{pixel}$) using a PP showing apoferritin proteins embedded in vitreous ice.

However, the PP appearing in these images leads to a misinterpretation of the micrographs and therefore to a wrong focus estimation. As a result, the focus determination between the final exposure images has to be skipped.

Nevertheless, a correct defocus is essential for good data. Micrographs, which exceed the defocus threshold of $-0.5\ \mu\text{m}$ and $-2.5\ \mu\text{m}$ are not used for processing and are discarded. It is of importance to assure a defocus inside the target threshold. Therefore, an additional experiment has to be performed, which is explained in the following section.

5.4.2 Focus-Distance Test

The herein used MSI-Edge workflow, which is part of the Legikon software had to be modified for data acquisition using a PP. It turned out that the regular defocus check between the final exposure micrographs could not be performed with an inserted PP. Therefore, this defocus readjustment step had to be skipped in the PP workflow. However, the defocus value is very important for good data quality. Only the mechanical eucentric focus can be determined during the PP workflow. It is important to assure that the focus value does not exceed the defocus threshold of $-0.5\ \mu\text{m}$ and $-2.5\ \mu\text{m}$. Hence, it was necessary to perform an experiment to check the precision of the eucentric focus routine.

For the experiment, a holey carbon grid R2/1 with a 5 nm continuous carbon layer (*Quantifoil*) is used under cryo conditions. The additional 5 nm carbon film guarantees sufficient contrast and signal in the Fourier transform to precisely determine the CTF, which is needed for defocus measurement. It is important to generate the same conditions as during a normal data acquisition to create comparable experimental conditions. Therefore, the experiment was performed under cryo conditions. All microscope settings for data acquisition remained the same as listed in tables 3.7 and 5.1.

In several runs, various target positions were checked. For the experiments, performed herein, only one eucentric focus target was set per mesh. Any further defocus estimation using image shift and beam tilt were left out. The exposure targets were selected individually for each run. Figure 5.7 shows in the upper right corner of each diagram the target distribution (green crosses) around the eucentric focus target (blue). Three different patterns around the eucentric focus target are shown here: (A) in a line on one side of the target, (B) second right and left from the target and (C) last circular distribution around the target. Figure 5.7 shows the data evaluation using the pre-processing script from Elmar Behrmann and Stephan Irsen. In all three experiments, the majority of the micrographs are detected inside the target threshold. Even for data acquisition, using the second focus routine between the final micrographs, a certain percentage always exceeds the threshold. Variations in defocus values, as observed in the diagram, are expected due to the inhomogeneous sample height. Various defocus values inside the threshold are wanted, and normally gained, by setting a defocus range.

The focus values could be out of range, the bigger the distance between the eucentric focus target and the hole target. Hole targets needed to be set in a small distance to the eucentric focus target. In order to still be able to use the complete mesh for acquisition, the workflow had to be further modified. Therefore, the mesh was divided into four parts by setting four eucentric focus targets per square (fig. 5.6 (B)). During hole targeting, only one fourth of the holes of the mesh were selected in order to keep the focus variation small and inside the threshold.

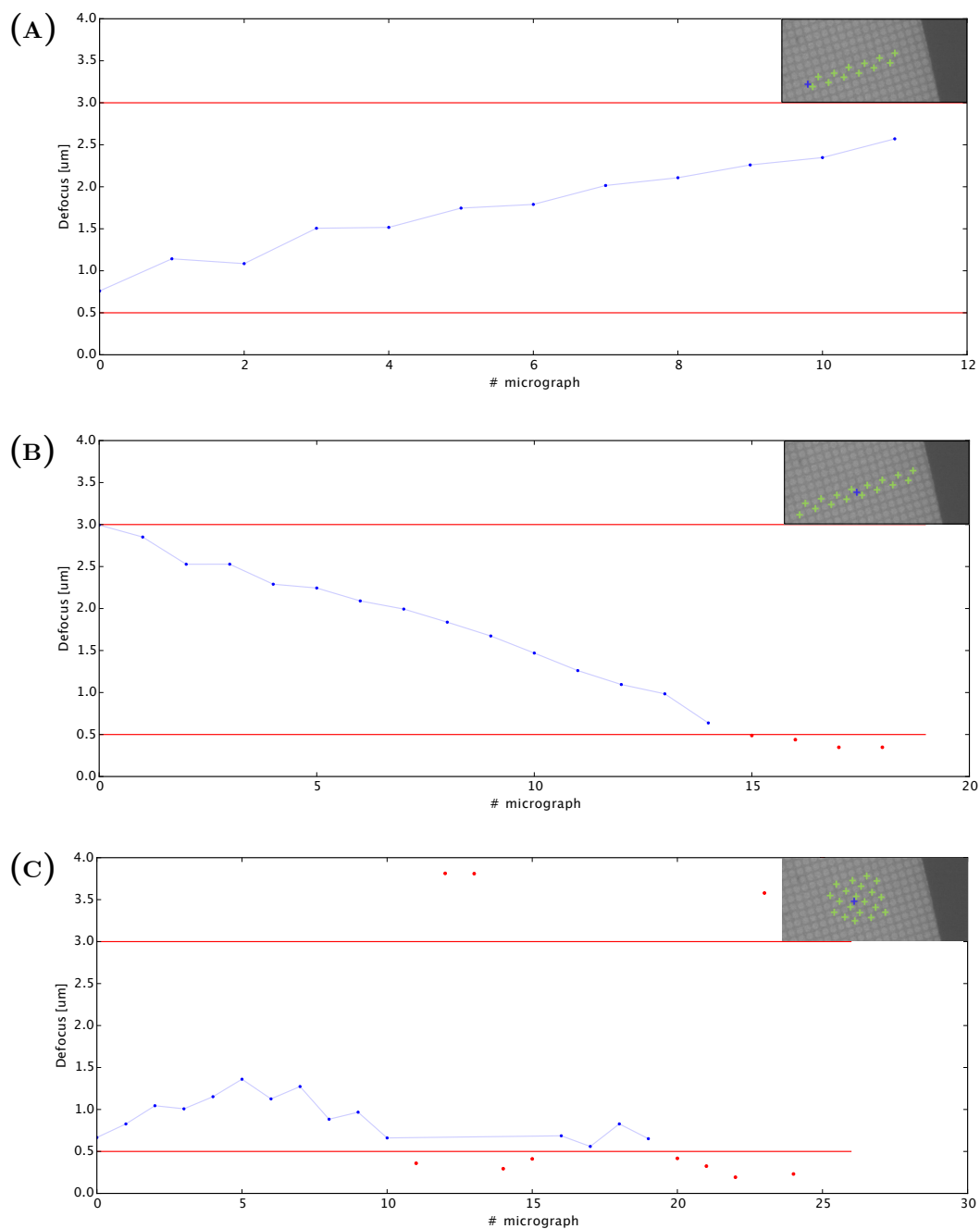


Figure 5.7: Focus distance test using Legikon 3.1. (A) distribution of hole targets right of eucentric height focus target (B) left and right distribution of hole targets around eucentric height focus target (C) circular distribution of hole targets around eucentric height focus target.

5.4.3 Phase Plate Positioning and Adjustment

For all PP acquisitions, the PP needed to be aligned inside the TEM. The procedure to center the PP in the back focal plane of the objective lens is described in this section.

The first step after installing a new PP grid inside the microscope is saving various positions as presets in the KonTROL software (fig. 3.3).

Besides the hole presets, three additional positions are defined: off - the PP holder is almost pulled back to its maximum, out - the PP is pulled back and not interfering with the electron beam, the objective aperture for normal data acquisition and the center of the PP grid.

To set these positions, the microscope settings used in the software Legikon for low magnification (85x) were used. Although technical measures were taken to prevent the system from damaging the PP (touch alarm), extra care had to be taken when moving the PP at high speed in low magnification mode. Once the preset positions have been saved, the PP positions can be stored. In the first step, the positions of the phase-plate meshes are stored using low magnification (85x), as mentioned above. The electron dose at 85x magnification is low enough to not damage the PP.

In the next step, the PP hole was finely adjusted starting at a magnification of 165x (9.93 Å/pixel), gradually increasing the magnification until the final magnification of 59,000x. At the same time, the PP hole needs to be kept in the center of the screen, using the piezo motors of the PP holder.

For long distance movements of the PP, holder drift occurs. Therefore, two hours were scheduled for the PP to settle before starting the precise centering of the PP in the back focal pane. For the final centering step, the setting, used to finally acquire the micrographs (e.g. magnification 59,000x (1.06 Å/pixel); illumination area 1.25 μm; spot size 6) was selected. It is important to perform this last procedure very quickly to keep the exposure of the PP to the electron beam as low as possible.

In this step, the C3 condenser lens gets involved in the centering process.

For manual fine tuning, the C3 lens can be varied within certain ranges by the MF-Y Fine Focus Back Focal Plane setting (for a detailed description see section 3.1).

To begin with, MF-Y Fine Focus is set to its minimum in order to bring the PP out of center and get an overview. The crossover is needed to find where the PP is correctly positioned in the back focal plane of the objective lens. Therefore, MF-Y Fine Focus is slowly and continuously increased. On the screen, the PP hole appears to get larger. At the same time the x-y position of the PP might need to be corrected to keep the PP hole centered. At the crossover, the PP hole stops to get larger and turns into getting smaller if the MF-Y Fine Focus is further increased. This is the point along the optical axis where the PP is correctly positioned. In order to check if the PP is properly centered along the x-y axis, it is helpful to look at the Fourier transform of a micrograph. Figure 5.8 shows a Fourier transform of a TEM micrograph acquired with the PP. The bright circle in the middle of the image is not round. This indicates a poorly centered PP along the x-y axis.

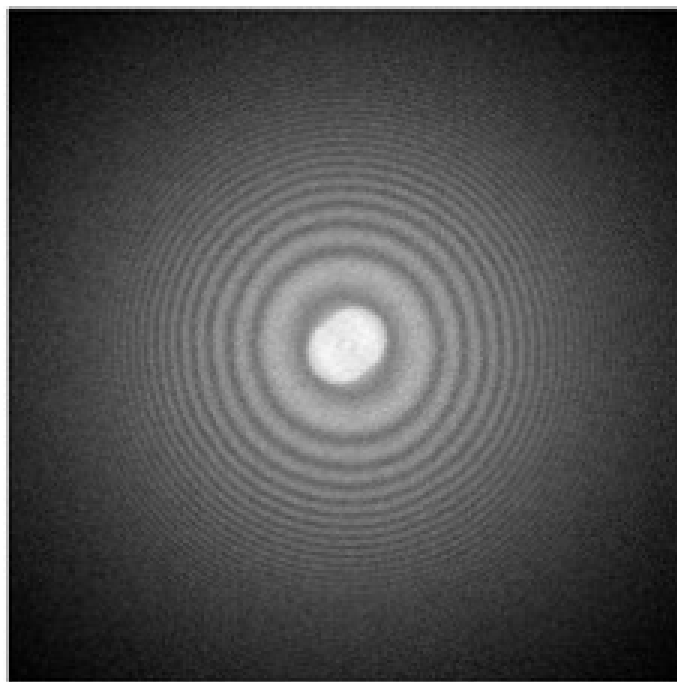


Figure 5.8: Fourier transform of a TEM micrograph acquired with the PP. The bright circle in the middle is not completely round due to a misalignment of the PP hole along the x-y axis.

5.4.4 Discussion

In order to perform PP data acquisition, several changes had to be made to the standard workflow for single particle data acquisition at caesar.

The changes in the data acquisition process could be implemented by changing the acquisition workflow order. Focus determination steps, between the final exposure acquisition, were replaced by additional eucentric focus determination routines. The preliminary setup for PP acquisition, following the modified workflow, requires more intervention of the operator. The modifications in the acquisition process have not been automated yet. Some steps, like performing hole targeting four times per mesh, might be further automated by changing the magnification. A higher magnification, to limit the image section to show a maximum of one fourth of the mesh, would allow automated hole target selection. However, the workflow will always be interrupted by inserting the PP, which will have to be done by the operator. Therefore, a fully automated PP data acquisition workflow will not be visible.

Using a Zernike based PP excludes the application of beam tilt and beam/image shift² except for very small changes. A change of beam tilt and image shift with a centered PP would result in a misalignment of the PP. These functions are usually used in a small radius to change from one exposure target to the next. As using a PP prohibits these functions, positions had to be changed by physical movement of the stage. After each stage movement, a waiting time of 30 seconds was implemented. The stage needed to settle before image acquisition to avoid artifacts caused by mechanical drift.

Furthermore, it should be mentioned that the Titan Krios at caesar is equipped with a C_s corrector. Aberrations and artifacts caused by the PP can be reduced up to a certain level by the C_s corrector.

Considering the total time for data acquisition using a PP, it is more time-consuming than a normal data acquisition. The increased acquisition time results from the longer waiting times such as settling of the PP drift or the precise adjustment of the PP in the back focal plane. However, the actual recording time

²In FEI cryo-TEM beam and image shift are connected.

of the micrographs is comparable to the normal workflow without the PP. The extended acquisition time is still in an acceptable range and speed optimization has not been part of this work.

5.5 Single Particle Analysis using the *Rocking-Phase Plate*

5.5.1 First Data Acquisition and Reconstruction using a *Rocking-Phase Plate*

For the first PP dataset, micrographs were acquired following the semi-automated acquisition workflow described in section 5.4.1. The used PP IrNo4 consisted of a 6.7 nm iridium film with a 2 μm PP hole. The PP was constantly heated before and during acquisition. The micrographs were recorded using the PP in *rocking*-mode, with the following settings: circle-width 8 [a.u.], frequency (resolution) 17 Hz and aspect-ratio 2 [a.u.].

Data Acquisition

In total 4229 movies were acquired using the FEI Titan Krios operated at 300 kV equipped with a Falcon II detector. Each movie includes 17 frames with a total dose of $35.7 \text{ e}^-/\text{\AA}^2$ at a nominal magnification of 59,000x (1.06 \AA /pixel). Images were acquired using the semi-automated acquisition workflow described in chapter 5.4.1 with a fixed defocus setting of -0.5 μm .

An overview of all parameters, including data collection, sample information and data processing, can be found in appendix C.3.

The data were acquired in three successive acquisition cycles, over four days. These four days only consider the time for the acquisition workflow, including the retraction of the PP between each acquisition cycle, for the selection of new exposure

targets. Before starting a new acquisition run, the PP had to be reinserted and settled to minimize the drift. In addition, a waiting time of 38 seconds was set between each exposure target, to reduce the stage drift.

Apart from the expected waiting times, which slow down the data acquisition, unexpected technical difficulties extended the complete experiment from four acquisition days to one week.

Prior to the data acquisition, the PP heating was activated. Thereby, the saved PP positions had to be recalibrated due to the slight shift that might occur during the heating process. The heating was typically started at the end of the day, in order to let the system settle over night.

The ATLAS, which was typically only acquired once at the beginning of each experiment, in order to scan the entire grid, had to be acquired a second time, due to a computer outage.

Further difficulties were faced during C_s correction. Here, additional waiting time was needed. Due to a high drift of the sample, the C_s corrector failed several times, which prolonged the process. The experiment was terminated by a high tension outage, caused by a flashover during the third acquisition cycle. After a complete high tension outage, the microscope needed to be restarted and all alignments had to be recalibrated. Due to the problems during data acquisition, the expectations on data quality were not very high. Even though, the amount of data was sufficient to use it as a first attempt for PP data processing.

Data Processing

Data processing was performed, following the reconstruction workflow of the reference dataset. An overview about the single workflow steps and their results can be found in figure 5.10. From the total 4229 images, 1985 images were discarded after a first round of visual image inspection, due to insufficient sample quality (e.g. too much carbon film, ice contamination, no ice). 2294 were used for further processing, starting with motion correction using MotionCor. A selection of motion-corrected micrographs is shown in figure 5.9.

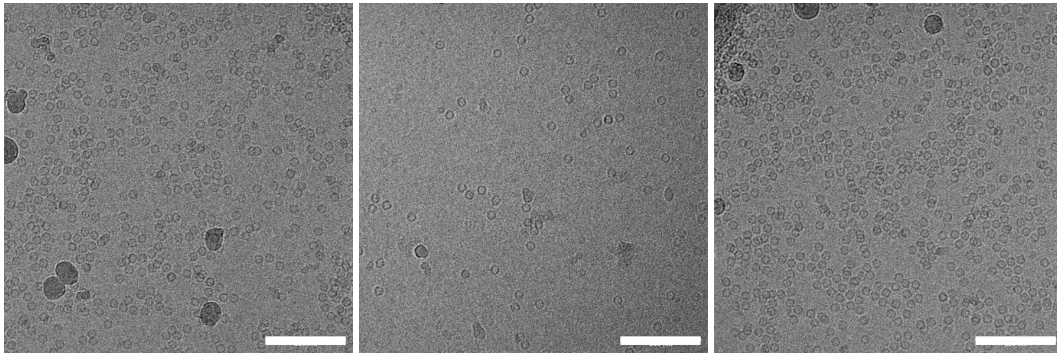


Figure 5.9: Motion-corrected micrographs from the first PP dataset acquired in *rocking*-mode. The contrast was enhanced by histogram equalization. Scale bars: 100 nm.

For the next step of reconstruction, the CTF estimation, a special PP version of Gctf (1.18) was used. CTF estimation is a crucial step in the data reconstruction workflow. Especially for PP data the estimation of the CTF is important. Due to the additional unknown parameter in the CTF, the phase shift, the correct fitting of the CTF is difficult. Here, the CTF was fitted using the parameters listed in table 5.4.

Table 5.4: Parameters for the first CTF estimation using Gctf1.18.

Parameters for CTF estimation	Gctf1.18
Spherical aberration [mm]	0.01
Voltage [kV]	300
Amplitude contrast	0.1
Magnified pixel size [\AA]	1.06
Amount of astigmatism [\AA]	500
FFT box size [pixel]	512
Minimum resolution [\AA]	100
Maximum resolution [\AA]	4
Minimum defocus value [\AA]	5,000
Maximum defocus value [\AA]	50,000
Defocus step size [\AA]	500
Minimum phase shift [deg]	30
Maximum phase shift [deg]	100
Phase plate step [deg]	5

Automated particle picking was performed using crYOLO, resulting in 78,625 found particles. These particles were used for 2D classification in RELION. For the calculation of the initial model, three out of seven 2D class averages were selected, containing 35,763 particles.

The initial model calculated from these classes showed no high similarity to known 3D models from apoferritin, e.g. from the reference dataset. However, the data were used to continue processing up to 3D refinement using 35,763 particles. The result is shown in fig. 5.10. In the 2D classes, shown in fig. 5.10, no fine structures of apoferritin appear. The initial model created out of the selected 2D classes, does not show any helical structure, only a ball. As expected, the data used for the initial model did not lead to a realistic 3D model. The visualization of the 3D structure also shows low similarity with the apoferritin structure from the reference dataset. The four-fold and three-fold channels are slightly indicated, but the resolution of this refined 3D structure is not very high. The resolution of the refined 3D model is estimated around 20-25 Å.

The question is, why did the reconstruction fail?

The answer is likely either a lack of particles, insufficiently cleaned data with too many bad particles, or a failure in the CTF estimation step.

Comparing the reference dataset, which reached a resolution of 3.4 Å, using 35,487 particles, 35,763 PP data particles should be sufficient to achieve a similar resolution. However, a further cleaning of the dataset, by running more 2D classifications, will reduce the amount of particles and might lead to the problem of an insufficient number of particles. In order to exclude the insufficient number of particles, further data need to be acquired.

As previously mentioned, the CTF estimation is a very crucial step during data reconstruction and it seems that, especially for PP data, this step is error-prone. To get a better understanding of the CTF estimation of PP data, a more systematic investigation was started. The results will be described in the following chapter.

Reconstruction of the first PP dataset

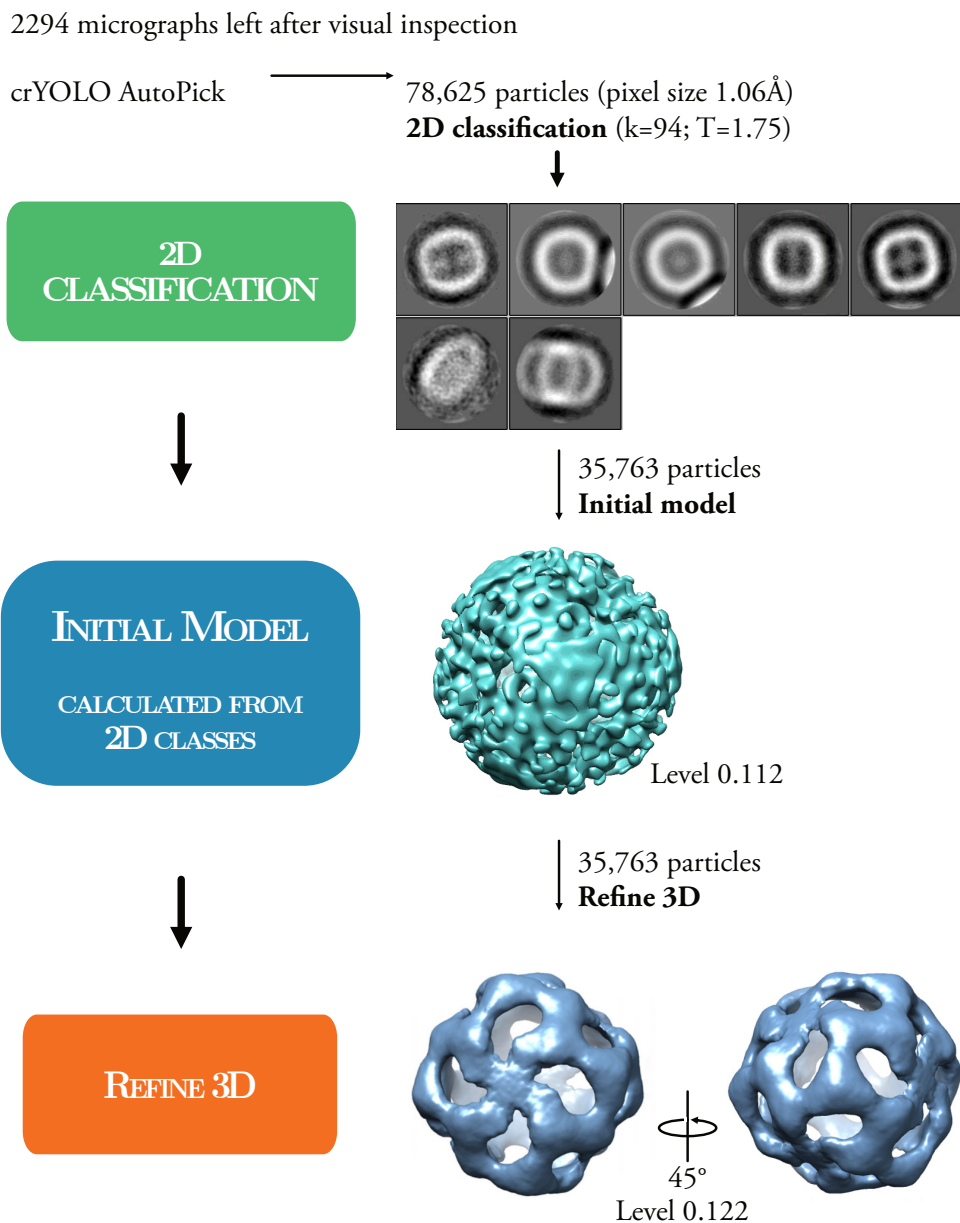


Figure 5.10: Data processing of the first PP dataset acquired in *rocking*-mode. Starting with 2294 micrographs after the first visual inspection. Picking 78,625 particles, which were used for 2D classification. Three out of seven classes have been selected for the calculation of the initial model, containing 35,763 particles. All 35,763 particles were used for 3D refinement, ending in a 3D model with an estimated resolution of approximately 20-25 Å.

5.5.2 CTF Estimation Tests

CTF estimation is an essential step in the single particle reconstruction workflow. The CTF is a microscope-specific function, describing mathematically the imaging process in the TEM. In cryo-EM, due to the low image contrast and the high background noise, the SNR is very bad. The CTF is low in the area of high-spatial frequencies due to the damping factors of the envelope function. Here, the envelope function contains information of additional effects in the image formation process, e.g. finite source size, energy spread and drift, which lowers the CTF with increasing spatial frequency [117]. The area of high-spatial frequencies is important for the CTF estimation of PP data. As the signal in this area is low, due to the envelope function and the bad SNR, the correct fitting of the CTF parameters is very difficult. As CTF estimation is a crucial step, a detailed investigation of software tools for CTF estimation was started.

Several tools are available for CTF estimation. The programs mainly used are CTFFIND4 and Gctf. Both of these tools provide versions for PP data. The first investigation focused on CTFFIND4, due to code compatibility problems with Gctf. After solving these code problems, the investigation was expanded to Gctf, following a comparison of the results.

Since the CTF correction is a time consuming step, a data subset was created for these investigations. Therefore, 100 randomly selected micrographs were taken from the first PP dataset. Both software programs allow various parameters to be set, the main parameters are listed in table 5.4.

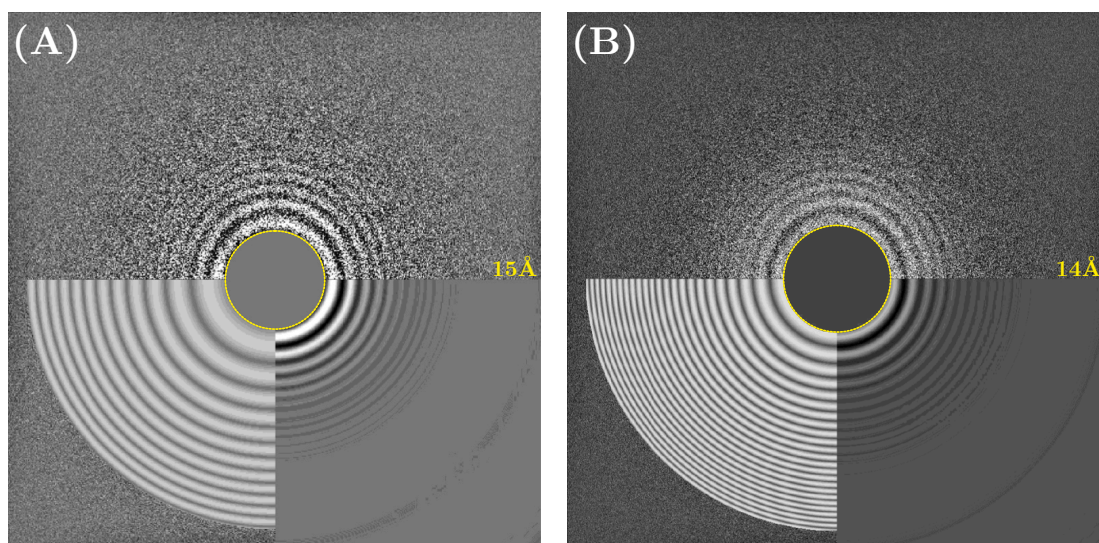


Figure 5.11: Examples of two different CTF estimation results using CTFFIND4. The yellow rings indicate the minimum resolution considered for fitting. Everything inside the gray area was not fitted. These are represented structures larger than 15 Å. (A) shows a failed fitting of the CTF estimation. The fit, shown in the lower left corner, does not match the Thon rings of the original FFT of the micrographs. (B) shows a successful match, where at least 12 Thon rings of the FFT of the micrograph were fitted.

The subset was imported into the RELION software. From here, various CTF estimations were started. In several runs, parameters such as: resolution, phase shift and phase shift step were changed in the ranges listed in table 5.5. In order to evaluate the quality of the CTF fitting, the results of the CTF estimations had to be visually inspected. Figure 5.11 shows the results of two different CTF estimation runs. Figure 5.11 (A) shows a failed CTF fitting. The Thon rings of the estimation do not fit the ones of the original FFT of the micrograph. Figure 5.11 (B) shows a successful fit. Here, the minimum resolution was set from 15 Å to 14 Å resulting in a matching CTF estimation.

In the second part of the investigation, the experiments were performed using Gctf1.18. The majority of the micrographs using the code of Gctf1.18 could not be fitted. Only approximately 15% of the data could be successfully fitted.

In general, it could be shown that PP data can be fitted by the two software pro-

grams. The high failure rate of the CTF estimation might be related to corrupted data. Bad data quality might also be the reason for the unsuccessful reconstruction of the first PP dataset. Therefore, a new dataset was acquired.

Table 5.5: Parameters used for CTF estimation in CTFFIND4 and Gctf

Parameters for CTF estimation	
Spherical aberration [mm]	0.01
Voltage [kV]	300
Amplitude contrast	0.1
Magnified pixel size [Å]	1.06
Amount of astigmatism [Å]	500
FFT box size [pixel]	512 ; 1024
Minimum resolution [Å]	12 - 30
Maximum resolution [Å]	3 - 5
Minimum defocus value [Å]	500 - 5,000
Maximum defocus value [Å]	20,000 - 50,000
Defocus step size [Å]	500
Minimum phase shift [deg]	0 - 85
Maximum phase shift [deg]	95 - 110
Phase shift step size [deg]	1 ; 5 ; 10

5.5.3 Second Data Acquisition and Reconstruction using a *Rocking-Phase Plate*

Data Acquisition

The dataset was acquired using the same PP (PP IrNo4), changing the position to a second 2 μm PP hole. The acquisition was executed according to the semi-automated workflow, recording 1550 micrographs in total. The data acquisition and the reconstruction parameter can be found in appendix C.6. A second acquisition cycle with this PP was not possible. The PP broke during the first recording cycle. 1045 out of 3534 micrographs were acquired with the PP in *rocking-mode*.

Data Processing

After the visual inspection of the micrographs and discarding the bad images, 1045 micrographs were imported into RELION. CTF estimation was performed using CTFFIND4. 940 micrographs remained for further processing, after the visual inspection of the micrographs and their CTF estimations. Particles were picked using crYOLO resulting in a total number of 166,740 particles. 2D class averages were calculated out of the 166,740 extracted particles, shown in figure 5.12. The 2D class averages shown here, show a more detailed structure of the particle compared to the previous dataset. 23 out of 100 2D class averages were selected containing 29,421 particles. In a second run of 2D classification, all classes were selected. The calculation of the initial model using 29,421 particles, resulted again in a 3D initial model with low similarity to known 3D structures of apoferritin. The 3D initial model is pictured in figure 5.12, and like the initial model of the first dataset, it does not show any helical structure. Here, the ball structure looks stretched in one direction. Data processing was not continued any further at this point, as the data quality was not convincing.

Reconstruction of the second PP dataset

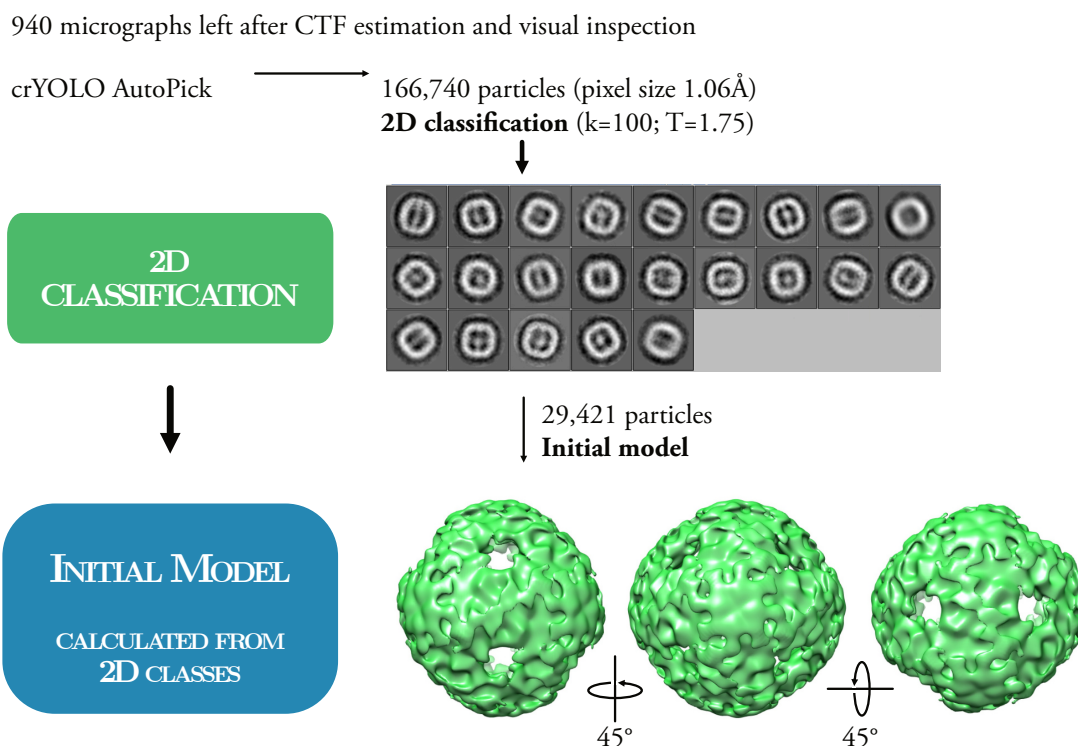


Figure 5.12: Data processing of the second PP dataset acquired in *rocking*-mode. Starting with 940 micrographs after CTF estimation and visual inspection of the CTF fitting. Picking 166,740 particles, which were used for 2D classification. 23 out of 100 2D class averages were selected for the calculation of the initial model, containing 29,421 particles.

Why did the reconstruction of the second dataset fail again?

One reason might still be an insufficient number of particles, as for this dataset the number of particles were even a bit lower. Besides, more classes could be deselected, discarding bad particles, which do not contribute to a high-resolution structure.

Furthermore, the PP broke during the acquisition, but the reason for this is unknown. Therefore, the data might be corrupted again, due to an unknown status of the PP during the recoding.

Knowing about the importance of CTF estimation, the results of this reconstruction step were further investigated. Looking at the histogram of the phase shift (fig. 5.13), an output of the RELION software shows the number of micrographs against the phase shift. Here, the histogram shows a tendency to a phase shift of approximately 50° . If this is a systematic error or ageing over time, it could not be investigated as the PP broke during the last part of the acquisition cycle. One reason for the reduced phase shift can be an insufficient thickness of the PP film. Since the broken PP had to be replaced, a new PP with a thicker iridium film (~ 10 nm) was produced and installed in the TEM.

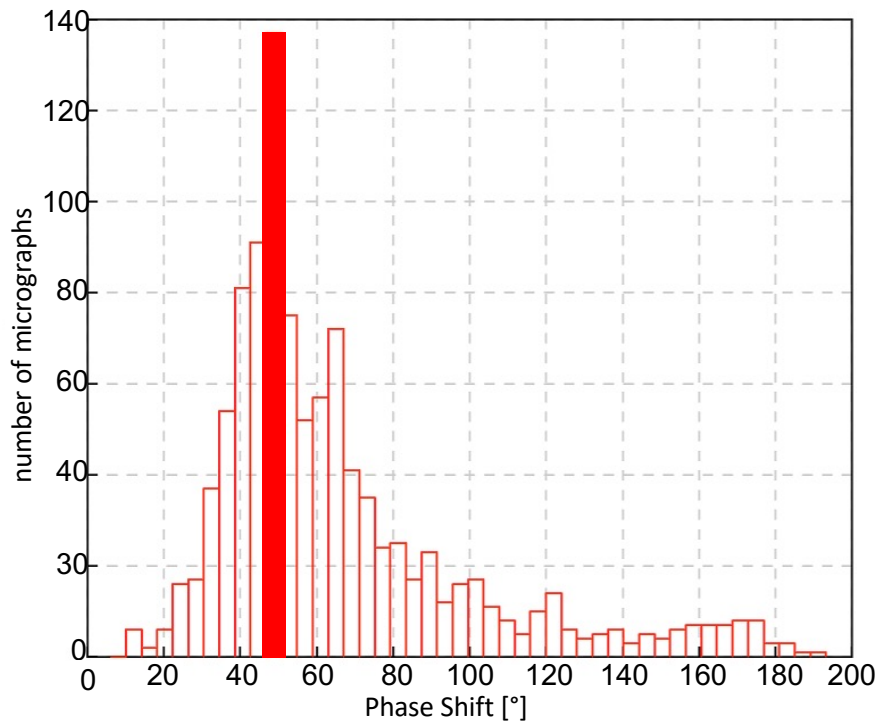


Figure 5.13: Result of the CTF estimation, showing the histogram of the PP phase shift. The PP IrNo4 with a thickness of 6.7 nm had a phase shift of approximately 50° .

Adjusted PP film thickness

In order to include the findings of the previous dataset, a new PP made of a 10.7 nm thick iridium film was produced and installed in the microscope. For a fast evaluation of the PP, a small dataset of ~ 280 micrographs was acquired. The resulting phase shift of the CTF estimation can be seen in the histogram of figure 5.14. Here, a peak is visible at a phase shift of approximately 85° . The reduced phase shift of around 50° of the PP IrNo4 is most probably related to a thin PP film. The new PP IrNo7 with a thickness of 10.7 nm is still a little bit too thin and does not reach 90° phase shift. However, the difference is in the range of less than one nm, which can hardly be controlled during the sputtering process.

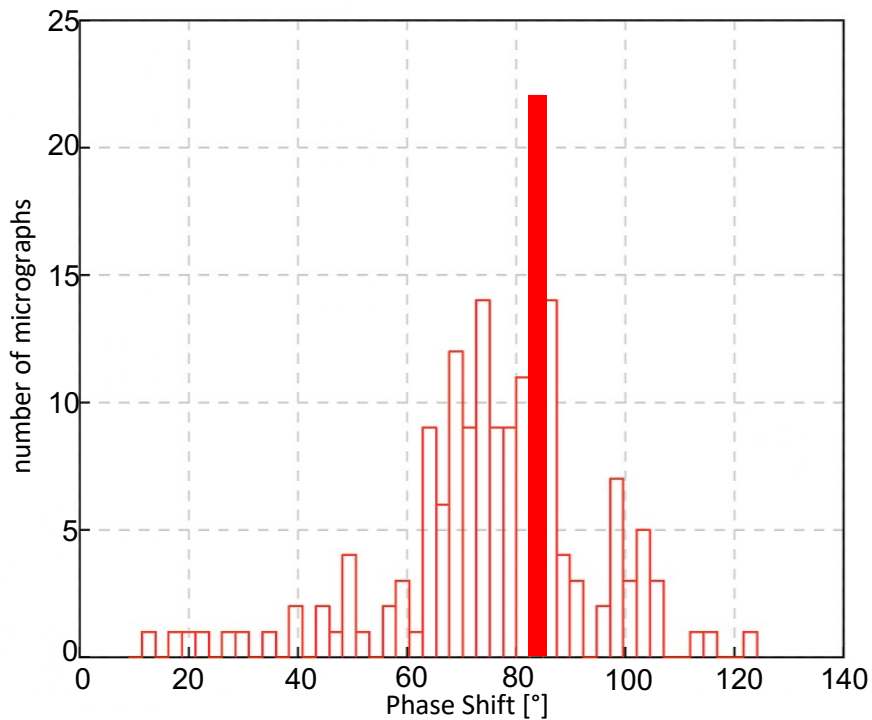


Figure 5.14: Result of the CTF estimation, showing the histogram of the PP phase shift. The PP IrNo7 with a thickness of 10.7 nm had a phase shift of approximately 85° . An increase of the PP thickness increased the phase shift.

5.5.4 Third Data Acquisition and Reconstruction using a *Rocking-Phase Plate*

Data Acquisition

For this PP dataset, the newly installed PP (IrNo7), consisting of a 10.7 nm iridium film with a 2 μm PP hole, was used for data acquisition. The PP was constantly heated since the time of installation. The micrographs were recorded using the PP in *rocking*-mode with the following settings: circle-width 10 [a.u.], resolution 16 [a.u.] and aspect-ratio 3.7 [a.u.].

In total 6,997 micrographs were acquired using the settings listed in appendix C.8. Movies were acquired using the FEI Titan Krios operated at 300 kV equipped with a Falcon II detector. Each movie includes 17 frames with a total dose of $45 \text{ e}^-/\text{\AA}^2$ at a nominal magnification of 59,000x (1.06 \AA /pixel). Images were acquired using the semi-automated acquisition workflow described in chapter 5.4.1 with a fixed defocus setting of -1 μm .

The data were recorded over 6 days in three successive acquisition cycles.

Data Processing

All micrographs were motion corrected using MotionCor. 1,166 out of 6,997 micrographs were imported into RELION after visual inspection. Many micrographs had to be discarded due to bad image quality, e.g. insufficient number of particles per image, crystalline ice, wrong defocus. A selection of motion-corrected micrographs is shown in figure 5.15. CTF estimation was performed in RELION using Gctf 1.18 with the parameters listed in table 5.6. Afterwards, 320 micrographs were discarded based on the visual inspection of the CTF estimation results. 846 micrographs were left for further processing. 195,606 particles were picked using the standard trained model in crYOLO. 2D classification was performed using RELION, resulting in 190 classes of which 12 were selected, containing 11,091 particles (fig. 5.16). An initial model was calculated from the 11,091 particles of the

12 selected 2D classes. Data processing continued, calculating three 3D classes out of the 11,091 particles. The 3D classes and the resulting 3D models, after 3D auto-refine, are shown in figure 5.16.

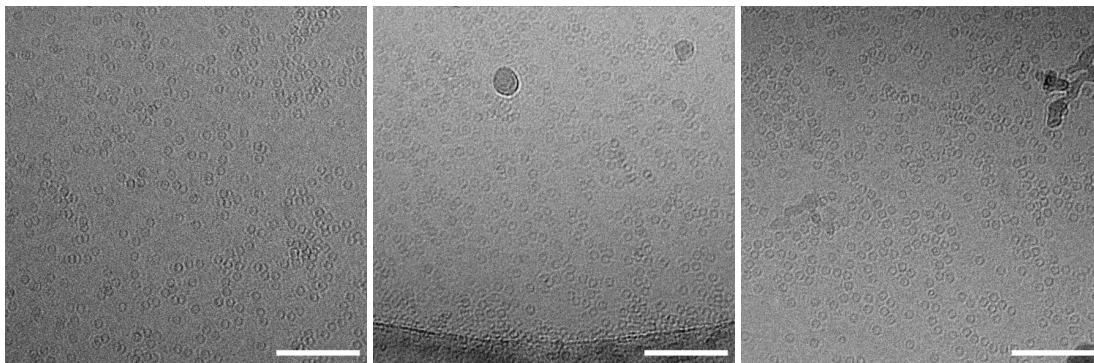


Figure 5.15: Motion-corrected micrographs out of the PP dataset acquired with a 10.7 nm iridium PP in *rocking*-mode. The contrast was enhanced by histogram equalization. Scale bars: 100 nm.

Table 5.6: Parameters used for CTF estimation using Gctf 1.18

Parameters for CTF estimation	
Spherical aberration [mm]	0.01
Voltage [kV]	300
Amplitude contrast	0.1
Magnified pixel size [\AA]	1.06
Amount of astigmatism [\AA]	500
FFT box size [pixel]	512
Minimum resolution [\AA]	100
Maximum resolution [\AA]	4
Minimum defocus value [\AA]	5,000
Maximum defocus value [\AA]	50,000
Defocus step size [\AA]	500
Minimum phase shift [deg]	40
Maximum phase shift [deg]	110
Phase shift step size [deg]	5

The 2D class averages in figure 5.16 do not show any details. They show the typical round or rectangular shape depending on the direction angle of the particle. The initial model does not show the typical apoferritin shape and looks more like a ball. Even though the quality of the initial model did not allow high expectations on the data quality, processing was continued calculating three 3D classes. The third, light blue 3D structure shows the closest fit to an apoferritin structure known from the reference dataset. However, no helical structure is visible in any of the three 3D models. Without any expectation of a better looking 3D model, 3D auto-refinement was processed. The three refined 3D models shown in figure 5.16 are even less related to an apoferritin structure than the unrefined models. The three 3D classes contain a very low amount of particles. This might be a reason why no reasonable structure can be calculated. In a further experiment, which will be described in the following chapter, the minimum amount of particles needed for a structure of apoferritin, showing helices, was investigated.

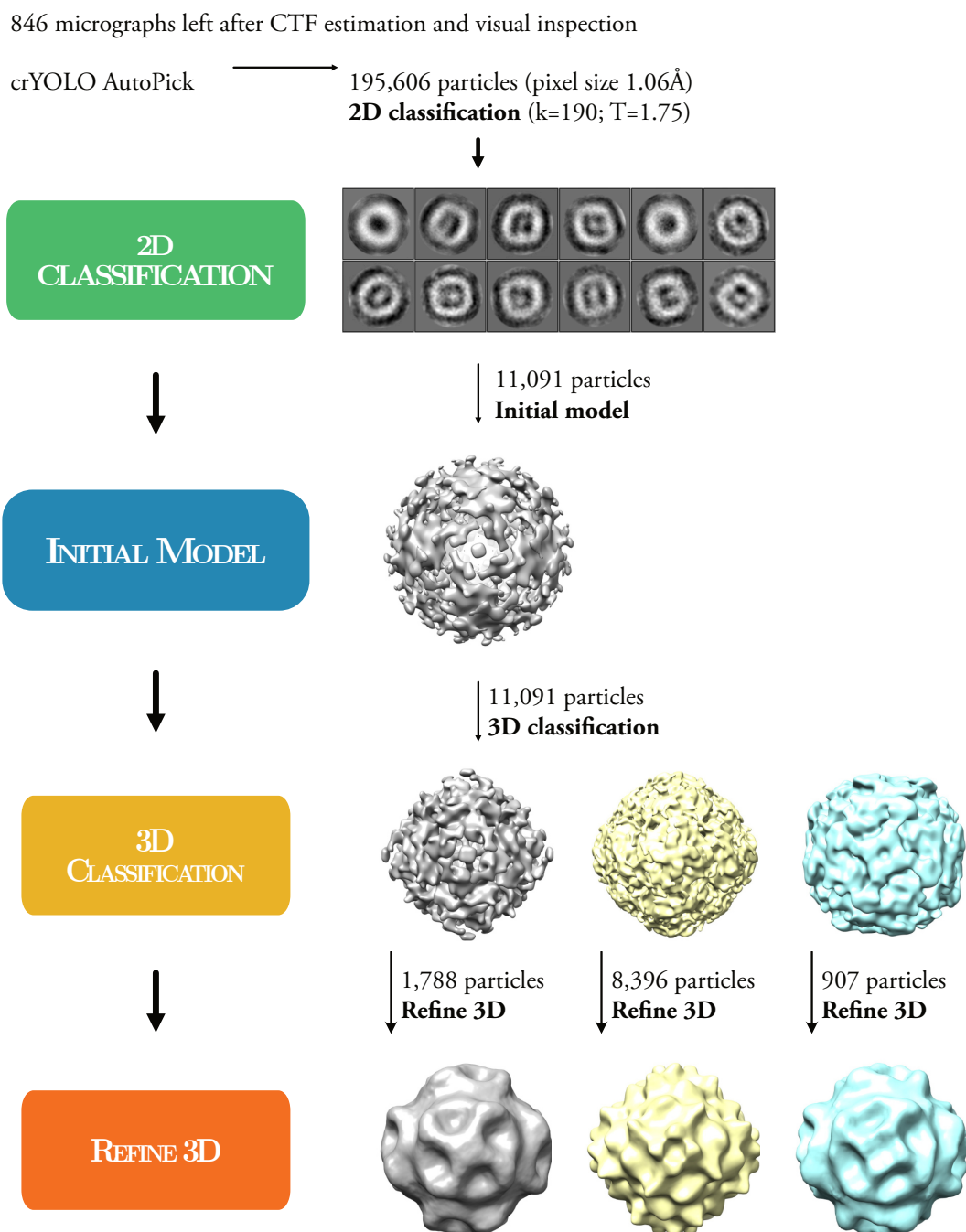


Figure 5.16: Data reconstruction of PP data acquired in rocking-mode. 846 micrographs were loaded into Relion, extracting 195,606 particles using crYOLO. After 2D classification, 12 classes containing 11,091 particles were selected for the calculation of an initial model. 11,091 particles were used for 3D classification. Each 3D class was further processed using auto-refinement.

5.5.5 Particle Comparison - Reducing the Number of Particles of the Reference Dataset

In order to clarify the influence of the number of particles on the initial model, the reference dataset was used as an example. To determine the minimum number of particles needed for an apoferritin reconstruction resolving helices ($< 6 \text{ \AA}$), the best 2D class average of the reference dataset was split randomly into four different subsets, consisting of 4000, 2000, 1000 and 500 particles. These subsets were individually processed following the standard workflow described in chapter 3.2.4. Figure 5.17 shows the reconstruction results of each particle sub-stack at each reconstruction step. First, all particle subsets were processed individually to create an initial model. Using the same particles as for the calculation of the initial model, 3D classification was performed, splitting the data into three 3D classes. In figure 5.17, the best 3D class of each particle stack is shown. 3D refinement was performed using the initial model and the best 3D class of each particle subset. The results, including the estimated resolution, are pictured in figure 5.17. As a last reconstruction step, post processing was applied individually for each set of particles.

Comparing the different initial models shown in figure 5.17, all of them derive the helical structure of apoferritin. The models consisting of 4000 and 2000 particles do not differ so much in terms of their resolution.

The subset of 1000 and 500 particles instead, show lower resolution in some areas compared to the larger subsets. With a decreasing number of particles, the resolution worsens, which can be seen in areas where the different helices can not be clearly resolved and become blurry.

A similar conclusion can be made looking at the results of the 3D classification. Here, only the best out of the three calculated 3D classes are shown in figure 5.17. Each of these classes contains less particles than the initial model. Bad particles, which were sorted into the other two 3D classes, were discarded and not used for further processing.

The two larger subsets show 3D classes with a well-resolved helical structure.

The best 3D classes contain almost all particles that have been used for the calculation of the initial model. Only 154 (3.85 %) respectively 172 (8.6 %) particles have been discarded in this step.

For the two smaller subsets, the amount of discarded particles was higher. In the subset of 1000 particles, only 332 particles were kept in the good 3D class, around 60 % of the particles were rejected. The smallest subset, containing 500 particles, lost almost 50 % of the particles in this processing step. Losing half of the particles results in a degradation of resolution, which can be seen in figure 5.17. While the structure of the 1000 particle subset still shows the helical structure of apoferritin, the smallest subset loses even more information and the structure tends to a ball-shaped model.

Looking at the results of the refinement step, the difference between the subsets becomes even more obvious. While the larger subsets show a similar 3D model with 1 Å difference in resolution, the other two subsets show results of 7.6 Å resolution or worse. The gray 3D model in figure 5.17, the result of the 500 particle subset, shows even less similarity to the structure of apoferritin. The helical structure slightly disappears and the structure turns into a ball-shaped model.

Finally, in the post processing step, the subsets with a particle count larger than 2000 show a difference in resolution in the sub-angstrom range. Particle subsets of less than 1000 particles show a huge decrease in resolution.

Comparing the initial model and the post processing results of the two small subsets (1000 and 500 particles), the number of particles might not be the only crucial factor. A good initial model is equally essential for a well-resolved 3D structure. The quality of the initial model is a good first indication, which can be seen comparing the two smaller subsets. For the calculation of the 3D classes, the amount of good particles in the best 3D class were very similar. In order to check the influence of the initial model on the 3D model quality, an additional experiment was performed.

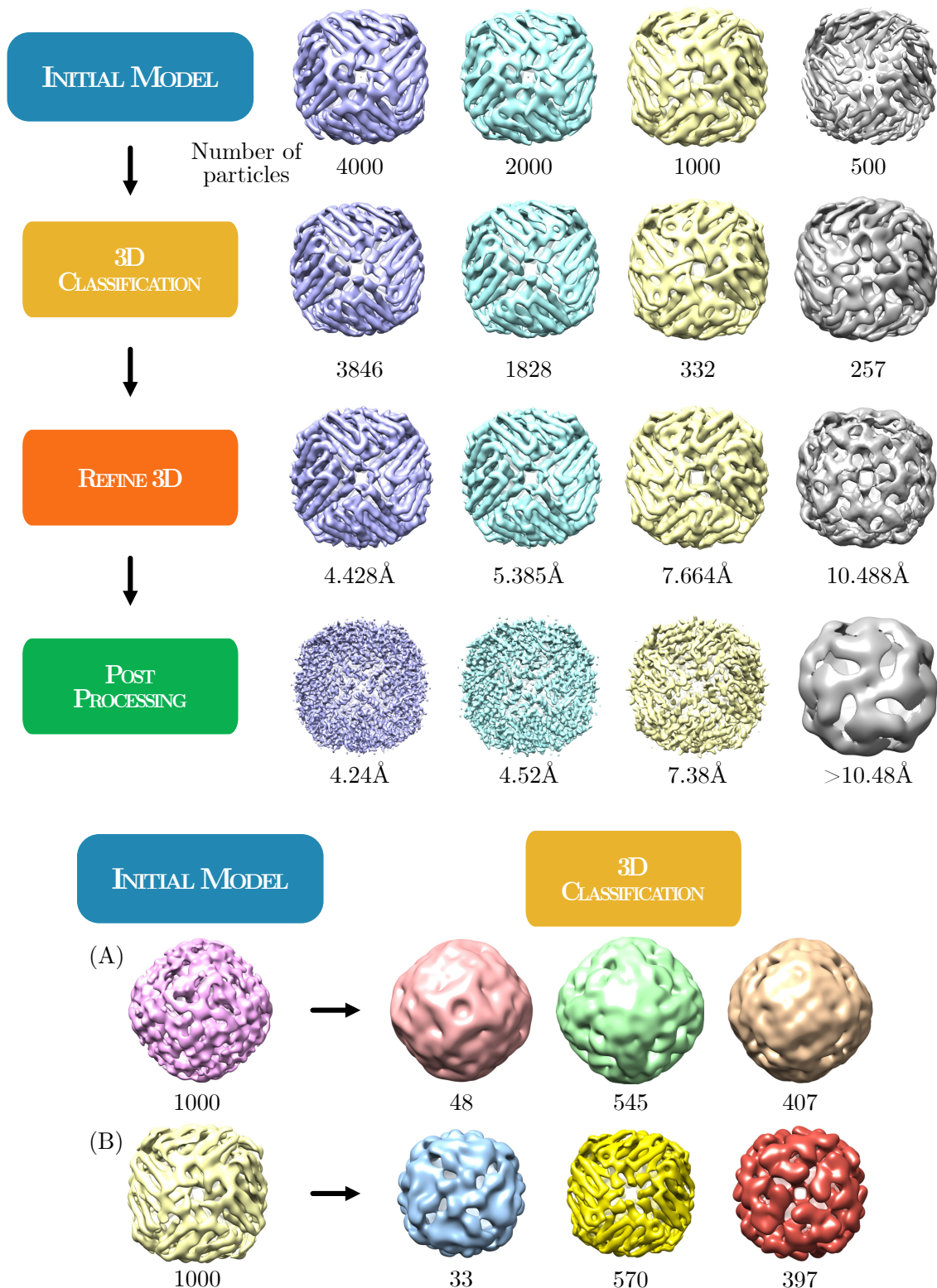


Figure 5.17: Reconstruction overview of randomly selected particle subsets of 4000, 2000, 1000 and 500 particles. Each particle subset was individually processed following the standard reconstruction workflow of chapter 3.2.4. The particle subset of 1000 particles was additionally processed using two different initial models, (A) and (B), for 3D classification.

Out of the reference dataset, an additional 1000 particle subset was randomly selected. The calculated initial model of this subset is shown in figure 5.17 (A). This initial model does not show the typical structure of apoferritin. Nevertheless, a 3D classification was run using this model (fig. 5.17 (A)). The three resulting 3D classes are shown in the same row of figure 5.17. None of these 3D models resembles the structure of apoferritin, but all three show similarities to the initial model.

In a second reconstruction, the exact same 1000 particles were used. The original initial model was replaced by the model from the earlier 1000 particle subset (fig. 5.17, light yellow model). The result of the following 3D classification is shown in fig. 5.17 (B). As an outcome of this calculation, one of the three resulting 3D classes derives in an apoferritin structure. This leads to the conclusion that using a better initial model can lead to better results in the 3D classification step.

Essential for a good 3D model is the amount of good particles used for processing. A bad initial model does not directly indicate bad data. However, using a bad initial model does not usually provide good 3D classes, which can be seen in the second experiment using two different initial models on the same 1000 particles.

Processing *rocking* datasets using an external initial model

To determine if 3D classification improves 3D classes if a high-quality initial model is used, the two *rocking* datasets were reprocessed using the good initial model of the reference subdataset from the last experiment, containing 4000 particles.

For the first dataset, described in chapter 5.5.1, the complete reconstruction was repeated. 2294 micrographs remained after visual inspection. 2053 micrographs were further deleted due to insufficient CTF fitting. Out of the 241 micrographs, 28,484 particles were extracted using crYOLO. These particles were used for two runs of 2D classification leaving five 2D classes, containing 11,193 particles for further processing. At this step, no initial model was calculated based on the 11,193 particles. Instead, the initial model from the 4000 particle subset was used for the next step, the 3D classification. The resulting three 3D classes can be seen

in the first row of figure 5.18. Figure 5.18 (A) shows the initial model calculated in the previous processing. The initial model used for the 3D classification is shown in purple.

In the second part of the experiment, the results from the reconstruction described in chapter 5.5.3 were used up to the step ‘initial model’. Here, the initially calculated initial model (fig. 5.18 (B)) was replaced by the above described reference dataset model. From here on, the reconstruction was rerun using the new initial model. The outcome of the processing using the good initial model is shown in the second row of figure 5.18.

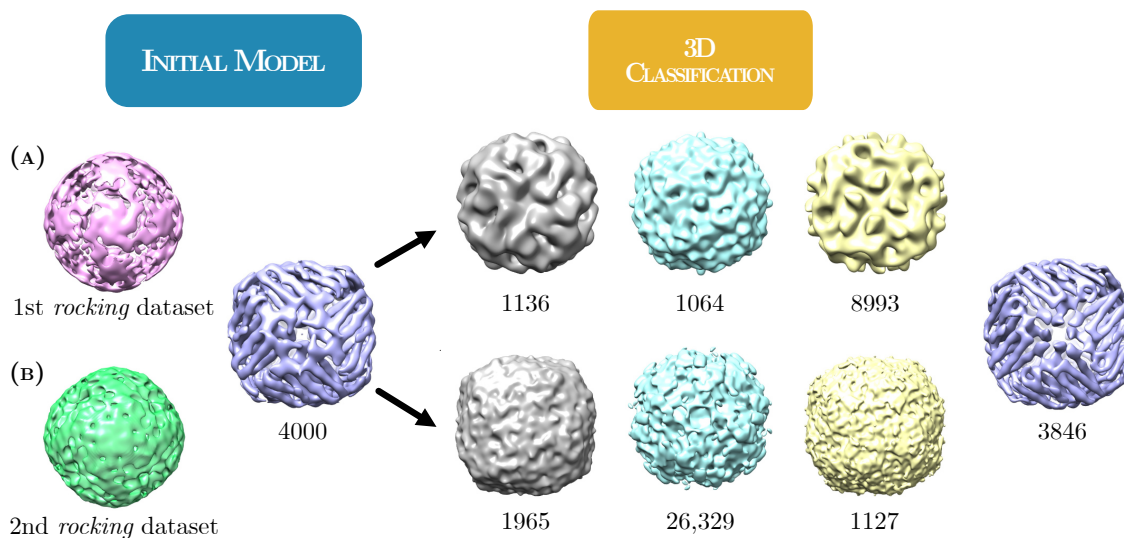


Figure 5.18: Results of the 3D classification of the two *rocking* datasets replacing their initial model by the initial model of the 4000 particle subset of the reference dataset. (A) and (B) show the initially calculated initial models of the two datasets. The purple model containing 4000 particles is the initial model, which was used for the 3D classifications performed in this experiment. In the first row the three 3D classes of the first dataset are shown. Below, the output of the 3D classification of the second dataset is shown. The purple structure on the right, containing 3846 particles, represents the best 3D class output of the reference subdataset.

For both datasets, it can be seen that using a different initial model has an effect on the 3D classification. However, none of the 3D classes shown in figure 5.18 provide a well resolved apoferritin structure, as in the reference dataset (fig. 5.18, purple apoferritin structure containing 3846 particles). For the second dataset, the 3D classes at least provide the outer shell structure of apoferritin, but not the typical helical structure of the protein. Although the resulting 3D classes show a slightly better result than before, they are still not sufficient to provide a high-resolution structure of apoferritin. Possible reasons might be bad data quality, not enough high-frequency information data or issues with the rocking-mode. In order to further investigate and exclude that the bad data are related to the rocking-mode, a PP dataset in static-mode was acquired. The experiment is described in the following chapter.

5.5.6 Data Acquisition and Reconstruction using a Phase Plate in Static-Mode

Data Acquisition

The first dataset using a PP in static-mode was acquired following the semi-automated acquisition workflow described in chapter 5.4.1. The used PP IrNo7 consisted of a 10.7 nm iridium film with a 2 μm PP hole and was constantly heated before and during acquisition. In total 576 movies were acquired using the FEI Titan Krios operated at 300 kV equipped with a Falcon II detector. Each movie was recorded with a total dose of $37.5 \text{ e}^-/\text{\AA}^2$ at a nominal magnification of 59,000x (1.06 $\text{\AA}/\text{pixel}$) and -0.5 μm defocus. The data were acquired in one acquisition cycle, over one day. An overview of all parameters, including data collection and sample information can be found in appendix C.10.

Data Processing

Data processing was performed following the reconstruction workflow of the reference dataset.

After motion correction using MotionCor 102 out of 576 micrographs, were discarded after visual image inspection due to insufficient sample quality. A selection of motion-corrected micrographs can be found in figure 5.19. 474 were used for further processing, starting with the CTF estimation, using CTFFIND4. crYOLO was used for particle picking providing 74,397 particles from 474 micrographs. Five 2D class averages were selected after 2D classification, containing 5555 particles. These 5555 particles were used to calculate an initial model, which was further used for 3D classification.

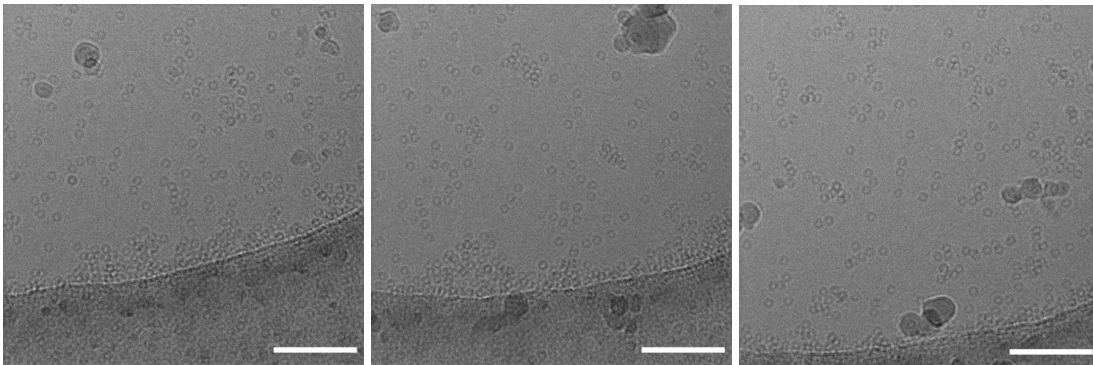


Figure 5.19: Motion-corrected micrographs of the first PP dataset acquired in static-mode. The contrast was enhanced by histogram equalization. Scale bars: 100 nm.

The results of the individual processing steps are shown in figure 5.20. Here, the 5 selected 2D classes, containing 5555 particles are pictured. The gray 3D model represents the initial model, calculated out of the 5555 particles. It can be seen that this initial model does not resolve the typical helical structure of apoferritin. This ball-shaped initial model was then used for 3D classification. The resulting three 3D classes can be seen below. None of these three 3D classes reveal a similar structure to apoferritin.

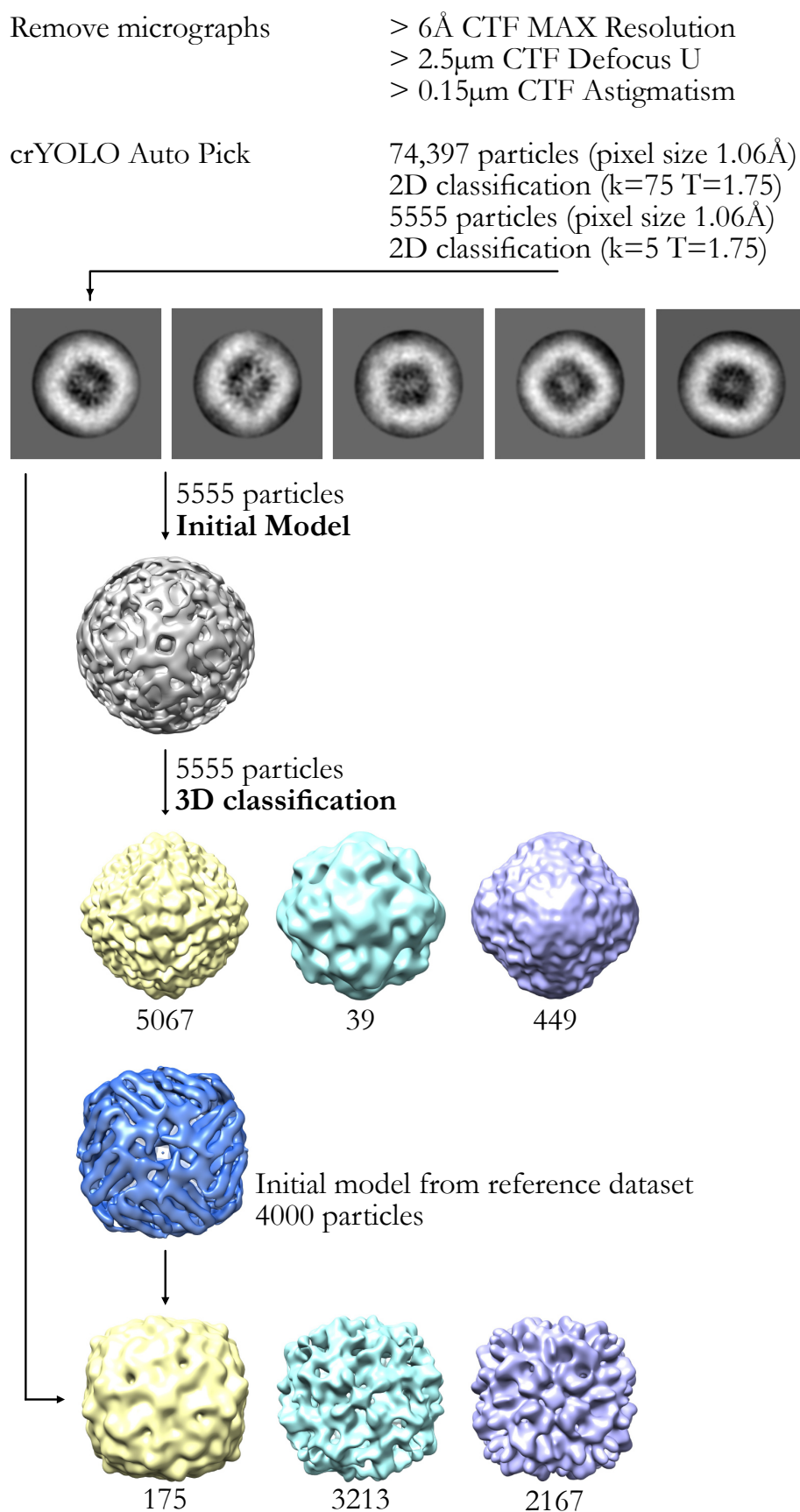


Figure 5.20: Reconstruction workflow of PP dataset in static-mode.

In order to exclude a bad influence of the here calculated initial model, the 3D classification step was repeated replacing the model. The blue initial model shown in figure 5.20 was previously calculated from a reference subdataset of 4000 particles (chapter 5.5.5). The output of the 3D classification is shown in the lower part of figure 5.20.

It must be noted that even with the replaced initial model, the 3D classes do not show a satisfying similarity with the structure of apoferritin. This might have different reasons, such as: not enough particles, containing high-resolution information or too many bad particles that are still deteriorating the results. Therefore, a high-resolution structure could not be achieved. Comparing the results of *rocking* and static-mode, no significant difference in the structure could be found.

Possible explanations for this behavior of phase-plate data will be discussed in further detail the next chapter.

5.6 Discussion

As described in the last chapter, a total number of 10 datasets with and without a PP have been recorded (appendix C). After minor sample-related problems, the data recorded without PP led to a high resolution 3D structure of apoferritin.

The datasets recorded with a PP on the other hand were much more challenging. Out of six recording sessions, only four datasets could be used for reconstruction. Multiple reconstruction experiments were made to get a high-resolution structure from these data. Unfortunately, none of these reconstructions were successful. Possible explanations for these failures will be discussed in the following chapter.

5.6.1 Sample Quality

One of the commonly discussed sources for bad data quality is insufficient sample quality. Sample preparation is a crucial and error-prone step. The sample has to fulfill several requests: the particles have to be evenly distributed in the ice layer and should not form clusters or overlap. Besides, the ice layer should neither be too thick, nor too thin. Thick ice favors overlapping of particles and the particles can be located at different focus levels in the ice layer. Contrarily, the ice should also not be too thin, as the particles could denature in the air-water interface [118].

Besides the sample preparation, the sample storage influences the sample quality. Too much time in the microscope or several times of removing and reinserting the sample into the microscope, can decrease sample quality over time.

Furthermore, the source of the sample has been discussed to be directly connected to the achievable resolution [78]. The commercially available horse apoferritin seems to result in structures around 3.5 Å, while several labs around the world reported good results using mouse apoferritin reaching a resolution of up to 1.2 Å [65, 51].

After the first attempts with horse apoferritin, the sample was replaced by mouse apoferritin, provided by M. Kikkawa (University of Tokyo). Several high-resolution structures could be reconstructed using this sample. Furthermore, the same sample grid was used for the static and reference dataset. Therefore, the sample quality as a source of insufficient data quality can nearly be excluded in this case. A structure of 3.4 Å could be obtained without a PP, whereas this was not possible on the basis of the PP data.³ Variations between the different meshes of a grid may exist, but they are usually not so severe that it could influence data quality as significantly as it can be observed here.

³The data quality looked good enough for an even higher resolved structure in case of using a larger dataset. I decided to not spend more of my limited instrument time for collecting a large reference dataset and to use more instrument time for PP datasets.

5.6.2 Reconstruction

Number of Particles and Symmetry

The number of particles, containing high-resolution information, is an essential factor for a successful data reconstruction. It could be shown for the reference dataset, that a small number of particles can be sufficient for a reasonable reconstruction of apoferritin. Using individual subsets of 4000, 2000, 1000 and 500 particles, out of a good 2D class, showed that only for the smallest subset, no apoferritin structure could be resolved. The total amount of acquired particles is not critical, but rather the total number of particles containing the important high-resolution information. As previously demonstrated using the reference dataset, at least a good 2D class average containing around 2000 particles should provide an apoferritin structure.

Therefore, an insufficient number of particles is also less likely the reason for the failed reconstructions. However, it is possible that in the amount of bad particles in the selected 2D class averages predominates and no structure can be resolved.

The principle behind single particle analysis is to take thousands of images of the same type of particle in order to statistically image the particle under many different angles. If the number of different views is too low, the resolution of the 3D structure can reduce. One possible reason for a low number of viewing angles is preferred orientation. Preferred orientation can occur e.g. by intermolecular forces on the sample grid prior to the vitrification. In extreme cases, preorientation can lead to a loss of resolution or even a complete fail of the reconstruction.

In case of apoferritin, this should not be an issue. Apoferritin is a highly symmetric protein with octahedral symmetry (O). With such a high symmetry, the number of needed angular views is dramatically reduced compared to a low symmetry protein like e.g. *E. coli* 70S ribosomes [119] or human ribosomes [120]. The high symmetry is one of the reasons why apoferritin is the perfect benchmark sample.

To completely rule out missing views, an additional reconstruction test was run. RELION allows the modification of the particle symmetry during reconstruction.

If a structure of a particle is completely unknown or a particle shows no symmetry, C1 symmetry is applied during data processing.

An experiment was performed reprocessing a dataset acquired with and without a PP applying C1 instead of octahedral symmetry. Figure 5.21 shows the resulting 3D maps. The upper green PP structure (A) shows the refined 3D map of all particles. This 3D map does not feature any symmetry at all. Furthermore, it does not show any similarity to the structure of apoferritin.

In comparison, the lower yellow structure (B), reconstructed from a dataset without a PP, does show roughly the symmetry of apoferritin. For the yellow model, all particles after 2D classification were used. The orange map (C) only consists of one selected good 3D class and was also processed with applied symmetry C1. Here, the typical structure of apoferritin is even more obvious than in model (B). In order to compare the structures at the same level, the 3D class (C) was further refined, resulting in the 3D map shown in red (D).

As a result of this experiment, a wrongly induced symmetry during reconstruction can also be excluded as a potential cause of failure. The reconstruction of the reference data, calculated with C1 symmetry, did not show any problems with this type of applied symmetry. Despite the C1 symmetry, the reconstruction shows the typical apoferritin structure. Moreover, for PP data, no improvements could be shown, applying C1 instead of octahedral symmetry.

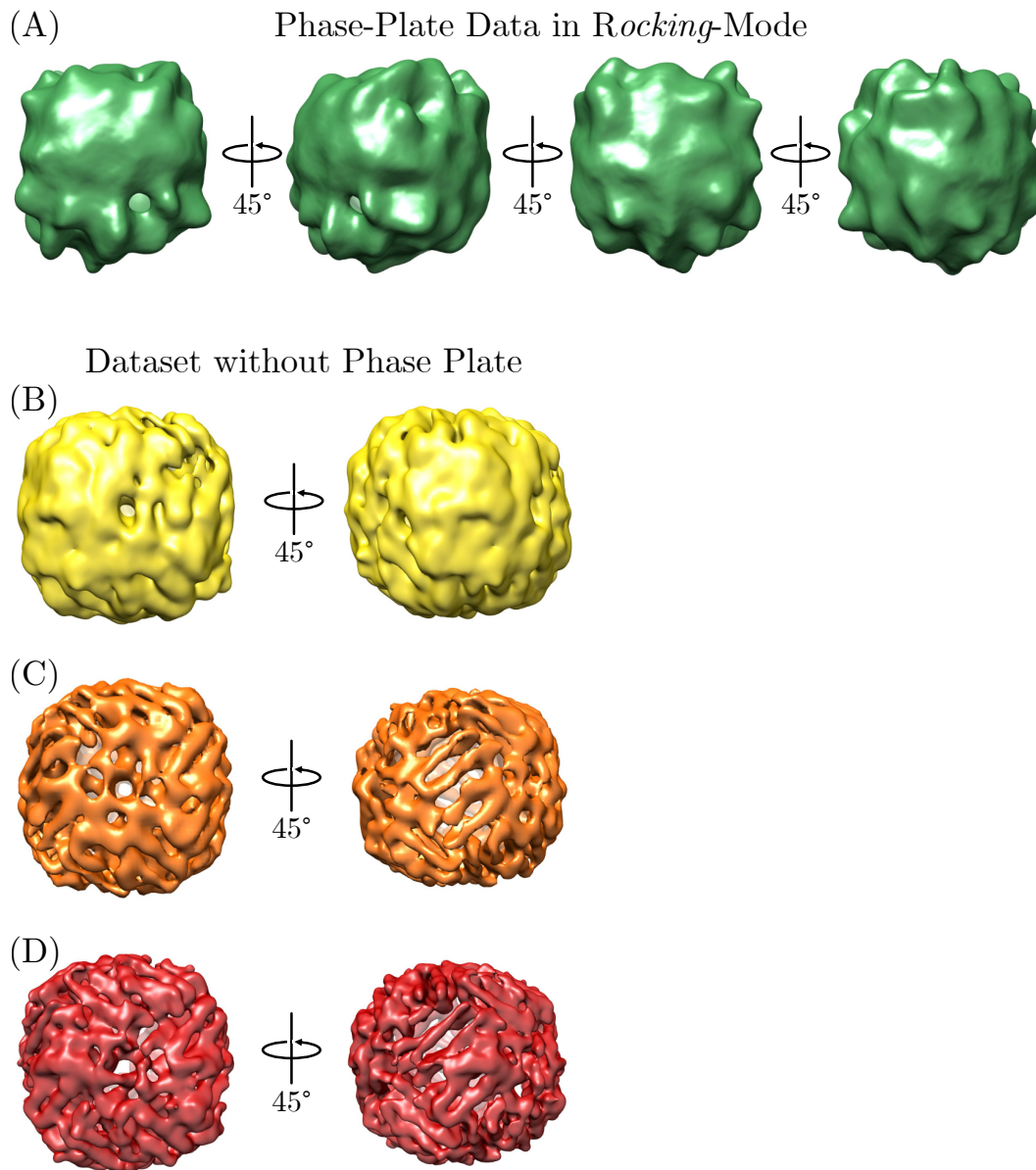


Figure 5.21: Datasets reconstructed with applied C1 symmetry. The green 3D map (A) represents the reconstructed 3D model of a PP dataset, compared to the yellow model (B), representing non PP data. For the structures (A) and (B) all particles were used for the reconstruction. (C) shows the best 3D class with applied C1 symmetry. The refined 3D map of the orange 3D class is shown in red (D).

CTF Estimation

CTF is a very pivotal step in data processing. Actual CTF estimation programs, such as Gctf and CTFFIND4, provide special versions for PP data. During the processing of PP data in this work, lots of micrographs were discarded after the CTF estimation step, due to a false CTF fitting. Why the CTF could not be estimated for these micrographs is not completely understood. One explanation might be the set search ranges. The CTF estimation software allows to set individual search ranges for the parameters that have to be fitted. Usually, changed ranges are the defocus, minimum and maximum resolution, as well as minimum and maximum phase shift, in case of phase plate data. A possible explanation for the failure of the CTF fitting might be that the actual values are out of the set search range and can therefore not be estimated properly. Besides, some of the micrographs might be acquired too close to focus that the provided Thon rings are not sufficient for a correct fitting.

Danev et al. acquired data in focus using the VPP [47]. As the FFTs of micrographs acquired in focus, do not show any Thon rings at all, fitting the CTF is almost impossible. Therefore, the CTF estimation step was skipped and processing was continued without the CTF information.

In the experiments performed in this thesis, a slight defocus was applied, because of the modified acquisition workflow. Although the herein used Titan Krios is an extremely stable microscope, focus variations in the range of 0.5 - 3 μm occurred (chapter 5.4.2). To avoid micrographs in over focus, a slight defocus of -0.5 μm was applied. With this setup, enough Thon rings for a CTF correction were observable, but it can not be excluded that some images were too close to focus or even recorded in over focus.

As for the majority of micrographs in a dataset, the CTF parameters could not be properly estimated. A pursuing experiment was performed, processing the PP data without the CTF estimation step. The results of this experiment did not show any improvements in the data processing. Also, when skipping the CTF correction, the reconstruction did not improve.

Taking a closer look at the successful CTF estimations, led to the output of estimated phase shifts. The output histograms of the PP datasets (fig. 5.13, fig. 5.14), show a phase-shift distribution (chapter 5.5.3).

Both histograms show an obvious tendency towards one phase shift value. However, not just one phase shift value can be seen here, as it would be expected for an ideal Zernike PP with a constant phase shift. Although, a fixed phase shift value would be ideal, the slight phase shift variation was not expected to become a problem. Danev et al. also reported a drift of the phase shift during data acquisition [47]. In their experiments, the reconstruction was not hindered.

What could be the reason for the observed phase shift instability?

Two possible explanations might explain this phenomena.

At first, the fluctuations around the main peak could be related to miscalculated CTF estimations. As mentioned above, micrographs might still be acquired in or over focus, so that the CTF estimation leads to false estimated phase shifts.

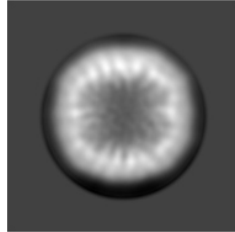
The second possibility might go back to the PP itself. Potentially, the PP still underlies charging and ageing effects. Charging and ageing of the PP occurs due to contamination of the PP inside the microscope. These effects can force the PP to act like a lens and affect the CTF. Acting like a lens can be problematic because a standard formula for fitting the CTF may not apply. If such an effect is the reason for a failure, it was not examined in more detail due to the huge effort for such an investigation. To get a closer insight in the behavior of the CTF in case the PP acts like a lens, numerical simulation would be needed to calculate the situation around the back focal plane (where the PP is positioned) and the image plane. The resources for extended simulations to solve these questions at a more fundamental level could not be provided, neither at caesar nor from my scientific network.

Summarizing, CTF estimation stays as a potential source of error. It can not be clearly excluded that the data reconstruction fails because of errors in the CTF fitting. Therefore, CTF estimation is still a topic for further investigation.

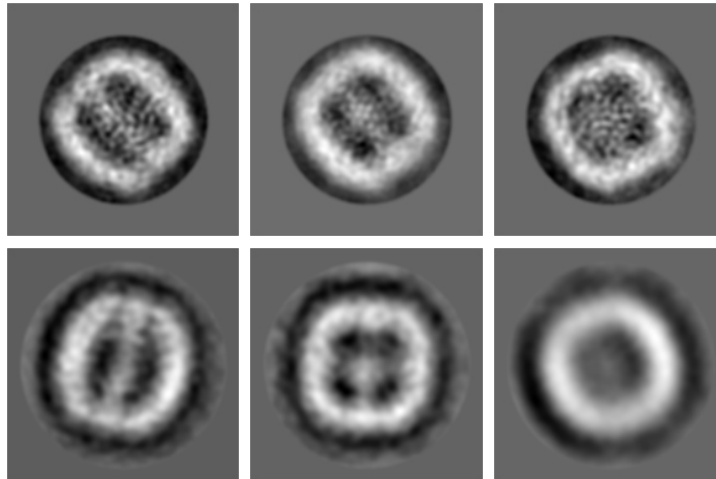
2D Classification

2D classification is the main sorting step to clean the dataset from bad particles. Besides, it is a good indication to evaluate the quality of the data.

Reference Dataset without Phase Plate



Phase-Plate Data in *Rocking-Mode*



Phase-Plate Data in *Static-Mode*

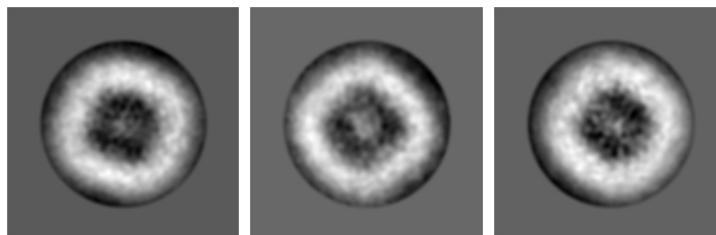


Figure 5.22: Comparison of 2D class averages of the reference dataset and data acquired with PP in *rocking* and *static*-mode.

In figure 5.22 various examples of 2D class averages taken from the recorded datasets are pictured. Looking at the first 2D class average, selected from the reference dataset, the helical structure of apoferritin is clearly visible in the image. Some of the helices are more strongly defined towards the center of the particle, which makes the inner part look slightly like a four-leaf clover. This class contains 87% of all particles of the dataset. The pictograms represent a summed up image of all of these particle images. The good resolution of the data can already be estimated from this pictogram.

In comparison, the 2D class averaged of the *rocking* datasets mostly do not show any helical structures. This can be a hint that the expected resolution is significantly lower compared to the reference data. Nevertheless, the 2D class averages clearly show the outside shell of the particle, and in some cases the typical four-leaf clover structure.

An additional difference between the PP and reference data is an electron density in the center of the PP classes. This electron density might come from the protein structure. As the structure is not visible in the class of the reference dataset, these electron densities in the center might be strengthened in the PP data due to the increased contrast induced by the PP.

To investigate the origin of these center densities, the electron density map of an earlier version of a no PP dataset and a *rocking* dataset was compared to a 1.9 Å mouse apoferritin structure taken from the EMDB⁴ (EMD-10675 [121]). In figure 5.23 (A), the gray reference dataset model was fitted to the yellow EMDB structure. For better comparison, the EMDB structure was filtered to 4 Å and 5 Å (fig. 5.23 (A),(B)) comparing the fittings of (A) and (B). It can be seen that with a lower resolution, the center structures become more present. The electron density map shown in figure 5.23 (B) shows a cross structure with higher densities in the center. This might be the structure that can be seen in the PP data. For a better comparison, a 2D class average of a *rocking* dataset (fig. 5.22) was used to fit the EMDB structure filtered to 6 Å (figure 5.23 (C)). Here, it can be seen, that the fitted EMDB structure (yellow) matches the white particle density of the

⁴Electron Microscopy Data Bank

2D class average. The outer diameter of the particle and the inner cross structure are similar.

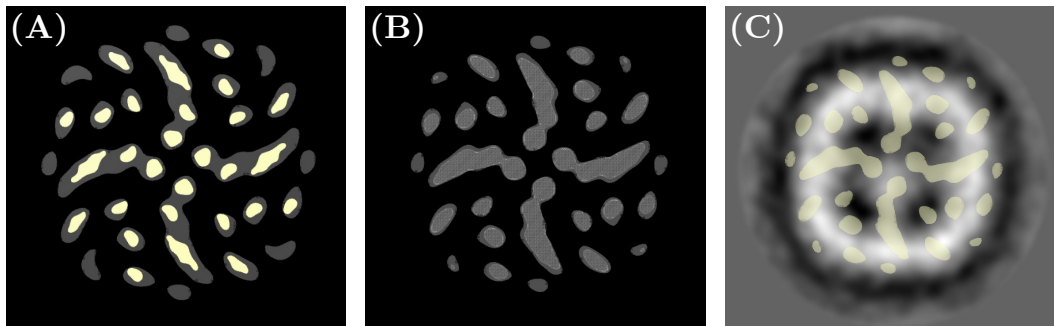


Figure 5.23: Comparison of PP and reference data with an EMDB data bank apoferritin structure. (A), (B) show comparisons of electron density maps of the reference dataset (gray) with the EMDB structure filtered to 4 Å ((A), yellow) and 5 Å ((B), light gray mesh). (C) is a 2D class average of a *rocking* dataset compared to the EMDB model filtered to 6 Å (yellow).

As both, *rocking* and static PP data, show these center densities, a second possible explanation might be fringing artifacts caused by the PP hole edge. Fringing artifacts occur due to the sharp cut-on of the phase shift. The *rocking*-mode is used to virtually smoothen this sharp cut-on and thereby reduce fringing artifacts. However, this would imply, that the static data show stronger center densities than the *rocking* data. As in this case, the *rocking* data show the stronger defined center densities. Fringing is less likely an explanation for the electron densities in the center of the particle.

5.6.3 Legimon Workflow and Recording Conditions

The standard legimon workflow that was used for the acquisition of the reference dataset was modified to adapt it to the special needs of PP data acquisition (chapter 5.4.1). In the regular workflow, the defocus is rechecked after every third micrograph. This assures a higher precision of defocus in the micrographs. For PP data acquisitions, this step was skipped. The workflow was divided into two recording parts, with and without the PP. Only the z-focus was determined during

the first recording cycle without the PP. During the second cycle using the PP, no further defocus corrections were made. The missing correction of the defocus between the micrograph recording might also be a potential error source.

In an additional test (chapter 5.4.2), the effect of skipping the focus determination was investigated. According to the results of this experiment, which was performed without a PP, the variations in defocus were in a range between 0.5 - 3.0 μm . These fluctuations are in a normal range, as they would also appear in a normal dataset.

Nevertheless, the high number of discarded micrographs in the PP datasets may be a clue that the proposed z-focus routine could be optimized. It may happen that in the progress of finding the z-focus values, which runs automated and unsupervised, the focus determination fails on some spots due to locally bad sample quality e.g. ice crystals, broken support film, etc. In these cases, either a misadjusted z-focus is used for all images of this area (15 - 30 images), which leads to unusable micrographs. Theoretically, these errors can be corrected manually. A manual correction on the other hand would be contradictory to an automated workflow and was not done. Summarizing, the workflow itself can lead to a significantly reduced number of usable images. However, as long as the bad images are discarded, this should not be a reason for the low-resolution of PP data.

5.6.4 Phase Plate

What still has to be taken into account as a possible error source is the PP itself. In the previous discussion, charging and ageing of the PP were already mentioned as possible reasons for the insufficient data quality.

Contamination of the PP most probably happens due to condensation of hydrocarbon molecules still present inside the TEM. The heating of the PP should prevent this contamination.

Two reasons could cause contamination despite heating: either the temperature is not high enough or the installation of the PP is too close to the cryo-shield of the TEM. This cryo-shield is the coldest element in the entire microscope and acts as a cryo-pump. The concentration of gaseous hydrocarbon molecules in the immedi-

ate area around the shield may be higher compared to the rest of the microscope. The position of the PP inside the microscope can not be changed. Therefore, the way to reduce contamination is to increase the temperature of the heating. Unfortunately, changing the heating element would include a complete redesign of the KonTEM holder and was not possible.

Another possible contamination source could be that the carbon support film of the PP was not completely removed by plasma etching during the fabrication process. In the progress of the fabrication experiment, a randomly selected PP was analyzed for carbon residues after plasma etching using EELS⁵ and no carbon was detected. So the film itself can also be ruled out as a source for contamination.

Here, it can be stated that preliminary experiments from KonTEM [122], using the same silicon support films like Marko et al. [105], showed contamination of these silicon films during electron irradiation. This was one reason to use pure metal films in the experiments of this thesis. It might be possible, that the contamination reported by Marko et al. [105] was caused by the silicon film and not by the metal layer.

Since none of the previously discussed possibilities seem to have a strong direct influence on the data quality, a direct visual comparison of particle images was made. This qualitative inspection may give a clue, if the particle images of the PP data show visible differences compared to the reference dataset. Particle images were compared from three datasets: with and without the PP in *rocking* and static-mode.

Figure 5.24 shows individual particles of these datasets. In the first row, particles of the reference dataset acquired without the PP are shown. Rows two and three show particles of a *rocking* and static PP dataset. For a better comparison, all micrographs were Gaussian filtered and the contrast was enhanced by histogram equalization.

Comparing the *rocking* data with the particles of the reference dataset, the particles look quite similar, which does not explain why no high-resolution structure could be obtained. However, particles acquired with the PP in static-mode look

⁵Electron Energy Loss Spectroscopy

a bit different. The ring, representing the outer shell of the protein, is wider and shows a higher density compared to the reference particles. Besides, the black halo around the particle is wider, too. The higher density and the higher contrast might be related to the fringing artifacts. These higher densities and wider structures are not visible in the *rocking* data, which would support the assumption that the *rocking*-technique reduces fringing artifacts caused by the PP hole edge.

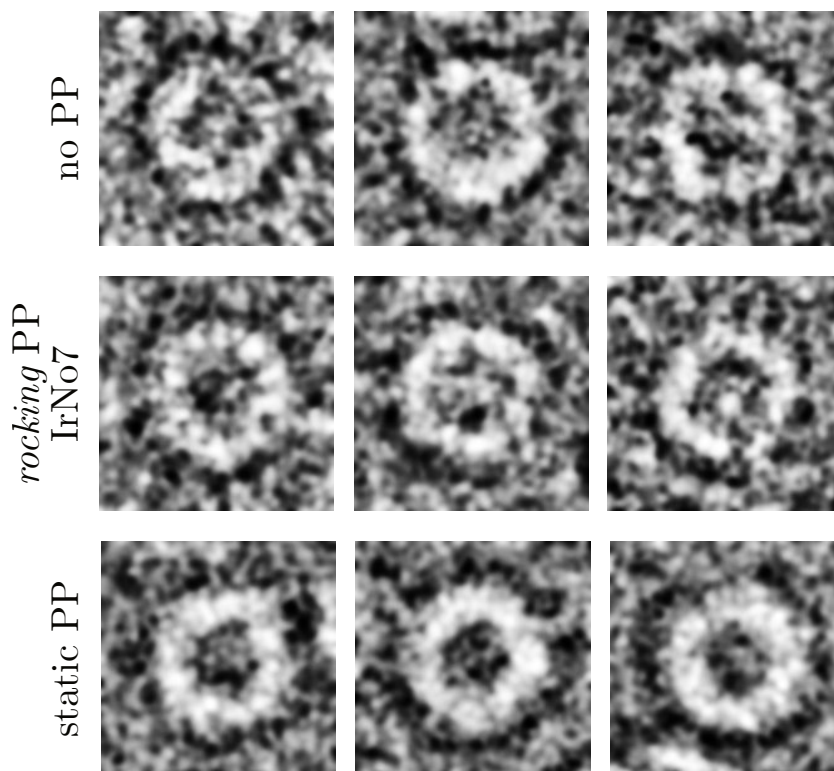


Figure 5.24: Comparison of individual particles taken from three different datasets acquired with and without a PP, in *rocking* and static-mode. All micrographs were Gaussian filtered and the contrast was enhanced by histogram equalization. Box size: 188×188 pixel.

Chapter 6

Conclusion and Outlook

In the present thesis, a new type of thin-metal film PP was developed and tested. It could be demonstrated that this type of PP can be used for single-particle data acquisition. Multiple experiments have been performed to investigate the properties of the thin-metal film PPs. The favored contrast enhancement by these PPs could be observed in the recorded micrographs. Furthermore, the stability of the PP fulfilled the requirement of a typical single-particle acquisition up to 24 h. Fringing artifacts could successfully be reduced by using the newly introduced *rocking*-mode, where the PP is moved in the back focal plane of the TEM. A resolution experiment was performed to prove that the PP does not limit the resolution. Therefore, an amorphous carbon film was imaged and Thon rings of the FFT were fitted. Here, frequencies up to 4.2 Å could be fitted. This value is comparable to other experiments without a PP.

Comparing the particles of *rocking* and reference data, they look similar in terms of size and structure. The particles of the *rocking* dataset show slightly more contrast in these images. Particles out of the static dataset show a wider and more dense structure of the protein shell. This might be related to the fringing artifacts caused by the sharp cut-on of the PP hole edge. The *rocking* data do not show this broadening of the particle shell, which is proof of the reduction of fringing artifacts by the *rocking*-mode.

A thorough search was started to identify possible error sources. Here, both reconstruction related problems as well as the PP itself were analyzed as to how they could inhibit a successful data reconstruction.

Every step of the reconstruction process, such as false CTF estimation, an insufficient number of particles or a strong influence of bad particles was analyzed. Here, no obvious problem could be identified. Also regarding the PP itself, all in-depth investigations of, e.g. contamination or *rocking* parameters could not reveal any systematic errors that would explain the failed reconstruction of the PP data.

The only clear difference between the PP compared to the reference data could be identified by a visual analysis of the particle image itself. Here, a contrast enhancement could be detected in the 2D class averages of the PP datasets. Static data, as well as *rocking* data, showed an enhanced density in the center of the particles of the 2D class averages. This extra density was even visible with a low number of particles per 2D class average. In the *rocking* data these densities were most distinct. Whether this is an effect of the *rocking*-mode could not be answered.

All things considered, it has to be admitted, that single particle analysis with a PP did not lead to the expected result.

The initial goal of a high-resolution PP structure of apoferritin outreaching the resolution of the reference dataset, or achieve a similar resolution with less particles, could not be shown. It might be possible that with a higher amount of good PP data or advanced data reconstruction, an apoferritin structure with the desired resolution can be achieved. However, in order to make this possible, significantly more data have to be acquired. The additional experimental effort, or extra work for finding special settings during reconstruction, would eliminate all advantages of using PPs for SPA.

Perhaps the PP shows its benefit in the application of smaller and lighter particles, which are not visible without a PP. Here, the PP might be used for screening the data, previous to data acquisition, in order to evaluate the density and distribution of particles. It is also possible that the strength of PPs lies in the field of electron tomography, where the targeted resolution is less demanding and the typical time to achieve a dataset is shorter in comparison to the methods described in this thesis.

Bibliography

- [1] Shen, P. S. The 2017 nobel prize in chemistry: cryo-em comes of age. *Analytical and Bioanalytical Chemistry* **410**, 2053–2057 (2018).
- [2] Choquet, D. The 2014 nobel prize in chemistry: a large-scale prize for achievements on the nanoscale. *Neuron* **84**, 1116–1119 (2014).
- [3] Galli, S. X-ray crystallography: One century of nobel prizes. *Journal of Chemical Education* **91**, 2009–2012 (2014).
- [4] Sirohi, D. *et al.* The 3.8 Å resolution cryo-em structure of zika virus. *Science* **352**, 467–470 (2016).
- [5] Ke, Z. *et al.* Structures and distributions of sars-cov-2 spike proteins on intact virions. *Nature* **588**, 498–502 (2020).
- [6] Dubochet, J. *et al.* Cryo-electron microscopy of vitrified specimens. *Q Rev Biophys* **21**, 129–228 (1988).
- [7] Agirrezabala, X. & Valle, M. *Structure and Dynamics of the Ribosome as Revealed by Cryo-Electron Microscopy*, 117–141 (Cambridge University Press, 2011).
- [8] Dubochet, J. & McDowell, A. Vitrification of pure water for electron microscopy. *Journal of Microscopy* **124**, 3–4 (1981).
- [9] Zernike, F. Das Phasenkontrastverfahren bei der mikroskopischen Beobachtung. *Z. technische Physik* **16** (1935).

- [10] Zernike, F. Phase contrast, a new method for the microscopic observation of transparent objects. *Physica* **9** (1942).
- [11] Knoll, M. & Ruska, E. Beitrag zur geometrischen Elektronenoptik. i. *Annalen der Physik* **404**, 607–640 (1932).
- [12] Knoll, M. & Ruska, E. Das Elektronenmikroskop. *Zeitschrift für Physik* **78**, 318–339 (1932).
- [13] Ruska, E. Über ein magnetisches Objektiv für das Elektronenmikroskop. *Zeitschrift für Physik* **89**, 90–128 (1934).
- [14] Ruska, H. Die Sichtbarmachung der bakteriophagen Lyse im Übermikroskop. *Naturwissenschaften* **28**, 45–46 (1940).
- [15] Ruska, E. The development of the electron microscope and of electron microscopy. *Bioscience Reports* **7**, 607–629 (1987).
- [16] Danev, R. & Nagayama, K. Chapter fourteen - Phase plates for transmission electron microscopy. In Jensen, G. J. (ed.) *Cryo-EM Part A Sample Preparation and Data Collection*, vol. 481 of *Methods in Enzymology*, 343–369 (Academic Press, 2010).
- [17] Ludwig, R. & Kohl, H. *Transmission Electron Microscopy* (Springer, New York, NY, 2008).
- [18] Egerton, R. *Physical Principles of Electron Microscopy* (Springer International Publishing, 2016).
- [19] Williams, D. B & Carter, C. B. *Transmission Electron Microscopy*, vol. 2 (Springer US, 2009).
- [20] Hawkes, P. & Spence, J. C. *Springer Handbook of Microscopy* (Springer International Publishing, 2019).
- [21] FEI Company *Falcon II TM Falcon II - 16 Megapixel TEM Direct Electron Detector with Back-Thinned Sensor Technology* (2012).

- [22] Glaeser, R. M. How good can single-particle cryo-em become? What remains before it approaches its physical limits? *Annual Review of Biophysics* **48**, 45–61 (2019).
- [23] McMullan, G., Faruqi, A. & Henderson, R. Chapter one - Direct electron detectors. In Crowther, R. (ed.) *The Resolution Revolution: Recent Advances In cryoEM*, vol. 579 of *Methods in Enzymology*, 1–17 (Academic Press, 2016).
- [24] Danev, R., Yanagisawa, H. & Kikkawa, M. Cryo-electron microscopy methodology: Current aspects and future directions. *Trends Biochem Sci* **44**, 837–848 (2019).
- [25] Haider, M., Braunshausen, G. & Schwan, E. Correction of the spherical aberration of a 200 kV TEM by means of a hexapole-corrector. *Optik* **99**, 167–179 (1995).
- [26] Scherzer, O. Sphärische und chromatische Korrektur von Elektronen-Linsen. *Optik* **2**, 114–132 (1947).
- [27] Haider, M. *et al.* A spherical-aberration-corrected 200 kV transmission electron microscope. *Ultramicroscopy* **75**, 53–60 (1998).
- [28] Müller, H., Uhlemann, S., Hartel, P. & Haider, M. Aberration-corrected optics: from an idea to a device. *Physics Procedia* **1**, 167–178 (2008). Proceedings of the Seventh International Conference on Charged Particle Optics (CPO-7).
- [29] Hosokawa, F. *et al.* A spherical aberration-corrected 200 kV TEM. *Journal of Electron Microscopy* **52**, 3–10 (2003).
- [30] Zemlin, F., Weiss, K., Schiske, P., Kunath, W. & Herrmann, K.-H. Coma-free alignment of high resolution electron microscopes with the aid of optical diffractograms. *Ultramicroscopy* **3**, 49–60 (1978).
- [31] Danev, R., Glaeser, R. M. & Nagayama, K. Practical factors affecting the performance of a thin-film phase plate for transmission electron microscopy. *Ultramicroscopy* **109**, 312–325 (2009).

- [32] Marko, M., Leith, A., Hsieh, C. & Danev, R. Retrofit implementation of Zernike phase plate imaging for cryo-tem. *J Struct Biol* **174**, 400–412 (2011).
- [33] Malac, M. *et al.* Phase plates in the transmission electron microscope: operating principles and applications. *Microscopy* **70**, 75–115 (2020).
- [34] Frank, J. *Three-Dimensional Electron Microscopy of Macromolecular Assemblies: Visualization of Biological Molecules in Their Native State*. (Oxford University Press, 2006).
- [35] Zernike, F. Phase contrast, a new method for the microscopic observation of transparent objects. *Physica* **9**, 686–698 (1942).
- [36] Zernike, F. Phase contrast, a new method for the microscopic observation of transparent objects part ii. *Physica* **9**, 974–986 (1942).
- [37] Boersch, H. Über die Kontraste von Atomen im Elektronenmikroskop. *Zeitschrift für Naturforschung A* **2**, 615–633 (1947).
- [38] Danev, R. & Nagayama, K. Transmission electron microscopy with Zernike phase plate. *Ultramicroscopy* **88**, 243–252 (2001).
- [39] Danev, R., Okawara, H., Usuda, N., Kametani, K. & Nagayama, K. A novel phase-contrast transmission electron microscopy producing high-contrast topographic images of weak objects. *J Biol Phys* **28**, 627–635 (2002).
- [40] Schultheiß, K., Pérez-Willard, F., Barton, B., Gerthsen, D. & Schröder, R. R. Fabrication of a Boersch phase plate for phase contrast imaging in a transmission electron microscope. *Review of Scientific Instruments* **77**, 033701 (2006).
- [41] Majorovits, E. *et al.* Optimizing phase contrast in transmission electron microscopy with an electrostatic (Boersch) phase plate. *Ultramicroscopy* **107**, 213–226 (2007).
- [42] Schröder, R., Barton, B., Rose, H. & Benner, G. Contrast enhancement by anamorphic phase plates in an aberration-corrected tem. In *Microscopy and Microanalysis*, vol. 13, 136–137 (Cambridge University Press, 2007).

- [43] Müller, H. *et al.* Design of an electron microscope phase plate using a focused continuous-wave laser. *New Journal of Physics* **12**, 073011 (2010).
- [44] Okamoto, H. Adaptive quantum measurement for low-dose electron microscopy. *Phys. Rev. A* **81**, 043807 (2010).
- [45] Malac, M., Beleggia, M., Kawasaki, M., Li, P. & Egerton, R. F. Convenient contrast enhancement by a hole-free phase plate. *Ultramicroscopy* **118**, 77–89 (2012).
- [46] Irsen, S., Pattai, S., Kurth, P. & Wamser, J. New type of silicon-based Zernike thin-film phase plate. *Microscopy and Microanalysis* **17**, 1210–1211 (2011).
- [47] Danev, R., Buijsse, B., Khoshouei, M., Plitzko, J. M. & Baumeister, W. Volta potential phase plate for in-focus phase contrast transmission electron microscopy. *Proc Natl Acad Sci U S A* **111**, 15635–15640 (2014).
- [48] Danev, R. & Baumeister, W. Cryo-em single particle analysis with the Volta phase plate. *Elife* **5** (2016).
- [49] Danev, R., Khoshouei, M. & Baumeister, W. Single particle imaging with the Volta phase plate. *Microscopy and Microanalysis* **25**, 7–8 (2019).
- [50] Kuehlbrandt, W. The resolution revolution. *American Association for the Advancement of Science* **343**, 1443–1444 (2014).
- [51] Nakane, T. *et al.* Single-particle cryo-em at atomic resolution. *Nature* **587**, 152–156 (2020).
- [52] Yip, K. M., Fischer, N., Paknia, E., Chari, A. & Stark, H. Atomic-resolution protein structure determination by cryo-em. *Nature* **587**, 157–161 (2020).
- [53] Wrapp, D. *et al.* Cryo-em structure of the 2019-ncov spike in the prefusion conformation. *Science* **367**, 1260–1263 (2020).

- [54] Dubochet, J. The physics of rapid cooling and its implications for cryoimmobilization of cells. In *Cellular Electron Microscopy*, vol. 79 of *Methods in Cell Biology*, 7–21 (Academic Press, 2007).
- [55] Gilkey, J. C. & Staehelin, L. A. Advances in ultrarapid freezing for the preservation of cellular ultrastructure. *Journal of Electron Microscopy Technique* **3**, 177–210 (1986).
- [56] Dubochet, J. & Sartori Blanc, N. The cell in absence of aggregation artifacts. *Micron* **32**, 91–99 (2001).
- [57] Moor, H. *Theory and Practice of High Pressure Freezing*, 175–191 (Springer Berlin Heidelberg, Berlin, Heidelberg, 1987).
- [58] Jain, T., Sheehan, P., Crum, J., Carragher, B. & Potter, C. S. Spotiton: A prototype for an integrated inkjet dispense and vitrification system for cryo-tem. *Journal of Structural Biology* **179**, 68–75 (2012).
- [59] Darrow, M. C., Moore, J. P., Walker, R. J., Doering, K. & King, R. S. Chameleon: Next generation sample preparation for cryoem based on spotiton. *Microscopy and Microanalysis* **25**, 994–995 (2019).
- [60] Ravelli, R. B. G. *et al.* Cryo-em structures from sub-nl volumes using pin-printing and jet vitrification. *Nature Communications* **11**, 2563 (2020).
- [61] Russo, C. J. & Passmore, L. A. Electron microscopy: Ultrastable gold substrates for electron cryomicroscopy. *Science* **346**, 1377–1380 (2014).
- [62] Kayama, Y. *et al.* Below 3 Å resolution structure of apoferritin using a multi-purpose tem with a side-entry cryo-holder. *Scientific reports* (2021).
- [63] Hamdi, F. *et al.* 2.7 Å cryo-em structure of vitrified m. musculus h-chain apoferritin from a compact 200 keV cryo-microscope. *PLoS ONE* (2020).
- [64] Wu, M., Lander, G. C. & Herzik, M. A. Sub-2 Angstrom resolution structure determination using single-particle cryo-em at 200keV. *Journal of Structural Biology: X* **4**, 100020 (2020).

- [65] Yip, K. M., Fischer, N., Paknia, E., Chari, A. & Stark, H. Breaking the next cryo-em resolution barrier – atomic resolution determination of proteins! *Nature* **587**, 157–161 (2020).
- [66] Banyard, S. H., Stammers, D. K. & Harrison, P. M. Electron density map of apoferritin at 2.8-Å resolution. *Nature* **271**, 282–284 (1978).
- [67] Khoshouei, M., Radjainia, M., Baumeister, W. & Danev, R. Cryo-em structure of haemoglobin at 3.2 Å determined with the Volta phase plate. *Nature Communications* **8**, 16099 (2017).
- [68] Hassan, M. M. 16 - Antimicrobial coatings for textiles. In Tiwari, A. (ed.) *Handbook of Antimicrobial Coatings*, 321–355 (Elsevier, 2018).
- [69] Ryazantsev, S., Bergstrom, R., Prikhodko, S., Atanasov, I. & Avila-Sakar, A. Titan user manual. Tech. Rep., FEI Company (2008).
- [70] Kurth, P., Pattai, S., Rudolph, D., Wamser, J. & Irsen, S. Silicon-based thin film phase plates for 300 kV: First installation in an FEI Titan Krios. *European Microscopy Conference* (2012).
- [71] Irsen, S. & Kurth, P. Modular nano-positioning system for phase plates. *Microscopy and Microanalysis* **18**, 504–505 (2012).
- [72] KonTEM GmbH. Technical report (2014).
- [73] Merry, R., van de Molengraft, R. & Steinbuch, M. Modeling of a walking piezo actuator. *Sensors and Actuators A: Physical* **162**, 51–60 (2010).
- [74] Kurth, P. *et al.* Artifact-free, long-lasting phase plate. *Microscopy and Microanalysis* **20**, 220–221 (2014).
- [75] Sinha Ray, S. 3 - Structure and morphology characterization techniques. In Sinha Ray, S. (ed.) *Clay-Containing Polymer Nanocomposites*, 39–66 (Elsevier, Amsterdam, 2013).
- [76] Hameed, B. S., Bhatt, C. S., Nagaraj, B. & Suresh, A. K. Chapter 19 - Chromatography as an efficient technique for the separation of diversified

- nanoparticles. In Hussain, C. M. (ed.) *Nanomaterials in Chromatography*, 503–518 (Elsevier, 2018).
- [77] Gasteiger, E. *et al.* *Protein Identification and Analysis Tool on the ExPASy Server*, vol. 112, 571–607 (2007).
- [78] EMBL Symposium Heidelberg. Personal communication, February 7 (2020).
- [79] Thompson, R. F., Walker, M., Siebert, C. A., Muench, S. P. & Ranson, N. A. An introduction to sample preparation and imaging by cryo-electron microscopy for structural biology. *Methods* **100**, 3–15 (2016). Single Particle Cryo-EM, from sample to reconstruction.
- [80] Carragher, B. *et al.* Legion: An automated system for acquisition of images from vitreous ice specimens. *Journal of Structural Biology* **132**, 33 – 45 (2000).
- [81] Mastronarde, D. N. Automated electron microscope tomography using robust prediction of specimen movements. *Journal of Structural Biology* **152**, 36–51 (2005).
- [82] Suloway, C. *et al.* Automated molecular microscopy: the new legion system. *Journal of Structural Biology* **151**, 41–60 (2005).
- [83] Fernandez-Leiro, R. & Scheres, S. H. W. A pipeline approach to single-particle processing in *RELION*. *Acta Crystallographica Section D* **73**, 496–502 (2017).
- [84] Scheres, S. H. W. A bayesian view on cryo-em structure determination. *J Mol Biol* **415**, 406–418 (2012).
- [85] Scheres, S. H. W. Relion: implementation of a bayesian approach to cryo-em structure determination. *J Struct Biol* **180**, 519–530 (2012).
- [86] Moriya, T. *et al.* High-resolution single particle analysis from electron cryo-microscopy images using SPHIRE. *J Vis Exp* (2017).

- [87] Tang, G. *et al.* Eman2: an extensible image processing suite for electron microscopy. *J Struct Biol* **157**, 38–46 (2007).
- [88] Wagner, T. *et al.* SPHIRE-crYOLO is a fast and accurate fully automated particle picker for cryo-em. *Communications Biology* **2**, 218 (2019).
- [89] Wagner, T. & Raunser, S. The evolution of sphire-cryolo particle picking and its application in automated cryo-em processing workflows. *Communications Biology* **3**, 61 (2020).
- [90] Rohou, A. & Grigorieff, N. Ctffind4: Fast and accurate defocus estimation from electron micrographs. *Journal of Structural Biology* **192**, 216 – 221 (2015). Recent Advances in Detector Technologies and Applications for Molecular TEM.
- [91] Zhang, K. Gctf: Real-time ctf determination and correction. *Journal of Structural Biology* **193**, 1 – 12 (2016).
- [92] Zhang, K. MRC Laboratory of Molecular Biology - Gautomatch (<https://www2.mrc-lmb.cam.ac.uk/research/locally-developed-software/zhang-software/>).
- [93] Zheng, S. Q. *et al.* Motioncor2: anisotropic correction of beam-induced motion for improved cryo-electron microscopy. *Nature Methods* **14**, 331–332 (2017).
- [94] Pettersen, E. F. *et al.* UCSF Chimera—A visualization system for exploratory research and analysis. *J Comput Chem* **25**, 1605–1612 (2004).
- [95] Schindelin, J. *et al.* Fiji: an open-source platform for biological-image analysis. *Nature Methods* **9**, 676–682 (2012).
- [96] Chung, S.-C. *et al.* Pre-pro is a fast pre-processor for single-particle cryo-em by enhancing 2d classification. *Communications Biology* **3**, 508 (2020).
- [97] Vilas, J. *et al.* Advances in image processing for single-particle analysis by electron cryomicroscopy and challenges ahead. *Current Opinion in Structural*

- Biology* **52**, 127–145 (2018). Cryo electron microscopy: the impact of the cryo-em revolution in biology * Biophysical and computational methods - Part A.
- [98] Cheng, Y., Grigorieff, N., Penczek, P. A. & Walz, T. A primer to single-particle cryo-electron microscopy. *Cell* **161**, 438–449 (2015).
- [99] Punjani, A., Rubinstein, J. L., Fleet, D. J. & Brubaker, M. A. cryosparc: algorithms for rapid unsupervised cryo-em structure determination. *Nature Methods* **14**, 290–296 (2017).
- [100] Cong, Y. & Ludtke, S. J. Chapter eight - Single particle analysis at high resolution. In Jensen, G. J. (ed.) *Cryo-EM, Part B: 3-D Reconstruction*, vol. 482 of *Methods in Enzymology*, 211–235 (Academic Press, 2010).
- [101] Wang, L. & Sigworth, F. J. Cryo-em and single particles. *Physiology* **21**, 13–18 (2006).
- [102] Rohou, A. Fourier shell correlation criteria for local resolution estimation. *bioRxiv* (2020).
- [103] Scheres, S. Chapter six - Processing of structurally heterogeneous cryo-em data in relion. In Crowther, R. (ed.) *The Resolution Revolution: Recent Advances In cryoEM*, vol. 579 of *Methods in Enzymology*, 125–157 (Academic Press, 2016).
- [104] Danev, R. & Nagayama, K. Optimizing the phase shift and the cut-on periodicity of phase plates for tem. *Ultramicroscopy* **111**, 1305–1315 (2011).
- [105] Marko, M., Meng, X., Hsieh, C., Roussie, J. & Striemer, C. Methods for testing Zernike phase plates and a report on silicon-based phase plates with reduced charging and improved ageing characteristics. *J Struct Biol* **184**, 237–244 (2013).
- [106] Irsen, S., Lenz, J., Pattai, S. & Kurth, P. Silicon/chromium based thin films -a way to Zernike phase plates with long-term stability? *Microscopy and Microanalysis* **18**, 488–489 (2012).

- [107] Syed, M. *et al.* Surface morphology of gold thin films using RF magnetron sputtering (2017).
- [108] Irsen, S. Personal communication, March 17. (2020).
- [109] Fukuda, Y., Fukazawa, Y., Danev, R., Shigemoto, R. & Nagayama, K. Tuning of the Zernike phase-plate for visualization of detailed ultrastructure in complex biological specimens. *J Struct Biol* **168**, 476–484 (2009).
- [110] Danev, R. & Nagayama, K. Applicability of thin film phase plates in biological electron microscopy. *Biophysics (Nagoya-shi)* **2**, 35–43 (2006).
- [111] Barragán Sanz, K. & Irsen, S. The rocking phase plate - another step towards improved stability. *MC 2019 Berlin Microscopy Conference - Abstracts* 693–694 (2019).
- [112] Kishchenko, G. P. *et al.* Effect of fringe-artifact correction on sub-tomogram averaging from Zernike phase-plate cryo-tem. *Journal of Structural Biology* **191**, 299–305 (2015).
- [113] Abadias, G. *et al.* Review article: Stress in thin films and coatings: Current status, challenges, and prospects. *Journal of Vacuum Science & Technology A* **36**, 020801 (2018).
- [114] Sanchez, A. & Ochando, M. Calculation of the mean inner potential. *Journal of Physics C: Solid State Physics* **18**, 33–41 (1985).
- [115] Anishchenko, R. I. Calculation of the mean inner potential of a crystal in the statistical theory. *physica status solidi (b)* **18**, 923–928 (1966).
- [116] Hettler, S. *et al.* Carbon contamination in scanning transmission electron microscopy and its impact on phase-plate applications. *Micron* **96**, 38–47 (2017).
- [117] Zhu, J., Penczek, P. A., Schröder, R. & Frank, J. Three-dimensional reconstruction with contrast transfer function correction from energy-filtered cryoelectron micrographs: procedure and application to the 70S Escherichia coli ribosome. *J Struct Biol* **118**, 197–219 (1997).

- [118] D’Imprima, E. *et al.* Protein denaturation at the air-water interface and how to prevent it. *eLife* **8**, e42747 (2019).
- [119] Stark, H. Three-dimensional electron cryomicroscopy of ribosomes. *Curr Protein Pept Sci* **3**, 79–91 (2002).
- [120] Behrmann, E. *et al.* Structural snapshots of actively translating human ribosomes. *Cell* **161**, 845–857 (2015).
- [121] Fislage, M., Shkumatov, A. V., Stroobants, A. & Efremov, R. G. Assessing the JEOL CRYO ARM 300 for high-throughput automated single-particle cryo-em in a multiuser environment. *IUCrJ* **7**, 707–718 (2020).
- [122] KonTEM GmbH. Personal communication, April (2017).

List of Figures

2.1	Setup of a TEM.	6
2.2	Schematic drawing of the VPP and Zernike PP principles.	17
2.3	Schematic drawing of the image amplitude of a weak-phase object.	18
3.1	Basic mechanism of magnetron sputtering of the BAL-TEC MED 020.	29
3.2	KonTEM phase-plate system for the FEI Titan Krios.	33
3.3	Graphical user interface of the KonTROL 1.9 software.	34
3.4	Graphical user interface of KonSHAKER.	35
3.5	Schematic overview of the single particle analysis workflow from the protein sample to the three-dimensional structure of the protein.	39
3.6	Purification of equine spleen apoferritin via SEC.	40
3.7	Purification of mus musculus (mouse) apoferritin via SEC.	42
3.8	SDS-PAGE of SEC fractions.	42
3.9	Light microscopy images of a Quantifoil Holey Carbon 1/2 Cu 200 mesh TEM grid at three different magnifications.	45
3.10	Example of a typical output of the preprocessing script of an apoferritin dataset.	48

3.11 Schematic overview of the standard MSI-Edge acquisition workflow using Legimon 3.1.	49
3.12 Schematic overview of the data reconstruction pipeline in RELION.	52
3.13 Particle extraction.	54
3.14 2D class averages from an apoferritin dataset.	55
3.15 Low resolution initial model of an apoferritin dataset.	56
3.16 3D class averages and 3D model of an apoferritin dataset.	57
3.17 Post-processing output showing the 3D map and the gold-standard FSC curve.	59
4.1 FIB beam path for the PP hole cutting process and overview of the performed dose test.	62
4.2 Phase plate fabrication workflow I.	64
4.3 Light microscopy image of a gold-palladium phase plate grid.	65
4.4 TEM image of an iridium phase plate.	65
4.5 Phase plate fabrication workflow II.	67
4.6 Two SEM images of the same phase plate hole with a hole diameter of 2 μm	68
4.7 Light microscopy image of the iridium line on a glass object slide measured by the AFM cantilever tip.	70
4.8 Plots of AFM measurements of iridium PPs No4 and No5-7.	71
4.9 TEM images of AuPd phase plates.	75
4.10 TEM images of iridium PPs with dark contamination spots.	76

4.11	TEM image of an iridium PP with contamination spots caused by the unscattered electron beam.	77
4.12	Fourier Transforms of TEM micrographs acquired with an iridium PP.	78
4.13	Installation of a plasma cleaner at Titan Krios TEM at caesar.	79
4.14	TEM images of an iridium PP before and after plasma cleaning.	80
4.15	TEM images of a PP with a hole diameter of 1 μm	81
4.16	TEM micrograph of gold-on-carbon acquired without a PP and the corresponding Fourier transform.	82
4.17	Schematic drawing of the <i>rocking</i> -PP principle.	83
4.18	TEM micrographs of gold on carbon acquired with PP in static and <i>rocking</i> -mode.	84
4.19	Fourier transforms of TEM micrographs acquired with phase plate in static-mode and <i>rocking</i> -mode.	86
4.20	Fourier transforms showing the variation of <i>rocking</i> -amplitude.	88
4.21	Fourier transforms showing the variation of the <i>rocking</i> -speed.	89
5.2	Data reconstruction workflow showing the processing steps using the software RELION.	103
5.3	Data reconstruction workflow part II.	104
5.4	FSC of the reference dataset.	105
5.5	Selection of apoferritin helices.	106
5.6	Schematic overview of the modified MSI-Edge workflow using Legion 3.1 for PP data acquisition.	111

5.7	Focus distance test using Leginon 3.1.	114
5.8	FFT showing a not well centered PP.	116
5.9	Motion-corrected micrographs from the first PP dataset acquired in <i>rocking</i> -mode. The contrast was enhanced by histogram equalization. Scale bars: 100 nm.	120
5.10	Data processing of the first PP dataset acquired in <i>rocking</i> -mode.	122
5.11	CTF estimation test using CTFFIND4.	124
5.12	Data processing of the second PP dataset acquired in <i>rocking</i> -mode.	127
5.13	Phase shift histogram of the PP IrNo4.	128
5.14	Phase shift histogram of the PP IrNo7.	129
5.15	Motion-corrected micrographs out of the PP dataset acquired with a 10.7 nm iridium PP in <i>rocking</i> -mode. The contrast was enhanced by histogram equalization. Scale bars: 100 nm.	131
5.16	Data reconstruction of PP	133
5.17	Reconstruction overview of particle subsets.	136
5.18	3D Classification of <i>rocking</i> datasets using a good initial model.	138
5.19	Motion-corrected micrographs of the first PP dataset acquired in static-mode. The contrast was enhanced by histogram equalization. Scale bars: 100 nm.	140
5.20	Phase plate dataset in static-mode	141
5.21	Datasets reconstructed with applied C1 symmetry.	146
5.22	Comparison of 2D classes.	149
5.23	Comparison of PP and reference data with an EMBD data bank apoferritin structure.	151

5.24	Comparison of individual particles taken from three different datasets.	154
A.1	ProtParam analysis of ferritin heavy chain mus musculus (P09528) .	178
B.1	Plot of the phase plate thickness measuring of a 12 nm gold-palladium layer by atomic force microscopy.	180
B.2	Plot of the phase plate thickness measuring of a 45 nm gold-palladium layer by atomic force microscopy.	180
B.3	Results of the control-calibration test for layers of 30 nm and 50 nm iridium.	181
B.4	AFM measurement of Iridium phase plates IrNo2 and IrNo3.	182

List of Tables

3.1	Materials and devices used protein expression and purification.	25
3.2	Chemicals used for protein expression and purification.	26
3.3	TEM grids used in this work.	27
3.4	Instruments used for this thesis.	27
3.5	Zeiss Crossbeam XB1540 Workstation settings	37
3.6	Plunge freezing parameters for apoferritin.	44
3.7	Microscope settings used in this work for the Leginon MSI-Edge 3.0 workflow at the Titan Krios TEM at caesar.	50
3.8	Software used for single particle data acquisition, processing and reconstruction.	51
4.1	FIB settings for hole diameters determined by dose test.	63
4.2	MED 020 settings for sputtering process of the two metals used for PP films in this work.	66
5.1	Data collection parameters of the mouse apoferritin reference dataset.	100
5.2	Parameters used for CTF estimation in CTFFIND4.	102

5.3	List of apoferritin datasets acquired without a PP.	106
5.4	Parameters for the first CTF estimation using Gctf 1.18.	120
5.5	Parameters used for CTF estimation in CTFFIND4 and Gctf	125
5.6	Parameters used for CTF estimation using Gctf 1.18	131
B.1	Table of fabricated and installed phase plates.	179
C.1	Dataset I 2020-03-31-mAPO	184
C.2	Dataset II 2020-04-05-mAPO	185
C.3	Dataset III 2020-05-03-mAPO-PP	186
C.4	Dataset IV 2020-05-18-mAPO	187
C.5	Dataset V 2020-05-21-mAPO-PP	188
C.6	Dataset VI 2020-06-30-mAPO-PP	189
C.7	Dataset VII 2020-07-29-mAPO-PP	190
C.8	Dataset VIII 2020-08-12-mAPO-PP	191
C.9	Dataset IX 2020-11-23-mAPO	192
C.10	Dataset X 2020-11-30-mAPO-PP	193

Appendix A

Apo ferritin

A.1 Ferritin heavy chain equus caballus (horse)

ProtParam analysis of ferritin heavy chain equus caballus (horse) (Q8MIP0)

```
      1           11           21           31           41           51
      |           |           |           |           |           |
1   TTAFPSQVR QNYHQDSEAA INRQINLELH ASYVYLSMSF YFDRDDVALK NFAKYFLHQS   60
61  HEEREHAEKL MKLQNRGGR IFLQDIKKPD QDDWENGLKA MECALHLEKN VNESLLELHK   120
121 LATDKNDPHL CDFLETHYLN EQVKAIKELG DHVTNLRRMG APESGMAEYL FDKHTLGECD   180
181  ES
```

Number of amino acids: 181

Molecular weight: 21137.62

Theoretical pI: 5.41

Extinction coefficients:

Extinction coefficients are in units of $M^{-1} \text{ cm}^{-1}$, at 280 nm measured in water.

Ext. coefficient 16055

Abs 0.1% (=1 g/l) 0.760, assuming all pairs of Cys residues form cystines

Ext. coefficient 15930

Abs 0.1% (=1 g/l) 0.754, assuming all pairs of Cys residues are reduced

The ProtParam tool is a protein identification and analysis software and is part of the ExPASy Proteomics Server [77].

A.2 Ferritin light chain equus caballus (horse)

ProtParam analysis of ferritin light chain equus caballus (horse) (P02791)

```

      1           11           21           31           41           51
      |           |           |           |           |           |
1   SSQIRQNYSTEV EAAVNRLV NLYLRASYT YLSLGFYFDR DDVALEGVCH FFRELAE EKR    60
61  EGAERLLKMQ NQRGGRALFQ DLQKPSQDEW GTTLDAMKAA IVLEKSLNQA LLDLHALGSA 120
121 QADPHLCDFL ESHFLDEEVK LIKKMGDHLT NIQRLVGSQA GLGEYL FERL TLKHD

```

Number of amino acids: 174

Molecular weight: 19846.45

Theoretical pI: 5.36

Extinction coefficients:

Extinction coefficients are in units of $M^{-1} \text{ cm}^{-1}$, at 280 nm measured in water.

Ext. coefficient 14565

Abs 0.1% (=1 g/l) 0.734, assuming all pairs of Cys residues form cystines

Ext. coefficient 14440

Abs 0.1% (=1 g/l) 0.728, assuming all pairs of Cys residues are reduced

A.3 Ferritin heavy chain mus musculus (mouse)

ProtParam analysis of ferritin heavy chain mus musculus (mouse) (P09528)

Figure A.1: ProtParam analysis of ferritin heavy chain mus musculus (P09528)

```

      1           11           21           31           41           51
      |           |           |           |           |           |
1   1  TTASPSQVR  QNYHQDAEAA  INRQINLELY  ASYVYLSMSC  YFDRDDVALK  NFAKYFLHQS   60
61  HEEREHAEKL  MKLQNRGGR  IFLQDIKKPD  RDDWESGLNA  MECALHLEKS  VNQSLLLELHK  120
121 LATDKNDPHL  CDFIETYYLS  EQVKSIKELG  DHVTNLRKMG  APEAGMAEYL  FDKHTLGHD   180
181  ES

```

Number of amino acids: 181

Molecular weight: 20935.41

Theoretical pI: 5.53

Extinction coefficients:

Extinction coefficients are in units of $M^{-1} \text{ cm}^{-1}$, at 280 nm measured in water.

Ext. coefficient 19035

Abs 0.1% (=1 g/l) 0.909, assuming all pairs of Cys residues form cystines

Ext. coefficient 18910

Abs 0.1% (=1 g/l) 0.903, assuming all pairs of Cys residues are reduced

Appendix B

Phase Plates

B.1 Table of Phase Plates

Table B.1: Table of fabricated and installed phase plates.

Name	FIB	MED020	Plasma Etching	Krios	Film Thickness	Comment
AuPd 10 nm	05.09.2018	13.09.2018	13.09.2018	13.09.2018	10 nm	
PP IrNo 1	02.10.2018	02.10.2018	02.10.2018	02.10.2018	6.5 nm	defect
PP IrNo 1.2	02.10.2018	02.10.2018	04.10.2018	04.10.2018	6.5 nm	
PP IrNo 2	-	19.02.2019	19.02.2019	19.02.2019	6.4 nm	
PP IrNo 2	-	-	30.04.2019	30.04.2019	6.4 nm	reinstallation
PP IrNo 3	25.06.2019	28.06.2019	01.07.2019	01.07.2019	6.7 nm	
PP IrNo 4	05.12.2019	11.02.2020	01.02.2020	01.02.2020	6.9 nm	
PP IrNo 5	05.09.2018	21.07.2020	-	-	10.7 nm	
PP IrNo 6	05.09.2018	21.07.2020	27.07.2020	27.07.2020	10.7 nm	
PP IrNo 7	05.09.2018	21.07.2020	10.08.2020	10.08.2020	10.7 nm	

B.2 Coat Thickness Measuring of Phase Plates by Atomic Force Microscopy

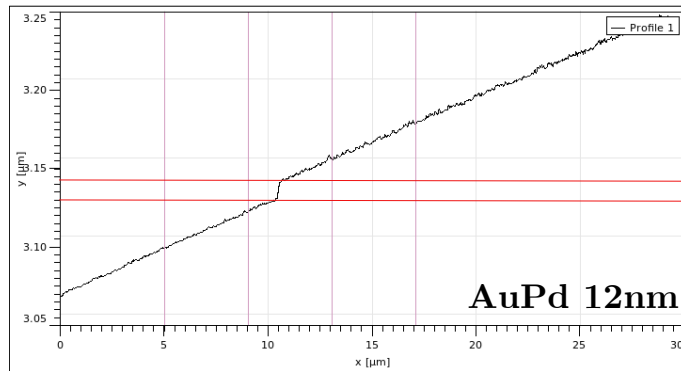


Figure B.1: Plot of the phase plate thickness measuring of a 12 nm gold-palladium layer by atomic force microscopy.

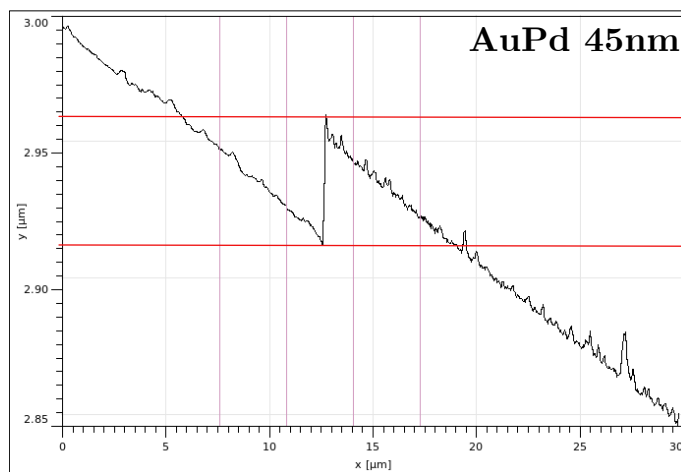


Figure B.2: Plot of the phase plate thickness measuring of a 45 nm gold-palladium layer by atomic force microscopy.

Control Calibration Test

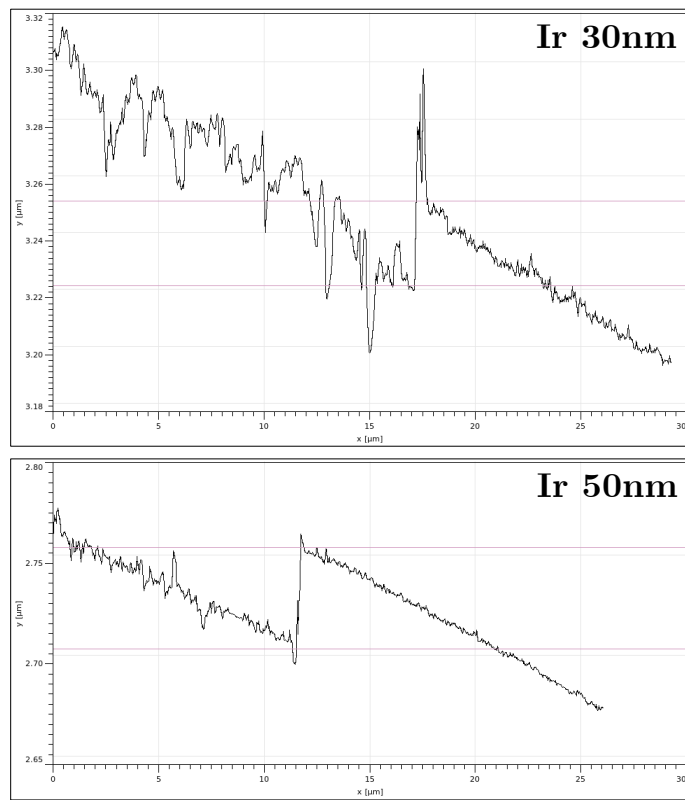


Figure B.3: Results of the control-calibration test for layers of 30 nm and 50 nm iridium.

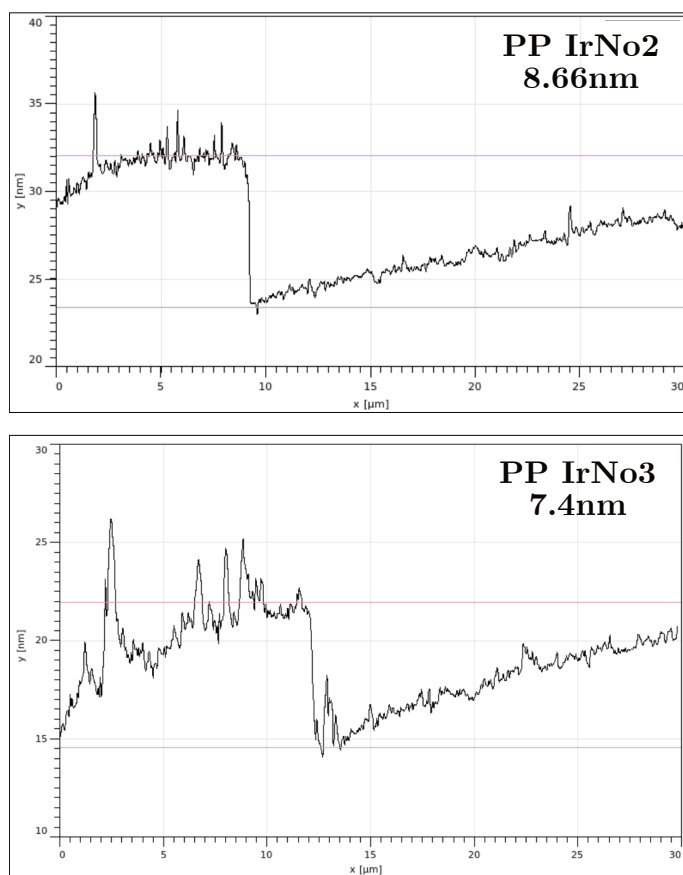


Figure B.4: AFM measurement of Iridium phase plates IrNo2 and IrNo3.

Appendix C

Datasets

The following pages provide detailed information about the recorded datasets listed below:

- Dataset I 2020-03-31-mAPO
- Dataset II 2020-04-05-mAPO
- Dataset III 2020-05-03-mAPO-PP
- Dataset IV 2020-05-18-mAPO
- Dataset V 2020-05-21-mAPO-PP
- Dataset VI 2020-06-30-mAPO-PP
- Dataset VII 2020-07-29-mAPO-PP
- Dataset VIII 2020-08-12-mAPO-PP
- Dataset IX 2020-11-23-mAPO Reference Dataset
- Dataset X 2020-11-30-mAPO-PP

C.1 Dataset I 2020-03-31-mAPO

Table C.1: Dataset I 2020-03-31-mAPO

Data collection	
Instrument	Titan Krios
Voltage [kV]	300
Magnification	59,000 x
Pixel size [Å]	1.06
C2 aperture [μm]	70
Objective aperture	No
Exposure time [s]	2
Electron dose per frame [$\text{e}/\text{Å}^2$]	1.1
Electron dose per s [$\text{e}/\text{Å}^2$]	19
Total electron dose [$\text{e}/\text{Å}^2$]	38
Defocus [μm]	-1.5 – -2.5
Micrographs [no.]	2265
Sample information	
Name	M1.1
Blotter	Leica EM GP II
Grid	Quantifoil R2/1 Cu 200 mesh
Sample	4.5 μl M. musculus apoferritin + 0.5 μl fOM
Sample solution [μl]	4
Blotting paper	Whatman 2
Blot time [s]	2.5
Temperature [°C]	20
Humidity [%]	95
Sensor	Yes

C.2 Dataset II 2020-04-05-mAPO

Table C.2: Dataset II 2020-04-05-mAPO

Data collection	
Instrument	Titan Krios
Voltage [kV]	300
Magnification	59,000 x
Pixel size [\AA]	1.06
C2 aperture [μm]	70
Objective aperture	Yes
Exposure time [s]	3
Electron dose per frame [$\text{e}/\text{\AA}^2$]	0.9
Electron dose per s [$\text{e}/\text{\AA}^2$]	15
Total electron dose [$\text{e}/\text{\AA}^2$]	46
Defocus range [μm]	-1.5 – -2.5
Micrographs [no.]	2215
Sample information	
Name	M1.1
Blotter	Leica EM GP II
Grid	Quantifoil R2/1 Cu 200 mesh
Sample	4.5 μl M. musculus apoferritin + 0.5 μl fOM
Sample solution [μl]	4
Blotting paper	Whatman 2
Blot time [s]	2.5
Temperature [$^{\circ}\text{C}$]	20
Humidity [%]	95
Sensor	Yes
Data processing	
Symmetry imposed	Octahedral (O)
Final images [no.]	1139

C.3 Dataset III 2020-05-03-mAPO-PP

Table C.3: Dataset III 2020-05-03-mAPO-PP

Data collection	
Instrument	Titan Krios
Voltage [kV]	300
Magnification	59,000 x
C2 aperture [μm]	70
Objective aperture	No
Exposure time [s]	3
Electron dose per frame [$\text{e}/\text{\AA}^2$]	1.05
Electron dose per s [$\text{e}/\text{\AA}^2$]	18
Total electron dose [$\text{e}/\text{\AA}^2$]	54
Defocus [μm]	-0.5
Micrographs [no.]	4229
Phase plate settings	
Name	PP IrNo4
Position	40
Hole diameter [μm]	2
Heating	Yes
Rocking parameter	
Circle-width [a.u.]	8
Resolution [a.u.]	2.8
Aspect-ratio [a.u.]	2
Sample information	
Name	M8.2
Blotter	Leica EM GP II
Grid	Quantifoil R2/1 Cu 200 mesh
Sample	4.5 μl M. musculus apoferritin + 0.5 μl fOM
Sample solution [μl]	4
Blotting paper	Whatman 2
Blot time [s]	2.5
Temperature [$^{\circ}\text{C}$]	20
Humidity [%]	95
Sensor	Yes

C.4 Dataset IV 2020-05-18-mAPO

Table C.4: Dataset IV 2020-05-18-mAPO

Data collection	
Instrument	Titan Krios
Voltage [kV]	300
Magnification	59,000 x
Pixel size [Å]	1.06
C2 aperture [μm]	70
Objective aperture	Yes
Exposure time [s]	3
Electron dose per frame [$\text{e}/\text{Å}^2$]	0.9
Electron dose per s [$\text{e}/\text{Å}^2$]	15
Total electron dose [$\text{e}/\text{Å}^2$]	46
Defocus range [μm]	-0.5 – -1
Micrographs [no.]	2281
Sample information	
Name	M6.1
Blotter	Leica EM GP II
Grid	Quantifoil R2/1 Cu 200 mesh
Sample	4.5 μl M. musculus apoferritin + 0.5 μl fOM
Sample solution [μl]	4
Blotting paper	Whatman 2
Blot time [s]	2.5
Temperature [°C]	20
Humidity [%]	95
Sensor	Yes

C.5 Dataset V 2020-05-21-mAPO-PP

Table C.5: Dataset V 2020-05-21-mAPO-PP

Data collection	
Instrument	Titan Krios
Voltage [kV]	300
Magnification	59,000 x
Pixel size [\AA]	1.06
C2 aperture [μm]	70
Objective aperture	No
Exposure time [s]	3
Electron dose per frame [$\text{e}/\text{\AA}^2$]	1.05
Electron dose per s [$\text{e}/\text{\AA}^2$]	18
Total electron dose [$\text{e}/\text{\AA}^2$]	54
Defocus [μm]	-1
Micrographs [no.]	2778
Phase plate settings	
Name	PP IrNo4
Position	40
Hole diameter [μm]	2
Heating	Yes
Rocking parameter	
Circle-width [a.u.]	6
Resolution [a.u.]	2.8
Aspect-ratio [a.u.]	2
Sample information	
Name	M6.1
Blotter	Leica EM GP II
Grid	Quantifoil R2/1 Cu 200 mesh
Sample	4.5 μl M. musculus apoferritin + 0.5 μl fOM
Sample solution [μl]	4
Blotting paper	Whatman 2
Blot time [s]	2.5
Temperature [$^{\circ}\text{C}$]	20
Humidity [%]	95
Sensor	Yes

C.6 Dataset VI 2020-06-30-mAPO-PP

Table C.6: Dataset VI 2020-06-30-mAPO-PP

Data collection	
Instrument	Titan Krios
Voltage [kV]	300
Magnification	59,000 x
Pixel size [\AA]	1.06
C2 aperture [μm]	70
Objective aperture	No
Exposure time [s]	4
Electron dose per frame [$\text{e}/\text{\AA}^2$]	0.8
Electron dose per s [$\text{e}/\text{\AA}^2$]	13.5
Total electron dose [$\text{e}/\text{\AA}^2$]	54
Defocus [μm]	-1
Micrographs [no.]	3534
Phase plate settings	
Name	PP IrNo4
Position	38
Hole diameter [μm]	2
Heating	Yes
Rocking parameter	
Circle-width [a.u.]	6
Resolution [a.u.]	2.8
Aspect-ratio [a.u.]	2.7
Sample information	
Name	M7.2
Blotter	Leica EM GP II
Grid	Quantifoil R2/1 Cu 200 mesh
Sample	4.5 μl M. musculus apoferritin + 0.5 μl fOM
Sample solution [μl]	4
Blotting paper	Whatman 2
Blot time [s]	3
Temperature [$^{\circ}\text{C}$]	20
Humidity [%]	95
Sensor	Yes
Data processing	
Symmetry imposed	Octahedral (O)
Initial images [no.]	1550
Final images [no.]	940

C.7 Dataset VII 2020-07-29-mAPO-PP

Table C.7: Dataset VII 2020-07-29-mAPO-PP

Data collection	
Instrument	Titan Krios
Voltage [kV]	300
Magnification	59,000 x
Pixel size [\AA]	1.06
C2 aperture [μm]	70
Objective aperture	No
Exposure time [s]	3
Electron dose per frame [$\text{e}/\text{\AA}^2$]	0.8
Electron dose per s [$\text{e}/\text{\AA}^2$]	13
Total electron dose [$\text{e}/\text{\AA}^2$]	39
Defocus [μm]	-1
Micrographs [no.]	287
Phase plate settings	
BEZEICHNUNG	PP IrNo6
Position	41 / 42
Hole diameter [μm]	2
Heating	Yes
Rocking parameter	
Circle-width [a.u.]	6
Resolution [a.u.]	2.8
Aspect-ratio [a.u.]	2.7
Sample information	
Name	M7.1
Blotter	Leica EM GP II
Grid	Quantifoil R2/1 Cu 200 mesh
Sample	4.5 μl M. musculus apoferritin + 0.5 μl fOM
Sample solution [μl]	4
Blotting paper	Whatman 2
Blot time [s]	3
Temperature [$^{\circ}\text{C}$]	20
Humidity [%]	95
Sensor	Yes

C.8 Dataset VIII 2020-08-12-mAPO-PP

Table C.8: Dataset VIII 2020-08-12-mAPO-PP

Data collection	
Instrument	Titan Krios
Voltage [kV]	300
Magnification	59,000 x
Pixel size [\AA]	1.06
C2 aperture [μm]	100
Objective aperture	No
Exposure time [s]	3
Electron dose per frame [$\text{e}/\text{\AA}^2$]	0.8
Electron dose per s [$\text{e}/\text{\AA}^2$]	15
Total electron dose [$\text{e}/\text{\AA}^2$]	45
Defocus [μm]	-1
Micrographs [no.]	6,997
Phase plate settings	
Name	PP IrNo7
Position	51 / 42
Hole diameter [μm]	2
Heating	Yes
Rocking parameter	
Circle-width [a.u.]	10
Resolution [a.u.]	16
Aspect-ratio [a.u.]	3.7
Sample information	
Name	M6.3
Blotter	Leica EM GP II
Grid	Quantifoil R2/1 Cu 200 mesh
Sample	4.5 μl M. musculus apoferritin + 0.5 μl fOM
Sample solution [μl]	4
Blotting paper	Whatman 2
Blot time [s]	2.5
Temperature [$^{\circ}\text{C}$]	20
Humidity [%]	95
Sensor	Yes
Data processing	
Symmetry imposed	Octahedral (O)
Initial particle images [no.]	1166
Final particle images [no.]	846

C.9 Dataset IX 2020-11-23-mAPO

Reference Dataset

Table C.9: Dataset IX 2020-11-23-mAPO

Data collection	
Instrument	Titan Krios
Voltage [kV]	300
Magnification	59,000 x
Pixel size [\AA]	1.06
C2 aperture [μm]	100
Objective aperture	yes
Exposure time [s]	3
Electron dose per frame [$\text{e}/\text{\AA}^2$]	0.7
Electron dose per s [$\text{e}/\text{\AA}^2$]	11.9
Total electron dose [$\text{e}/\text{\AA}^2$]	35.7
Defocus range [μm]	-1 – -2.5
Sample information	
Name	M6.3
Blotter	Leica EM GP II
Grid	Quantifoil R2/1 Cu 200 mesh
Sample	4.5 μl M. musculus apoferritin + 0.5 μl fOM
Sample solution [μl]	4
Blotting paper	Whatman 2
Blot time [s]	2.5
Temperature [$^{\circ}\text{C}$]	20
Humidity [%]	95
Sensor	Yes
Data processing	
Symmetry imposed	Octahedral (O)
Initial images [no.]	872
Final images [no.]	311

C.10 Dataset X 2020-11-30-mAPO-PP

Table C.10: Dataset X 2020-11-30-mAPO-PP

Data collection	
Instrument	Titan Krios
Voltage [kV]	300
Magnification	59,000 x
Pixel size [Å]	1.06
C2 aperture [μm]	100
Objective aperture	No
Exposure time [s]	3
Electron dose per frame [$\text{e}/\text{Å}^2$]	0.7
Electron dose per s [$\text{e}/\text{Å}^2$]	11.9
Total electron dose [$\text{e}/\text{Å}^2$]	35.7
Defocus [μm]	-0.5
Micrographs [no.]	576
Phase plate settings	
Name	PP IrNo7
Position	23
Hole diameter [μm]	2
Heating	Yes
Rocking parameter	static
Sample information	
Name	M6.3
Blotter	Leica EM GP II
Grid	Quantifoil R2/1 Cu 200 mesh
Sample	4.5 μl M. musculus apoferritin + 0.5 μl fOM
Sample solution [μl]	4
Blotting paper	Whatman 2
Blot time [s]	2.5
Temperature [°C]	20
Humidity [%]	95
Sensor	Yes
Data processing	
Symmetry imposed	Octahedral (O)

Danksagungen

An dieser Stelle möchte ich allen Menschen danken, die mich während dieser Dissertation auf vielfältige Art und Weise unterstützt haben:

Zu Beginn möchte ich mich bei Dr. Stephan Irsen (Leiter der EMA am Forschungszentrum caesar) für die Möglichkeit bedanken, dieses Projekt im Rahmen einer Doktorarbeit fortzuführen. Insbesondere danke ich ihm für die umfassende Einarbeitung in die Kryoelektronenmikroskopie und für das Vertrauen in mich, beim ‘Zerlegen’ des Mikroskops. Außerdem möchte ich mich bei ihm für die zahlreichen fachlichen wertvollen Diskussionen und die sehr gute Betreuung während meiner Dissertation bedanken.

Mein ausdrücklicher Dank gilt Prof. Barbara Hahn (Universität Koblenz-Landau) für die Betreuung dieser Arbeit einschließlich ihren wertvollen Anregungen, wissenschaftlichen Diskussionen nach caesar-Institutsseminaren und während der Thesis-Advisory-Committee-Treffen - auch über ihren Ruhestand hinaus.

Bei Dr. Magdalena Schacherl (Charité Berlin) bedanke ich mich herzlich, die meine Arbeit mit Rat und produktiven Gesprächen, fachlich sowie privat, begleitet hat. Sie hat mich insbesondere bei fachlichen Fragen zur Proteinaufreinigung und der Datenanalyse enorm unterstützt.

Ich möchte mich hiermit bei allen jetzigen, aber auch früheren Kollegen der Elektronenmikroskopie und Analytik bei caesar für die angenehme Arbeitsatmosphäre, sowie die fachliche und persönliche Unterstützung bedanken.

Insbesondere möchte ich mich bei Carola Tröger für ihren Beistand in sämtlichen Lebenslagen bedanken.

Zudem danke ich Mike Prämassing für seine fachliche Unterstützung an der FIB.

Für die Unterstützung bei der Proteinaufreinigung möchte ich mich an dieser Stelle bei den Kollegen der Gruppe von Elmar Behrmann (Universität Köln) bedanken.

Bei dieser Gelegenheit möchte ich mich zudem bei Stephan Irsen, Martin Shalita, Carola Tröger und Nikolai Krupp für die mühevollen Arbeit des Korrekturlesens dieser Dissertation bedanken.

Großer Dank geht an meine Familie, für die Aufmunterung, vielseitige Unterstützung und den stetigen Rückhalt.

Ein besonderer Dank geht an meinen Mann David, der mich bestärkt hat durchzuhalten. Vornehmlich bin ich für seine liebevolle Geduld, die Ermutigungen und den unermüdlichen Ansporn während dieser Dissertation sehr dankbar.